OBSERVATIONS OF VERY HIGH ENERGY GAMMA RAY EMISSION FROM SUPERNOVA REMNANTS WITH VERITAS

A Dissertation
Presented to
the Graduate School of
Clemson University

In Partial Fulfillment
of the Requirements for the Degree
Doctor of Philosophy
Physics

---

by
Mark Theiling
December 2009

Accepted by:
Dr. Mark D. Leising, Committee Chair
Dr. Jeremy King
Dr. Joseph R. Manson
Dr. Bradley S. Meyer

ABSTRACT

The nature and source of cosmic rays has been at the core of particle astrophysics since their discovery almost a century ago. The cosmic ray spectrum is best described by a broken power law, and can be better understood as three distinct parts. Theory holds that cosmic rays up to $\sim 10^{15}$ eV - those below the"knee" or steepening in the spectrum - are produced in the shocks of supernova remnants. Direct detection of cosmic rays produced in supernova remnant shocks is impossible, however, as cosmic rays below $\sim 10^{18}$ eV are deflected by the Galactic magnetic field and cannot be traced back to their origins.

If high energy hadrons are produced within the immediate environment of a supernova remnant, collisions will occur within the surrounding medium. As a result, pion production and subsequent decay will give rise to very high energy gamma rays (E >100 GeV). Since these gamma rays will not interact with any magnetic field, they can be traced back to their point of origin. Thus, Atmospheric Cherenkov Detectors like VERITAS, which have the capability to detect very high energy gamma rays via their interaction with our atmosphere, provide us the means of directly testing the theory of the origin of cosmic rays in supernova remnants.

Observations of 13 supernovae made with the VERITAS instrument are presented herein, including 5 individually targeted remnants and 8 remnants within the VERITAS Cygnus region Sky Survey. The observations provide detections of two known VHE remnants (Cassiopeia A and the Crab Nebula), and meaningful flux limits on the remainder. Comparison of these results to both hadronic- and leptonic-origin emission models is carried out.

DEDICATION

To my wife Bethany, for always giving me something to live up to.

ACKNOWLEDGEMENTS

I would like to thank my advisor first and foremost, but I have been gifted with several great scientists who've worn that title. Thanks to Dr. Mark Leising, my advisor at Clemson, who first woke me up to the possibilities of X-ray and gamma-ray astronomy. I have also been lucky enough to have two pre-doctoral advisors through the Smithsonian Astrophysical Observatory: Dr. Trevor Weekes, without whose enduring contributions the field of TeV astronomy would be a poorer place (and possibly no place at all), and Dr. Wystan Benbow, for being both the very model of a modern astrophysicist and a generous friend.

I would like to thank all of my VERITAS collaborators, for building such an amazing piece of technology and welcoming an outside graduate student to work and play with them on it. Thanks to Jeremy for all of his invaluable help, and his wife Donna for reminding me of all the best parts of home. Thanks to John Kildea, who may have moved on to greener pastures but likely still knows more astrophysics than I ever will and was kind enough to teach me a bit before he left. Andy, I can only thank you for always making me laugh, often against my will and my better judgement. John E. Ward, you are an unstoppable machine of astrophysics. Kenn Gibbs deserves a round of applause as well, for willingly shouldering the burden of the critic; crucial, yet so rarely appreciated.

To the Whipple Observatory basecamp staff: Jack, Ryan, Emmet, Danny, Cesar, Gene, Dan, Karen, and Steve- thank you all for everything you do to keep the Observatory running, VERITAS humming, and the mad scientists in check.

My fellow Clemson graduate students, thank you for my sanity. In the grip of sleep deprivation and crippling self-doubt, it is comforting to know I'm not alone.

Finally, I must thank the SAO Predoctoral Fellowship and all those associated with it, for their support in advancing my research goals and my life.

TABLE OF CONTENTS

Table of Contents (Continued)

Page

Table of Contents (Continued)

Page

LIST OF TABLES

LIST OF FIGURES

List of Figures (Continued)

CHAPTER 1

SUPERNOVA REMNANTS AT VERY HIGH ENERGIES

1.1 Introduction

The nature and physics of supernova remnants (SNRs) is an important subfield of astronomy. The explosive death of stars both enriches the Galaxy with new elements and releases an enormous amount of energy into its surroundings. As with most astrophysical objects, the primary means of understanding supernova remnants is by intercepting and studying light and particles emitted by the object. Of particular interest is the feasibility of SNR as efficient particle accelerators.

The origins of supernova remnants are discussed in Section 1.2. In Sections 1.3 and 1.4, the various types and evolutionary stages of SNR are explored. Section 1.5 covers the means by which SNR are thought to produce very high energy cosmic rays and photons. Finally, the specific supernova remnants covered in this work are discussed in Section 1.6

1.2 Supernovae

A supernova remnant is an expanding nebula of gas that is the direct result of the explosive death of a star. To understand the nature of supernova remnants it is important to understand how they begin as supernovae.

The conventional supernova (SN) classification scheme is primarily based on the absence or presence of specific absorption lines in their optical spectra. Broadly, hydrogen absorption lines are absent in Type I SNe and present in Type II. Type I SNe are further subdivided according to the absence or presence of silicon and helium lines; Type Ia have silicon lines, Ib have helium but no silicon, and Type Ic lack both. Further classes exist but are typically relevant to only a small subsample of objects (e.g., [Kamper and van den Bergh 1976],[da Silva 1993]).

White dwarf supernovae are associated with the Type Ia class. These supernovae are the result of a white dwarf star in a binary system accreting sufficient

matter from its companion to overcome the electron degeneracy pressure which supports the white dwarf under its own gravitational mass (Chandrasekhar 1931). The theoretical universality of this mass limit- 1.38 $M_{\odot}$, known as the Chandrasekhar Limit- leads to the idea that Type 1a supernova are all of the same absolute magnitude and thus useful as standard candles in determining distances to host galaxies (e.g., [Branch and Miller 1993]).

Core-collapse supernova, which make up the Type II and Type Ib/c spectral classes, occur when the core of a massive star ($\geq 8\ M_{\odot}$) can no longer support itself against gravitational collapse. Variation in the end stage of the star's life and the mass-loss history of the star lead to differences in composition and hence the absence or presence of the different atomic lines in the resulting supernova's spectrum. High mass stars evolve quickly through their core-burning fusion processes until an electron-degenerate ^{56}Fe core remains. Lacking a sustainable fusion reaction, if the core's mass exceeds the Fermi pressure a cascade reaction of electron-capture occurs and the core collapses into a neutron star or black hole. The supernova explosion itself is powered by the neutrinos released as a product of the core collapse and the near-elastic bounce of in-falling stellar material from the neutron star's surface. While understood in principle, this explosion mechanism has proven difficult to model.

1.3 Types of Supernova Remnants

Supernova remnants are divided into several classes based on their observational properties. For a full review, see Vink (2004).

Shell Remnants: These remnants are defined and dominated by emission from the outer shocked ejecta and swept-up material. Due to limb brightening, remnants of this type tend to appear as a ring of emission in radio and X-ray.

Crab-like Remnants: Defined by the archetypical Crab Nebula, these remnants are dominated by a nebula powered by a pulsar-driven wind (PWN). Plerions appear as filled irregular forms in X-ray and radio and lack line emission.

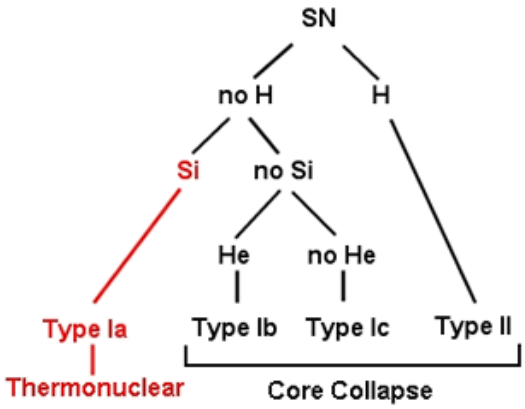

Figure 1.1 This is a breakdown of the schema by which supernova are roughly categorized by their optical absorption lines.

Remnants with pulsars are the result of core-collapse SN, though not all core-collapse SN produce pulsars.

Composite Remnants: As their name suggests, composite remnants appear as a combination of Crab-like and shell remnants. Their appearance depends on the wavelength in which they are observed. Composite remnants are further subdivided into two types. Composite remnants in which both a shell appears in synchrotron radio emission and central thermal emission appears with line emission in the X-ray are referred to as *thermal composites*. In *plerionic composites*, line emission appears in and near the outer shell, but they are otherwise Crab-like in radio and X-ray.

1.4 Remnant Evolution

The material released in a supernova explosion expands and evolves through a series of phases in which different gross physical processes dominate the behavior of the ejecta (Chevalier 1977). Despite differences in the original supernova, all remnants appear to go through the same basic phases. We refer to the evolving system of ejecta, stellar remnant and swept-up material as a supernova remnant.

These phases can be used to determine the approximate time since the explosion of observed supernova remnants. The observable remnants of historical supernovae can be linked to historical observations and an exact date can be established for the original event. Note that distinction amongst these phases is largely convention. The physical reality of any snapshot in time of the evolving remnant is likely to be some intermediate state between two phases.

The first stage of a remnant's evolution is the ejecta dominated (ED) or free expansion phase. During the ED phase the ejecta expand with a uniform velocity, leaving a lower density interior space behind it. The duration of this phase is determined by the mass and expansion velocity of the ejecta and the density of the surrounding media. The ED stage ends when the mass of shocked interstellar or circumstellar material swept up by the ejecta is comparable to the original ejecta mass. At this point, the remnant enters a period of adiabatic expansion called the Sedov-Taylor phase. The slowing due to the swept up material leads to a second shock which propagates backward through the ejecta. This reverse shock slows the ejecta material while compressing and heating it (Charles and Seward 1995).

During these two early stages, the temperature of both the ejecta and the shocked material is too high ($>2\times10^5$ K) to allow for efficient radiative processes. This is due to the complete ionization of the material in most of the remnant, disallowing line emission. The radiative phase is characterised by the recombination of ions into atoms capable of radiation via electron-transition at optical and UV wavelengths. This allows the remnant to effectively radiate away energy. While momentum conservation is naturally maintained throughout all phases, this phase is also referred to as the "momentum conserving" phase. This distinguishes it from the earlier phases in which both the energy and momentum of the system are conserved. At the end of the radiative phase, the remnant enters the final stage of its life, fading out at all wavelengths and eventually blending with the interstellar medium.

1.5 Cosmic Ray Acceleration

That supernova remnants are the primary source of galactic cosmic rays is the generally accepted theory. Indeed, measurement of non-thermal X-ray emission in several supernova remnants provides direct evidence of populations of electrons accelerated to cosmic ray energies. The evidence for acceleration of hadrons, however, is thus far less direct.

Supernova remnants were first proposed as cosmic ray accelerators based primarily on energetics (Ginzburg and Syrovatski 1964). Given the apparent spatial isotropy of cosmic rays, we can calculate the total cosmic ray energy for particles up to $\sim 3 \times 10^{15}$ eV to be

$$E = \rho_{CR}\, V_G \sim (10^{-11} \text{ ergs cm}^{-3}) \times (3.0 \times 10^{64} \text{ cm}^3) = 3 \times 10^{53} \text{ ergs} \qquad (1.1)$$

where V_G is the volume of the Galaxy and ρ_{CR} is the cosmic ray energy density in our Galaxy. If cosmic rays are trapped within our Galaxy by the galactic magnetic field for $\sim 10^{14}$ s, the rate of energy loss is $E_{loss} = 3 \times 10^{39}$ erg s^{-1}. This energy must then be provided by any hypothetical cosmic ray accelerator in order to maintain the cosmic ray energy density. We can calculate the necessary efficiency of cosmic ray acceleration in SNR as

$$\Theta = \frac{E_{loss}}{E_{SN} R_{SN}} \sim 3\% \qquad (1.2)$$

where R_{SN} is the galactic SNR rate of ~ 3 per century and E_{SN} is the total SN energy (typically estimated to be of $\sim 10^{51}$ ergs). While this energy budgeting is not sufficient evidence to claim SNR as the source of Galactic cosmic rays, no other source is known to produce sufficient energy to maintain this energy density.

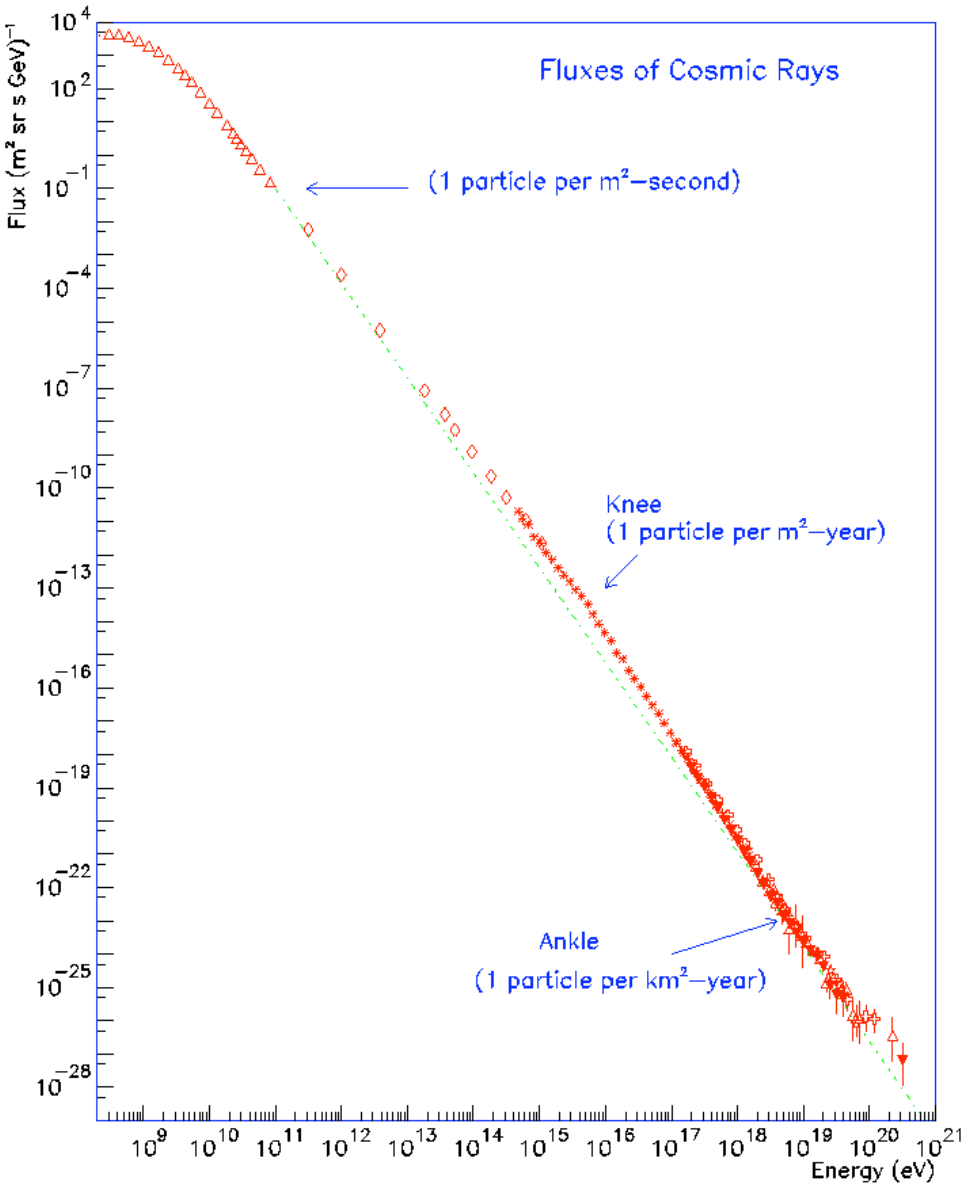

Figure 1.2 This is a spectrum of cosmic rays built from a compilation of cosmic ray experiments. The "knee" and "ankle" indicate changes in the spectral index from ∼2.7 below the knee to ∼3.0 between the knee and ankle and to ∼2.8 above the ankle. Supernova remnants are the presumed source of cosmic rays at energies below the knee.Taken from [Cronin et al. 1997]

1.5.1 Diffusive Shock Acceleration

The basis of most modern cosmic ray acceleration theories was set forth by Fermi (1949). Fermi originally proposed that particles could gain energy through repeated elastic scatterings off of moving interstellar gas, arguing that "head-on" collisions (in which the scattering particle gains energy) would be more common than "head-tail" collisions (in which the scattering particle loses energy). While this theory accurately predicts a power-law spectrum for the scattered particles, it fails in two regards. First, the scattering time for such a particle would be too long to maintain the galactic cosmic ray energy density. Secondly, the proposed process would be unable to accelerate heavy ions up to cosmic ray energies without fragmentation.

Bell (1978a) and Blandford and Ostriker (1978) proposed the currently accepted solution. Particles could gain the necessary energy via repeated crossing of an astrophysical shock. Elastic scattering would occur off of magnetic inhomogeneities both upstream and downstream of the shock. This process is referred to as *diffusive shock acceleration*. At each crossing, the momentum gain would be

$$\Delta p = \frac{4}{3}(\beta_u - \beta_d)p \tag{1.3}$$

where β_u and β_d are the upstream and downstream shock velocities in terms of c, respectively and p is the particle momentum (Bell 1978b). The probability of escape after each (perpendicular) crossing is

$$P = \frac{4c\beta_u}{v_p} \sim 4\beta_u \tag{1.4}$$

for a relativistic particle ($v_p \sim c$). The probability of a particle scattering l times before escaping and thus achieving energy E_l is

$$ln(P_l) = l \times ln(1 - 4\beta_u) \tag{1.5}$$

The particle differential spectrum can then be derived to be

$$N(E)dE = N_o \left(\frac{E}{E_o}\right)^{\frac{2+r}{1-r}} dE \tag{1.6}$$

where r is the compression ration β_u/β_d, E_o is the particle injection energy, and $N_o = (\mu - 1)/E_o$. For a strong SNR shock, r $\sim$ 4. This gives a power-law index of $\sim$ 2, which is sufficiently hard to account for the cosmic ray spectrum below the knee. We thus have an argument from energetics and a plausible scenario by which SNR produce the Galactic cosmic ray spectrum.

1.5.2 Electron Acceleration

In the case of pulsar wind nebulae (PWN), leptonic emission is expected to be dominant, though Arons and Tavani (1994) argue that diffusive shock acceleration cannot account for the leptonic acceleration. In PWN, the leptonic population is the result of pair production in the pulsar's magnetic field. Diffusive shock acceleration requires that the magnetic fields lie almost perpendicular to the flow of the material (generally, roughly parallel to the shock) which is not the case throughout the PWN shock. Instead, Arons & Tavani find that the acceleration mechanism is the absorption of synchrotron radiation emitted by heavy ions gyrating in the post-shock material. The electron-positron pairs absorb this radiation at their relativistic cyclotron frequencies.

Interestingly, the geometry of PWN may prove crucial in separating out potential pulsar-driven TeV emission from SNR shock-driven emission. The shock radius of a PWN is determined by

$$r_w^2 = \frac{\dot{E}}{4\pi\eta cp} \tag{1.7}$$

where $\dot{\text{E}}$ is the rate of energy injection into the wind, η is the fractional spherical area covered by the wind and p is the external pressure (Slane 2002). Typical values are $\sim 0.1pc$, considerably more compact than a typical SNR blast wave only a few decades after explosion. Thus, given sufficient angular resolution emission

from PWN shock-fronts should be readily distinguishable from SNR shock-front emission.

1.5.3 TeV Emission

We have accounted for the possibility of cosmic ray production in SNR for both the hadronic and leptonic case. The difficulty in confirming this production observationally lies in the charged nature of the particles thus produced. Charged cosmic rays up to (10^{15} eV) are deflected significantly by the Galactic magnetic field. The resultant isotropy of cosmic rays precludes the direct detection of the source of Galactic cosmic rays. However, these relativistic particles will produce very high energy gamma rays at or near their point of origin through multiple processes.

In the hadronic case, collisions between the relativistic protons/nuclei and the ambient medium will produce pions. The π^0 decays primarily (98.8%) via

$$\pi^0 \rightarrow 2\gamma \tag{1.8}$$

on a timescale of $\tau = 8.3 \times 10^{-17} s$ (Particle Data Group et al. 2008) - fast enough to consider the photon origin as the collision site. The collision target may be supernova ejecta or swept-up or undisturbed circumstellar medium. A local region of high density target- a nearby molecular cloud, for example- would serve to enhance the resultant TeV emission. This would be a strong indication of hadronic, rather than leptonic, emission.

High energy electron populations up to 100 TeV are observed via their synchrotron emission in several supernova remnants ([The et al. 1996],[Borkowski et al. 2001]). These electrons can generate VHE gamma rays through inverse Compton scattering of ambient photons off of electrons. This process leads to a power-law spectrum degenerate with the hadronic emission, and thus a key difficulty in the discrimination of hadronic from leptonic signal in TeV emission.

1.5.4 Observational Prospects

The viability of supernova remnants as TeV emitters is well established- but to what extent is this flux observable?

In the case of hadronic emission the brightness of a TeV source can be predicted from a few parameters. The gamma-ray luminosity due to π^0 decay can be estimated as (Drury et al. 1994)

$$L_\gamma = \int q_\gamma \; n \; E_{CR} \; d^3r \approx q_\gamma \; M_{SNR} \; E_{CR} = q_\gamma \Theta \; E_{SN} \tag{1.9}$$

where Θ is again the fraction of the supernova energy E_{SN} convert to cosmic ray energy and

$$q_\gamma = \frac{Q_\gamma}{n E_{CR}} \tag{1.10}$$

where Q is the production rate per unit volume of gamma rays. From [Aharonian et al. 1994], The flux at Earth can then be expressed as

$$F(\geq E_{thresh}) = f_\alpha \times 10^{-10} \; \Theta \; \mathrm{A} \; \left(\frac{E}{1 \text{ TeV}} \right)^{-\alpha+1} \text{cm}^{-2}\text{s}^{-1} \tag{1.11}$$

where f_α is a number ~ 1 which depends on the gamma-ray spectral index α, and A is a dimensionless amplitude scaling factor depending on the physical values of the remnants

$$\mathrm{A} = \left(\frac{E_{SN}}{10^{51} \text{ ergs}} \right) \left(\frac{d}{1 \text{ kpc}} \right)^{-2} \left(\frac{n}{1 \text{ cm}^{-3}} \right) \tag{1.12}$$

where n is the density of the ambient medium. The author has collected the best estimates from the literature for these physical values in Table 1.1 and the values for A used in this work are given in Table 6.1. Where no values are available, the values used are $n = 0.1$ and $E_{SN} = 1$.

1.6 VERITAS Targeted Remnants

1.6.1 Crab Nebula

The Crab Nebula (M1, G184.6-5.8) is the remnant of the historical SN 1054 recorded by Chinese astrologers and rediscovered as an optical remnant by English astronomer John Bevis. The Crab is the archetypical PWN, with little or no contribution from a classical supernova shock. For a recent review, see Hester (2008).

The Crab's morphology is highly varied at different wavelengths. Optical and radio images show diffuse filaments of emission which vary on short time scales (Bietenholz et al. 2004), while deep X-ray observations reveal emission from a torus of high-energy particles ringing the central pulsar and jets extending along the axis of this torus (Weisskopf et al. 2000).

The detection of the Crab Nebula was the first unequivocal detection of a TeV gamma-ray source (Weekes et al. 1989). As such, it has become the standard candle for TeV telescopes. VERITAS finds a differential spectrum which obeys a power law of form

$$\frac{dN}{dE} = f_o \left(\frac{E}{E_o}\right)^{-\Gamma} \text{TeV}^{-1}\text{cm}^{-2}\text{s}^{-1} \tag{1.13}$$

with $f_o = (3.63 \pm 0.15_{stat}) \times 10^{-11}$ and $\Gamma = 2.54 \pm 0.05_{stat}$. Other TeV telescopes report comparable values ([Aharonian et al. 2006], [Otte et al. 2008]).

Figure 1.3 Composite multiwavelength image of the Crab Nebula. Colors indicate waveband; Red = Radio, Green=optical and Blue=X-ray. Note that the pulsar-dominated center is seen primarily in X-ray synchrotron radiation, while the outer, free expanding material is seen in radio. The image is 6' across. Image Credits: X-ray: NASA/CXC/ASU/J. Hester et al.; Optical: NASA/HST/ASU/J. Hester et al.; Radio: NRAO/AUI/NSF .

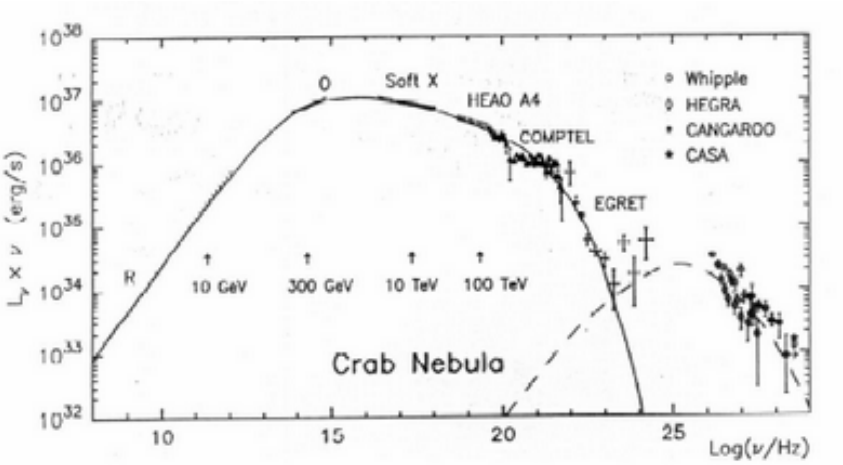

Figure 1.4 This is the broadband spectrum of the Crab Nebula, along with the theoretical curve for a leptonic-hadronic model (Image taken from: http://ihp-lx.ethz.ch/CompMethPP/magic/magicIntro.html) .

1.6.2 Cassiopeia A

Cassiopeia A (Cas A) is a well-studied middle-aged remnant of a Type IIb SN (Krause et al. 2008a). Discovered as the brightest radio source in the sky, optical studies have since constrained its age to ∼350 years, making it the second-youngest known SNR ([Thorstensen et al. 2001], [Green et al. 2008]). Dynamically, the remnant shows a strong forward and reverse shock propagating through ejecta in free expansion. A central compact object is seen in X-ray, though no evidence for a radio pulsar is found.

Evidence for a possible non-thermal electron population was seen by OSSE in the form of a hard X-ray emission tail (The et al. 1996). Chandra observations later localized X-ray synchrotron emission in filaments in the forward shock, thus strongly supporting the presence of TeV electrons interacting with Cas A's magnetic fields (Berezhko and Völk 2004).

TeV emission was first detected in Cas A by the HEGRA array (Aharonian et al. 2001a), and has since been seen by multiple major Čerenkov experiments (e.g., [Aharonian et al. 2001a], [Albert et al. 2007a], [Ergin and VERITAS Collaboration 2008]). The current VERITAS results for Cas A yield a power law spectrum with $\Gamma = 2.61 \pm 0.24_{stat}$ (Acciari et al. 2009), in reasonable agreement with both HESS and MAGIC. Atmospheric Čerenkov detectors cannot yet resolve this remnant (d ∼ 4'), so determining the origin within the remnant of the TeV photons is not yet possible. While the known TeV electrons are the presumed source of these photons, Cassiopeia's high radio brightness implies a large magnetic field ($B_{ave} \sim 0.5$ mG, [Vink and Laming 2003]), leading to a lower relativistic electron population for a given measured radio brightness. This then limits the TeV contribution from inverse Compton scattering, implying at least a partially hadronic origin for the measured TeV flux.

1.6.3 Tycho's SNR

SN 1572 was observed by the astronomer Tycho Brahe as a "stella nova." The remnant of this Type 1a supernova, G120.1+1.4, is thus better known as Tycho's

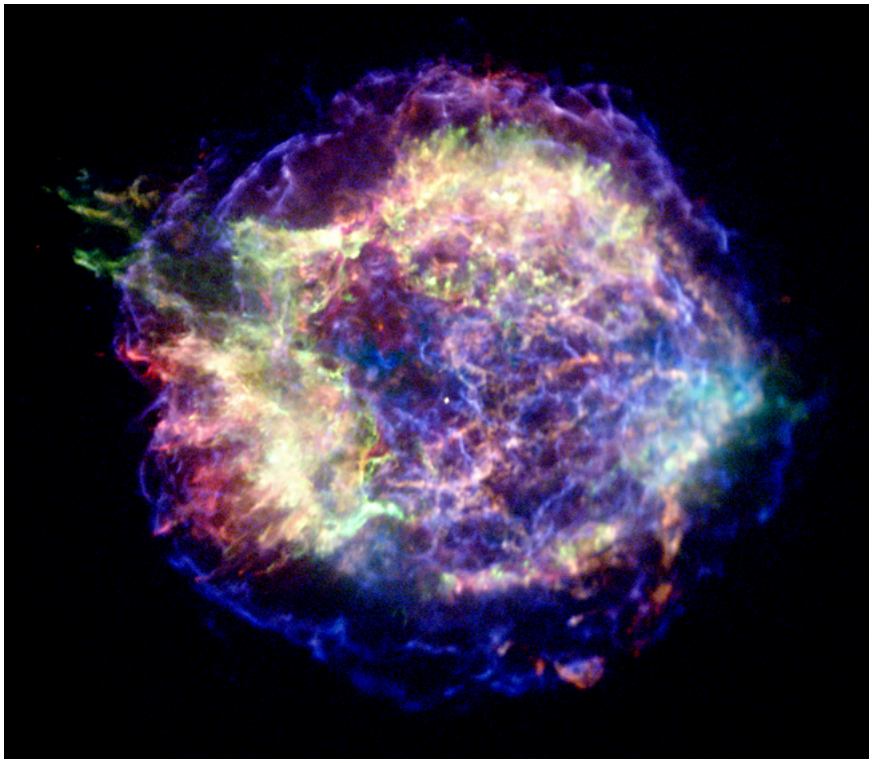

Figure 1.5 This is an image of Cassiopeia A as seen in X-rays by the Chandra X-ray Observatory. Color indicates energy; Red: 0.5-1.5 keV; Green: 1.5-2.5; Blue 4.0-6.0. The outer and reverse shock are clearly visible, as are the filaments of line-dominated emission. Faintly visible is the jet extended beyond the outer shock in the northeast. (Image Credit: NASA/CXC/MIT/UMass Amherst/M.D.Stage et al.)

SNR, or simply Tycho. The expansion of the supernova ejecta into a relatively clean volume of space has left a classical spherical shell remnant of radius 4'. Since Type Ia supernova leave no compact object, there is no expectation of a pulsar or wind nebula, and none is seen.

Tycho is another well studied remnant at nearly every wavelength. Recent spectral observations of SN 1572's light-echo have confirmed it as a Type 1a supernova (Krause et al. 2008b). Radio observations reveal a clumpy, circular remnant with a well-defined brightened outer shell (Dickel et al. 1991). X-ray observations of Tycho seem to be consistent with thermal bremsstrahlung emission with a harder

X-ray tail (Fink et al. 1994; Petre et al. 1999). This tail is taken as an indication of a non-thermal electron population up to ∼100 TeV. Given a sufficient seed photon population, this could be a source for inverse Compton-scattered gamma rays. Further, the morphology of X-ray emission and the thinness of the outer shock appear inconsistent with a purely adiabatic expansion and can be explained by energy lost to cosmic ray acceleration (Warren et al. 2005).

Tycho was observed extensively by the previous generation of Atmospheric Čerenkov Telescopes. HEGRA's observations of ∼ 65 hours during 1997 and 1998 yielded no detection and a 3 σ upper limit of 5.78×10^{-13} photons cm^{-2} s^{-1}, or 3.3% Crab, above 1 TeV [Aharonian et al. 2001b].

1.6.4 W44

W44 (G34.7-0.4) is a well-studied middle-aged remnant. The remnant has an associated pulsar, PSR B1853+01, with a small pulsar wind nebula (0.5') visible in radio and X-ray synchrotron photons. The pulsar is located roughly at the center of the remnant and has no apparent effect on the remnant's dynamics. Pulsar timing observations give an apparent age of 20 kyr for the pulsar, which concurs with W44's apparent late Taylor-Sedov phase.

Radio observations show a relatively smooth emission gradient over the full extent of the remnant, only showing an enhanced shell in the northeast. The remnant's overall shape is roughly elliptical, with angular dimensions of ∼ 25' × 35' in the radio. This shape, in conjunction with the enhanced shell in the NE, may indicate interaction with some enhanced density in the NE as the remnant expands (Giacani et al. 1997).

W44 shows an unusual central brightening in X-rays beyond what is expected for a thermal composite supernova remnant. Chandra observations seem to favor both enhanced entropy-mixing via thermal conduction or bulk motion in the remnant interior and a centrally-enhanced metallicity as explanations for the central brightening.

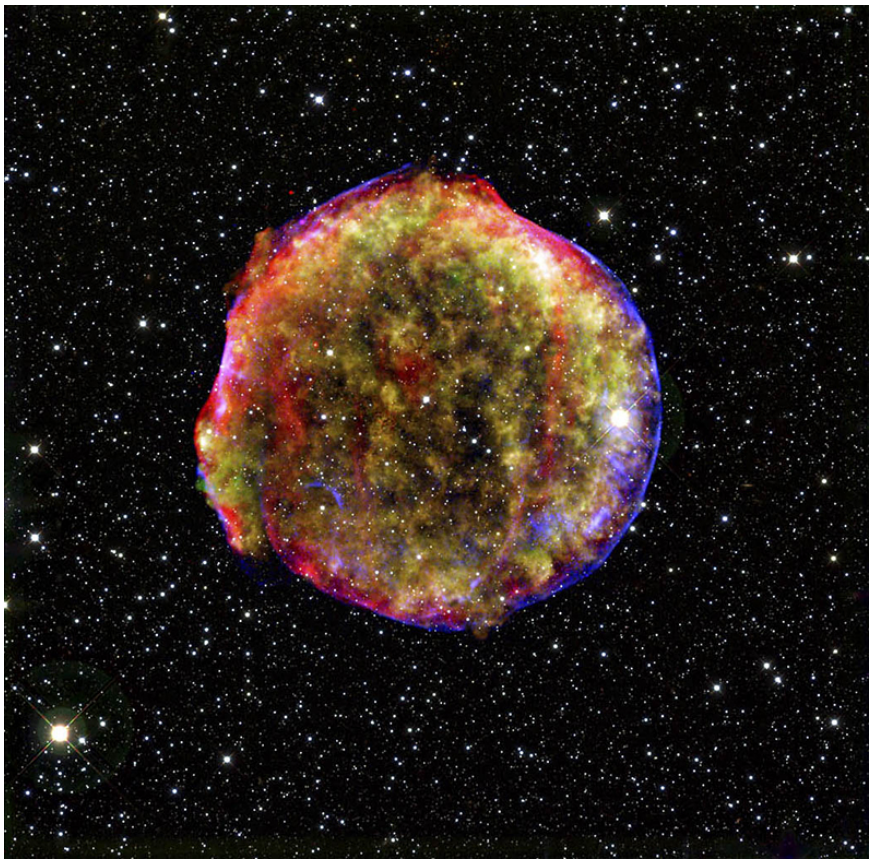

Figure 1.6 This is a multiwavelength image of Tycho's SNR in infrared, optical and X-ray. The non-thermal X-ray emission from high energy electrons in the outer blast wave is visible as a sharp blue edge to the remnant. (Image Credit: X-ray: NASA/CXC/SAO, Infrared: NASA/JPL-Caltech; Optical: MPIA, Calar Alto, O.Krause et al.)

The southern extent of W44 lies within the 95% confidence region of the EGRET detected source 3EG J1856+0114 (Esposito et al. 1996). If this association is valid, there must be a sharp cutoff in the gamma-ray spectrum between the hard spectrum ($\Gamma = 1.93 \pm 0.10$) seen by EGRET at MeV energies (Hartman et al. 1999) and the existing upper limits in the TeV regime. CANGAROO observations in the TeV find no emission and indicate an upper limit of F (E $>$ 1.36 TeV) $<$ 3.6 $\times 10^{-12} \gamma$ cm$^{-2} s^{-1}$ [Yukawa 2008].

1.6.5 CTB 109 (G109.1-1.0)

CTB 109 has a semicircular morphology, with a clear incomplete shell in radio and X-ray in the west, starkly contrasted with a lack of any extended emission in the east. Despite the presence of a giant molecular cloud (GMC) complex it is not believed that the remnant's apparent shape is due to obscuration in the west as absorption would be negligible in the radio. Thus it is more likely that the western shock has simply been stopped by the GMC complex on that side [Tatematsu et al. 1987].

Several features stand out in X-rays in CTB109. The associated anomalous X-ray pulsar 1ES 2259+586 is the brightest feature and has had outbursts similar to those of soft gamma-ray repeaters. In the east is the incomplete X-ray shell, interior to which is the Lobe, a bright diffuse X-ray region with no apparent association to the pulsar (Sasaki et al. 2004). Emission from the Lobe appears to be thermal and shows little spectral variation from the surrounding regions. This seems to indicate shock interaction with an interstellar cloud, rather than a high-density molecular region (Sasaki et al. 2006). It also rules out earlier suggestions that the Lobe is the result of material excited by a pulsar jet.

CTB 109's close proximity to, and apparent interactions with, a GMC complex give it an enhanced target density for any hadronic-cosmic rays produced in the shocks. The lack of a detected synchrotron signal indicating a population of relativistic electrons make it less attractive as a source of leptonic TeV emission; however, this might make the source an ideal candidate for unambiguous hadronic cosmic-ray production.

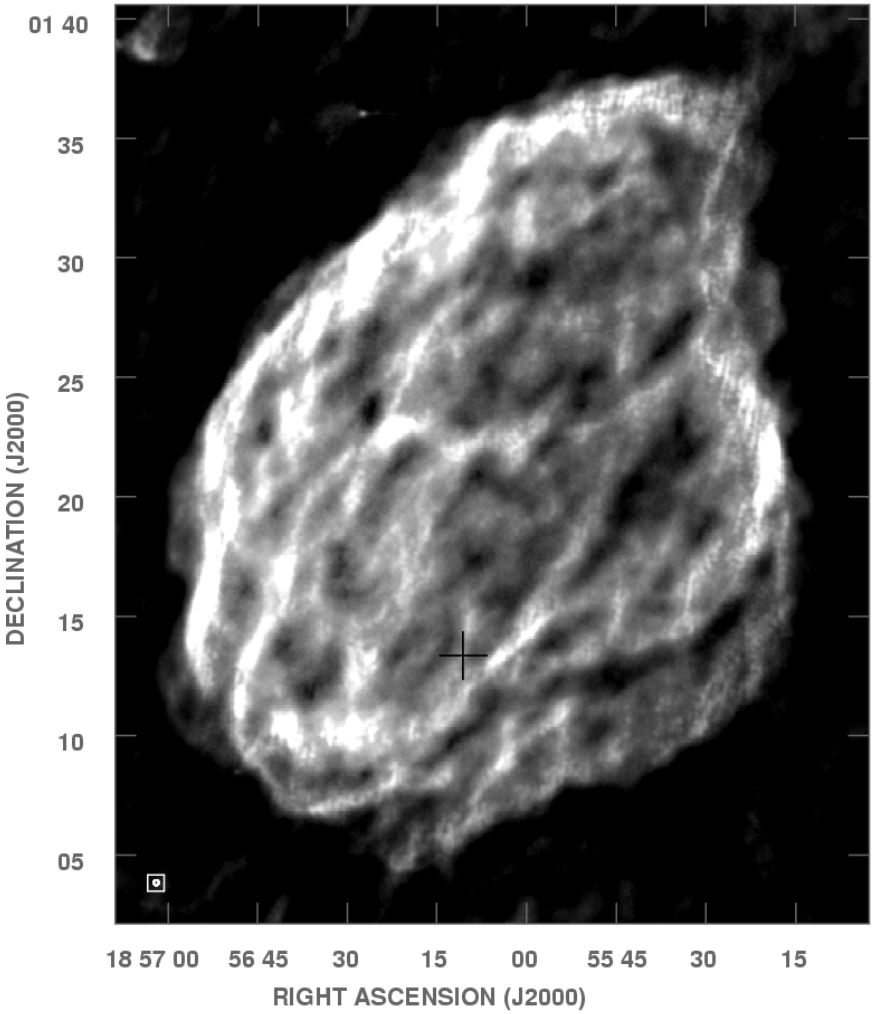

Figure 1.7 This is an radio image of W44 from VLA observations at 327 MHz. The image brightens at the eastern boundary, likely due to molecular cloud interaction. The black cross indicates the pulsar location. (Image Credit: Castelletti et al. (2007))

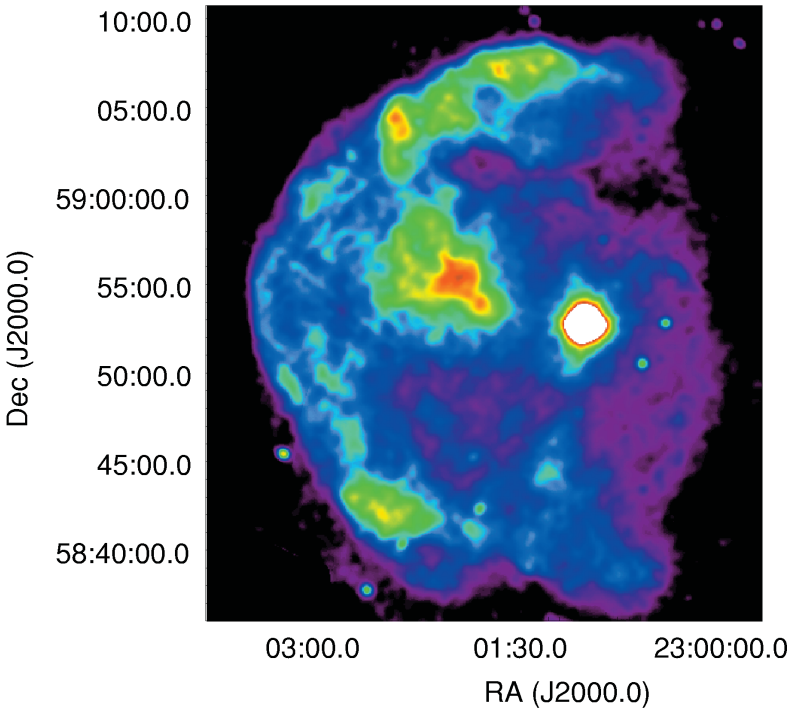

Figure 1.8 Intensity Map of CTB109 in the X-ray (0.3-0.4 keV). Clearly visible is the remnant's semi-circular extension around the bright X-ray pulsar. The Lobe is the diffuse bright patch at R.A. = 23:02, decl. = +58°55'. Image taken from [Sasaki et al. 2004].

1.7 Cygnus Region Remnants

The Cygnus region was selected as the target of the VERITAS Sky Survey Key Science Project for the first two years of operation. The region and survey are discussed in more detail in Chapter 3.

Green's catalog lists 8 remnants within the first half of the Survey region which have been studied to varying degrees. In many cases, observations of these remnants are complicated by proximity to other extended sources including complex molecular regions, Wolf-Rayet Stars and star-forming regions. We discuss the remnants below, focusing on general physics and observable properties with possible bearing on TeV emission. It is important to point out that most of the remnants within the Cygnus region are not necessarily considered good prospects for TeV emission, with the possible exceptions of CTB 80, CTB 87 and γ Cygni. Large and/or poorly constrained distances in the case of G67.7+1.8, G69.7+1.8 and G76.9+1.0 likely preclude any meaningful constraints on emission. Further, remnants such as CTB 80 are more properly considered PWN, and any detected emission must be interpreted within the context of particle acceleration by the central pulsar. The analysis of all the Survey remnants here is primarily an attempt to fully exploit the available data as a potential means of discovery.

1.7.1 G67.7+1.8

SNR G67.7+1.8 was discovered with number of other SNR as a part of the 327 MHz Galactic Plane Survey (Reich et al. 1988). Despite being only recently discovered, G67.7+1.8 has been observed in a number of wavelengths. Optical observations imply an explosion energy below the canonical value of 10^{51} ergs (Mavromatakis et al. 2001). In radio, the source shows a bilateral distribution, while in X-rays the remnant shows as centrally filled. Distance estimates are poorly constrained ($\sim$7-27 kpc), though optical observations make a distance over 17 kpc unlikely due to extinction values. There are no published TeV observations for this source.

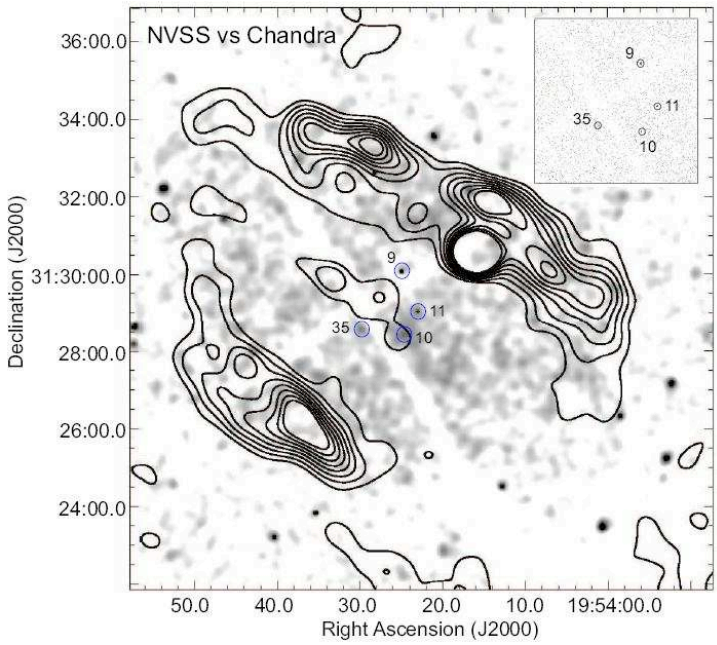

Figure 1.9 Radio map of G 67.7+1.8 overlaid onto Chanda X-ray data (0.5-0.8 keV). The bilateral distribution of radio emission is clearly not correlated to the centrally peaked X-ray emission. Point sources near the remnant center are circled in blue. Image taken from Hui and Becker (2008)

1.7.2 G68.6-1.2

G86.6-1.2 was discovered by Loiseau et al. (1988) and identified as a SNR by its linearly polarized emission at 2695 MHz. A diffuse, circular appearance in radio seems to imply a shell-type SNR; however there is no firm identification of the remnant type to date and no pulsar has been detected ([Lorimer et al. 1998], [Kothes et al. 2006]). There are no published TeV observations for this source.

1.7.3 CTB80/G69.0+2.7

CTB 109 is an interesting case of a mixed morphology SNR, having both an extended diffuse component and a central nebula with an embedded known pulsar. In radio, the SNR appears as an irregular diffuse structure with a spectrally flat plerion in the southwest at most wavelengths (Angerhofer et al. 1981), while

HI emission reveals a more regular shell of emission (Koo et al. 1990) . It has been suggested that the pulsar's proper motion has caught up to the decelerating (roughly circular) shock in the southwest, causing one of the unusual extensions which characterize the radio emission.

MAGIC has taken observations of CTB 80 and PSR B1951+32, searching for both continuous and pulsed emission. Despite strong predictions of TeV emission due to PWN/envelope interaction (Bednarek and Bartosik 2003), no detection is made and an upper limit of $1.5 \times 10^{-11}\gamma$ cm^{-2} s^{-1} is placed on the steady emission (Albert et al. 2007b).

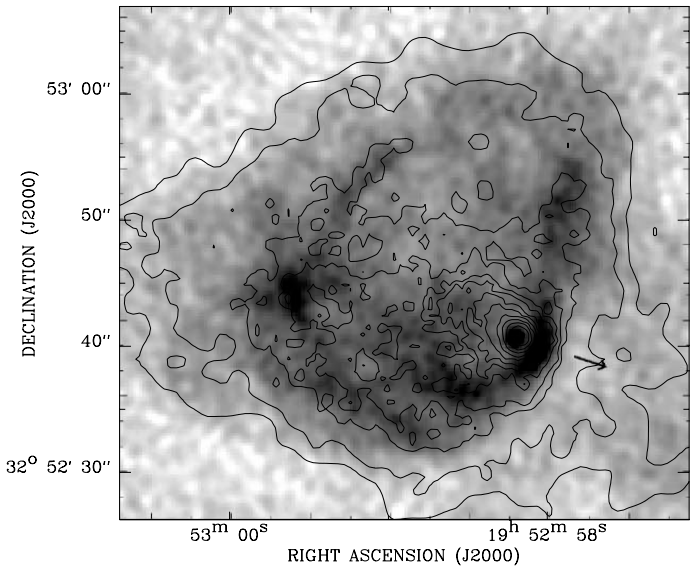

Figure 1.10 This is a 20 cm line radio map of CTB80, overlaid with contours of the X-ray emission seen with the Chandra X-ray Telescope (0.3-8.0 keV). The arrow indicates the pulsar's proper motion. The PWN is clearly visible embedded in the SNR ejecta in the western part of the remnant. Image taken from Li et al. (2005).

1.7.4 G69.7+1.0

G86.6-1.2 was discovered as part of the 2.7 GHz Survey as a poorly resolved source ~ 0.25 degrees in diameter (Reich et al. 1988). ROSAT found X-ray emission in the vicinity, but deeper X-ray observations revealed a large extension in the X-ray not likely to be associated with the remnant (Yoshita et al. 2000). No pulsar has been detected within the remnant (Lorimer et al. 1998), and no TeV searches have been reported.

1.7.5 G73.9+0.9

In the radio, this remnant appears as a diffuse shell with a centrally peaked shell to the east, possibly indicating a PWN (Kothes et al. 2006). The remnant is characterized in the optical by diffuse emission. An approximate distance of ~ 0.5 - 2.0 kpc is given by kinematic studies (citation), and an upper limit of $\sim 1.5 \times 10^{-3}$cts s^{-1} is set on X-ray emission by the ROSAT All-Sky Survey (Mavromatakis 2003). The remnant is only tentatively identified as a shell. No TeV searches have been reported.

1.7.6 CTB87/G74.9+1.2

CTB 87 is a centrally filled remnant considered to be a PWN, though no central point source or associated pulsar is detected (Kothes et al. 2006). It has a spectral index of ~ 2 in the X-ray, consistent with other Crab-like plerions (Asaoka and Koyama 1990). While a nearby giant molecular cloud is seen in CO emission, there is no indication of shock-cloud interaction (Cho et al. 1994). Only limited X-ray data exists on this source, and no TeV observations have been reported.

1.7.7 G76.9+1.0

The structure of G76.9+1.0 appears to vary at different radio frequencies, with a diffuse disk showing at 1.49 GHz, and a two-lobe structure appearing at 4.86 GHz. G76.9+1.0 may be a young shell SNR, or it may in fact be a pure PWN [Landecker et al. 1993]. The source has not been observed at higher energies.

1.7.8 γ Cygni SNR/G78.2+2.1

The supernova G78.2+2.1 (referred to as the γ Cygni because of its line of sight proximity to the eponymous, unrelated star) is perhaps the best studied of the Cygnus region SNR. The remnant appears as a rough circle in X-rays and gamma rays, with two pronounced arcs.

The brightest GeV gamma-ray source, 3EG J2020+4017, lies within the γ Cygni remnant (Esposito et al. 1996). Gamma-ray emission is not seen over the full extent of the remnant, so 3EG J2020+4017 is assumed to be an associated pulsar. The soft gamma-ray source has a flux of $1.24 \pm 6.7 \times 10^{-6}$ γ cm^{-3} s^{-1} and a spectral index of -2.08 ± 0.04, with a break at $\geq$ 4 GeV (Hartman et al. 1999). HEGRA observations put an upper limit of 12% Crab flux above 600 GeV (Aharonian et al. 2002). More recently, both the Fermi LAT instrument and the ground-based Milagro experiment have detected gamma-ray emission from the vicinity of this pulsar (Abdo et al. 2009).

Remnant	RA (h m s)	Dec	Size (')	Dist. (kpc)	Type	n (cm^{-3})	VHE Flux (10^{-12} γ cm^{-2} s^{-1})
CTB109 (G109.1-1.0)	23 01 35	+58 53	28	3.0	Shell	0.9 [1]	—
Cas A (G111.7-2.1)	23 23 26	+58 48	5	3.4	Shell	1	F(>300 GeV) = 2.5 [3]
Tycho (G120.1+1.4)	00 25 18	+64 09	8	2.4	Shell	1	F(> TeV) < 0.58 [4]
Crab Nebula (G184.6-5.8)	05 34 31	+22 01	7 × 5	2.0	PWN	1	F(>300 GeV) = 151 [3]
W44 (G34.7-0.4)	18 56 00	+01 22	35'×25	2.8	Pler. Comp.	1	F (> 1.36 TeV) < 3.6 [5]
G67.7+1.8	19 54 32	+31 29	9	7-17	Shell	13.0 [2]	—
G68.6-1.2	20 08 40	+30 37	28×25	8.1	Unknown	1	—
CTB 80 (G69.0+2.7)	19 53 20	+32 55	80	1.5-2.5	Composite	1	F(> 140 GeV) < 15 [6]
G69.7+1.0	20 02 40	+32 42	16	14.4	Shell	1	—
G73.9+0.9	20 14 15	+36 12	22	0.5 - 2.0	Shell	1	—
CTB87 (G74.9+1.2)	20 16 02	+37 12	8×6	2.0	Composite	1	—
G76.9+1.0	20 22 20	+38 43	9×12	12.6	Unknown	1	—
γ Cygni (G78.2+2.1)	20 20 50	+40 26	60	1.5	Shell	1	F(> 600 GeV) < 17 [7]

Table 1.1 Summary of the SNR included in this work. Unless otherwise noted, values are from Green (2006).

[1] [Sasaki et al. 2006]

[2] [Gök et al. 2008]

[3] This work

[4] [Aharonian et al. 2001b]

[5] [Yukawa 2008]

[6] [Albert et al. 2007b]

[7] [Aharonian et al. 2002]

CHAPTER 2

THE IMAGING ATMOSPHERIC ČERENKOV TECHNIQUE AND VERITAS

2.1 A Brief History of VHE Astronomy

The earliest astronomical measurements in gamma ray were taken by instruments borne above the atmosphere by balloon (e.g., [Hulsizer and Rossi 1948], [Schein et al. 1941]. These observations, and the subsequent satellite observatories, followed an evolution parallel to that of X-ray astronomy, though with several additional difficulties. Above a few MeV, reflection of photons, even at small incidence angles, becomes effectively impossible. Thus, a gamma-ray telescope has only the effective collection area of its detector- a severe limitation compared to the enormous collection area available to ground-based optical telescopes. This difficulty is made even more pronounced by the physical limits on detectors imposed by the necessity of hoisting the detector above the atmosphere; space and mass are at a premium onboard both satellites and balloons. For this reason, the development of very high energy (VHE) gamma-ray astronomy took place on the ground, and has had more in common with the field of cosmic ray astronomy than with lower energy gamma ray and X-ray astronomy. The possibility of studying VHE gamma rays from cosmic sources from the ground was first proposed by Cocconi (1960). Earlier experimentation by Galbraith and Jelley (1953) had shown the feasibility of detecting the flashes of Čerenkov light from cosmic rays.

The earliest major Čerenkov telescope installation was deployed by a group of Soviet scientists from the Lebedev Institute in the Crimea from 1960-1964. Observations were carried out on a number of sources as suggested by Cocconi (1960), though no sources were detected. The Crimean experiment consisted of an array of 12 small-scale light collectors, each outfitted with a single PMT. This experiment, like earlier methods, searched for directional anisotropies in the arrival directions of

air showers- the key difficulty being that there was no real way to discern between cosmic-ray and gamma-ray induced showers.

The first unambiguous detection of a TeV source via Čerenkov air showers was of the Crab Nebula in 1989 (Weekes et al. 1989). This detection was made by the Whipple Observatory's 10 m telescope. The Whipple 10 m was built in 1968 on Mount Hopkins in southern Arizona as the first large optical reflector dedicated to gamma-ray astronomy. A later upgrade added a camera consisting of 37 photomultiplier tube (PMT) pixels, which allowed for the discrimination between different types of air showers by the images produced. This technique, first proposed by Turver and Weekes (1978) and now standard for ground-based VHE telescopes, is referred to as the Imaging Atmospheric Čerenkov Technique (IACT). Other "second generation" atmospheric Čerenkov telescopes employing this technique include the very successful HEGRA ACT (Aharonian et al. 1993) which first detected the supernova remnant Cassiopeia A (Aharonian et al. 2001a), and the CANGAROO-I and -II systems [Kawachi et al. 2001].

The current generation of ground-based VHE telescopes is dominated by arrays of IACT telescopes, similar to VERITAS as presented in 2.6. The individual arrays are discussed in 2.5.1

2.2 Čerenkov Radiation

Čerenkov radiation occurs when a charged particle exceeds the speed of light in a dielectric medium- that is:

$$v = \beta c \ , \ \beta > \frac{1}{n} \tag{2.1}$$

where n is the refractive index of the medium. The phenomenon was first discovered as the emission of blue light by water when gamma radiation passed through it (Čherenkov 1937). Any given charged particle moving through a dielectric medium will undergo Coulomb interactions with nearby molecules, locally polarizing the medium. This polarization will switch on and off as the particle passes, causing

Figure 2.1 Photo from the inauguration of the Whipple 10 m on October 23, 1968 from the Smithsonian Institute Archive. The people in the foreground are, left to right, Tucson mayor James Corbitt, Smithsonian Astrophysical Observatory Director Dr. Fred Whipple and Rep. Morris K. Udall.

the molecules to radiate. In the case of a slow ($v \ll c$) particle, this interaction is symmetric around and along the particle's trajectory, and thus no radiation escapes.

In the case of a relativistic particle, however, the particle's electric field is distorted by its velocity. While radial symmetry is maintained a dipole is generated along the axis of the particle's trajectory, leading to detectable radiation emission. The resultant wavefront is emitted at an angle θ to the particle's trajectory such that:

$$\cos\theta = \frac{1}{\beta n} \tag{2.2}$$

which is only valid for $\beta > 1/n$, as stated before. The maximum angle will occur where v = c, or:

$$\theta_{max} = cos^{-1}\left(\frac{1}{n}\right) \tag{2.3}$$

For the Earth's atmosphere at an altitude of 10 km, n ≈ 1.000 096, and the critical angle becomes $\theta \sim 0.8\,\text{deg}$. More importantly, we can determine the minimum relativistic energy needed for a particle to produce Čerenkov radiation by setting $\theta = 0$:

$$E_{min} = \frac{mc^2}{\sqrt{1 - \frac{1}{n^2}}} \tag{2.4}$$

For an electron at sea level, $E_{min} \sim 21$ MeV and $\theta \sim 1.3°$.

The classical treatment of Čerenkov radiation gives a energy per unit path length of

$$\frac{dE}{dl} = 4\pi^2 e^2 \int_{\beta n>1} \left(1 - \beta^{-2} n^{-2}(\lambda)\right) \lambda^{-3} d\lambda \tag{2.5}$$

The λ^{-3} dependence indicates that the primary contribution is at shorter wavelengths. Since n falls below 1 at higher frequencies, the Čerenkov conditions are no longer met and emission peaks in the near UV. This also explains the bluish appearance of Čerenkov light to the human eye.

2.3 Production of Čerenkov Light in Air Showers

In extensive air showers, Čerenkov light is a result of a cascade of relativistic particles moving through the Earth's atmosphere. These particles may be cosmic rays themselves, or, more likely, the results of interactions between atmospheric particles and cosmic rays or VHE gamma rays (Weekes 2003). Since Čerenkov light is highly beamed in the forward direction, the trajectory and thus the origin of the original particle can be determined from the detected Čerenkov light. In the case of IACT telescopes, the shape of the 2-d projection of the air shower onto the detector plane can be used to determine the particle's type and direction.

The ultimate goal of the VHE astronomer is to use the detectable properties of the air shower to study the nature of the progenitor particle and, through it, the particle's source. It is necessary to look at the nature of the showers produced by different progenitors. This is typically done by extracting mean parameters from large numbers of Monte-Carlo simulated air showers (e.g., [Hillas 1995]), but what follows is a more general discussion.

2.3.1 Gamma rays

Of the various types of Čerenkov air showers, gamma rays are physically the simplest. The initial interaction event in the atmosphere is electron-positron production. The resulting high energy pair travel through the atmosphere and produce further high-energy gamma rays via bremsstrahlung as they brake against the local medium. If these photons are of high enough energies, they will also pair-produce. This process continues until the bremsstrahlung photons are no longer sufficiently energetic to pair-produce. The resulting cascade of high-energy electrons and positrons gives rise to a characteristic pulse of Čerenkov light. An example of the simulated development of a gamma-ray shower is shown in Figure 2.2.

2.3.2 Hadronic Cosmics Rays

The cosmic-ray flux incident on Earth is predominantly protons, with a significant contribution from He nuclei. A lesser fraction is from higher mass nuclei, which have been detected up to iron. A typical proton's first interaction upon entering the atmosphere is with another proton, producing a neutral and charged pion as well as some other particles

$$p_{CR} + p_{atm} \rightarrow \pi^{\circ} + \pi^{\pm} + N \tag{2.6}$$

where N is some combination of nucleonic debris. The subsequent decay of the neutral pion produces a gamma-ray pair. This pair creates an electromagnetic shower as described in 2.3.1. The EM component is the primary source of Čerenkov light on the ground in the CR induced shower. The charged pions will decay into muons

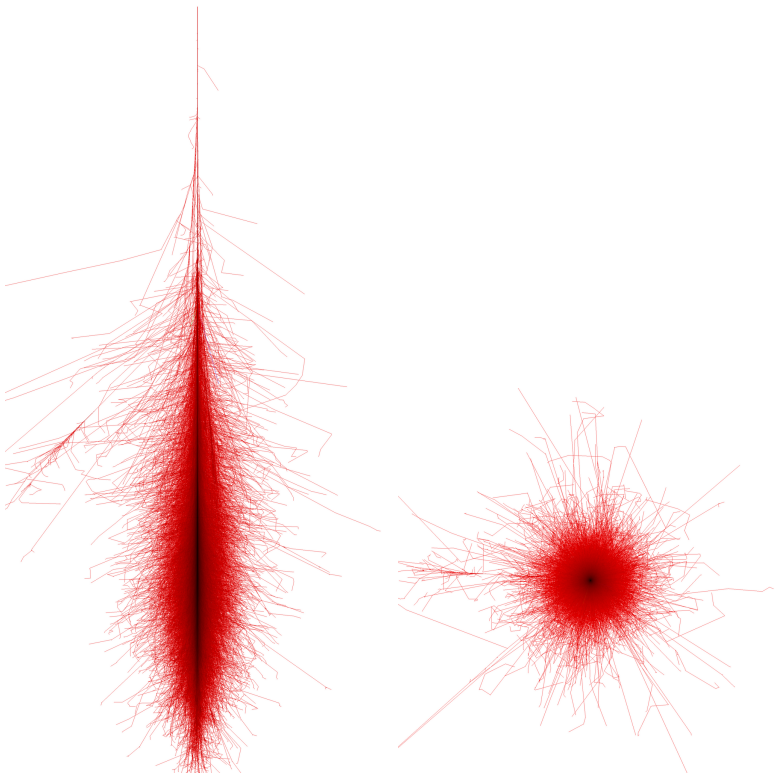

Figure 2.2 This is a particle track image of a CORSIKA simulated air shower from a gamma-ray primary of energy 1 TeV. The columnar projection (left) shows the shower's propagation through the atmosphere, while the shower's particle "pool" can be seen from the perspective of the ground (right). The track colors indicate different daughter particles; red = electron, positron or photon, green = muon, blue = hadron. Taken from http://www-ik.fzk.de/corsika/

and neutrinos. Some fraction of the muons will reach ground level due to Lorentz contraction before decaying.

2.4 Detection of Čerenkov Air Showers

For the bulk of the shower, we assume $\beta \sim 1$. This will not hold at the shower edges and during the shower's decline, but is a reasonable assumption since the shower particles have all been generated from either a primary or secondary with $E \gg mc^2$. It is established in 2.2 that the individual particles will emit their light within a cone of opening angle $\sim 0.8\,\mathrm{deg}$ at an altitude of $\sim 10\mathrm{km}$. At these energies,

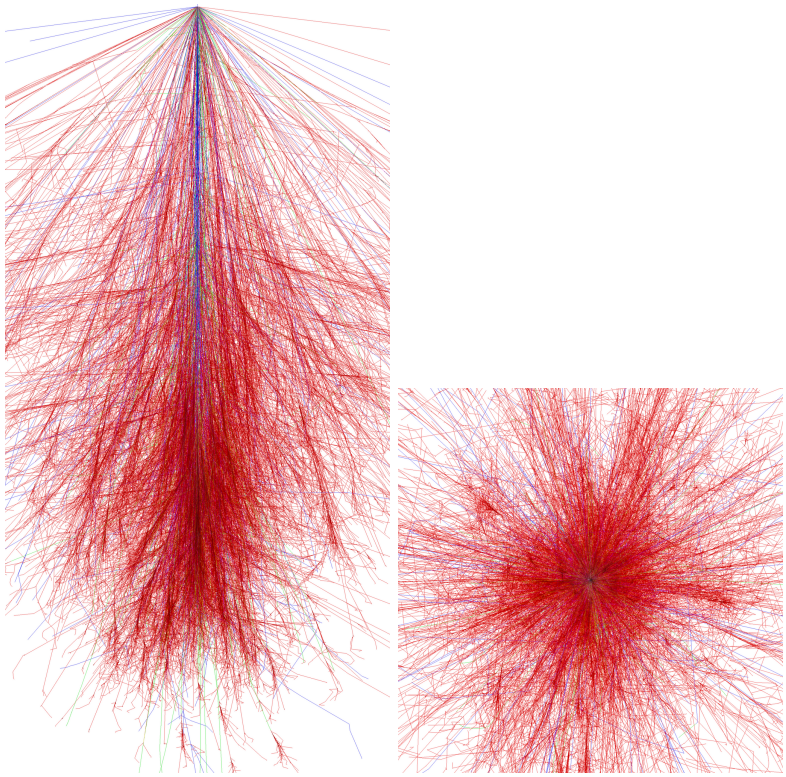

Figure 2.3 This is a particle track image of a CORSIKA simulated air shower from an ^{56}Fe primary of energy 1 TeV. The columnar projection (left) shows the shower's propagation through the atmosphere, while the shower's particle "pool" can be seen from the perspective of the ground (right). The track colors indicate different daughter particles; red = electron, positron or photon, green = muon, blue = hadron. Taken from http://www-ik.fzk.de/corsika/

the particles are beamed even more tightly than this, so the shower itself will radiate at approximately this opening angle. The bulk of the light will be emitted near the shower maximum h_{max}. For a typical value of h_{max} = 10 km, our light pool at ground level has a radius of $\sim$ 140 m. From Equation 2.5, the number of photons emitted over path length l is

$$N = 2\pi\alpha l \sin^2\theta \left(\frac{1}{\lambda_1} - \frac{1}{\lambda_2}\right) \tag{2.7}$$

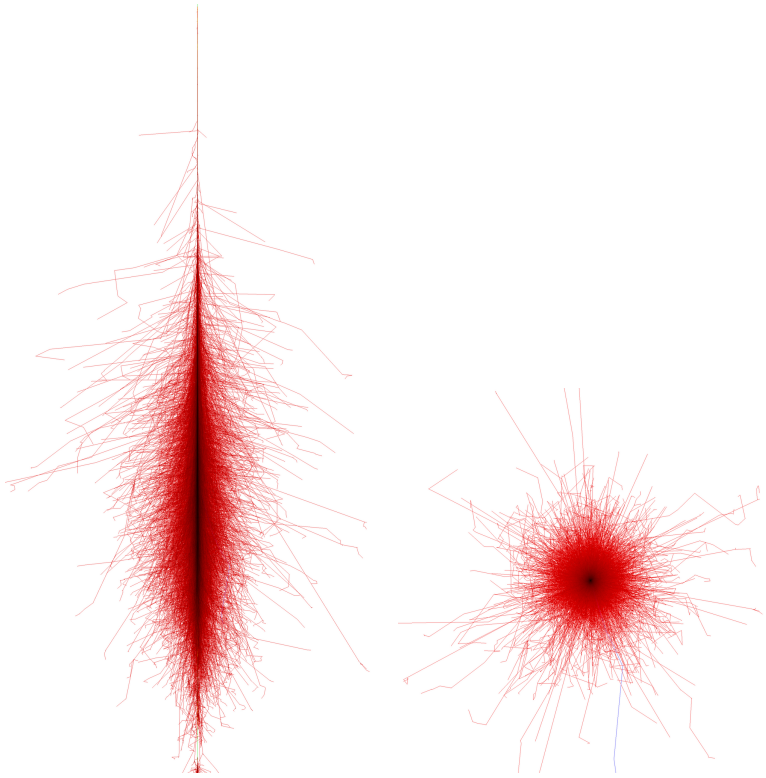

Figure 2.4 This is a particle track image of a CORSIKA simulated air shower from a muon of primary of energy 1 PeV. The columnar projection (left) shows the shower's propagation through the atmosphere, while the shower's particle "pool" can be seen from the perspective of the ground (right). The track colors indicate different daughter particles; red = electron, positron or photon, green = muon, blue = hadron. Taken from http://www-ik.fzk.de/corsika/

where $\alpha \sim 1/137$ is the fine structure constant. For a typical radiation length of $l = 930m$ have $N \sim 2.8 \times 10^4$ photons for 200 nm $< \lambda <$ 600 nm. For ~ 1000 particles in a shower, the light pool photon density is $\sim 500\,\gamma$ m^{-2}. This is a fairly crude approximation and omits absorptive and scattering processes which will further attenuate the photon signal. More rigorous predictions of air shower propagation and resulting photon densities are carried out via Monte Carlo simulations (see Table 2.1 for some representative values).

E_γ	h_{max} (km)	N_{max}	N_{sl}	N_{mt}	ρ_{sl} (γ m^{-2})	$\rho_{mt}(\gamma m^{-2})$
10 GeV	12.8	16	4×10^{-4}	0.02	0.27	0.36
100 GeV	10.3	130	0.04	1.4	4.6	7.6
1 TeV	8.4	1100	3	60	74	130
10 TeV	6.8	1×10^4	130	1.7×10^3	1.1×10^4	1.7×10^3
100 TeV	5.5	9.3×10^4	4.5×10^3	3.6×10^4	1.6×10^4	1.9×10^4
1 PeV	4.4	8.6×10^5	1.15×10^5	5.7×10^5	1.9×10^5	1.9×10^5

Table 2.1 A summary of representative values for gamma-ray induced showers for a range of primary energies E_γ. N is the number of particles and ρ is the photon density. Values are given for sea level and at mountain altitude ($\sim$ 2 km). Values taken from Weekes (2003).

2.5 Čerenkov Telescopes

In a more conventional optical telescope, a signal consisting of a few hundred photons would be swamped by the night sky background (NSB) of $\sim 10^{12}$ photons m^{-2}s^{-1}sr^{-1}. Thus, detection of the Čerenkov flash associated with air showers only becomes possible given an extremely short integration time, on order of 10 ns. This narrow integration window, when well matched to the duration of the shower, can sufficiently reduce the signal-to-noise ratio to allow for detection of this flash.

For an integration time over the full length of the flash, the total signal recorded by a camera is

$$S = \int_{\lambda_1}^{\lambda^2} F_C(\lambda)\eta_q(\lambda)Ad\lambda \tag{2.8}$$

where A is the mirror collection area, η_q is the quantum efficiency of the detector elements and F_C is the flux of Čerenkov photons detectable by the camera,

$$F_C(\lambda) = kE(\lambda)T(\lambda) \tag{2.9}$$

where $E(\lambda)$ is the Čerenkov emission spectrum from the air shower, T(λ) is the atmospheric transmission and k is a constant dependent on shower and instrument

geometries and the shower particle density. The background noise generated by fluctuations in the night sky is given by

$$B = \int_{\lambda_1}^{\lambda^2} F_B(\lambda)\eta_q(\lambda)\tau A\Omega d\lambda \tag{2.10}$$

where $F_B(\lambda)$ is the emission spectrum of the NSB, τ is the integration time and Ω is the solid angle. Thus our signal-to-noise ratio is given by

$$\frac{S}{N} = S * B^{-0.5} = \int_{\lambda_1}^{\lambda^2} C(\lambda) \left[\frac{\eta_q A}{F_B(\lambda)\tau\Omega}\right]^{0.5} d\lambda \tag{2.11}$$

The minimum detectable flash is inversely proportional to S/N, thus the threshold primary gamma-ray energy is given by

$$E_{thresh} \propto \sqrt{\frac{B(\lambda)\Omega_\tau}{F_C^2(\lambda)\eta_q(\lambda)A}} \tag{2.12}$$

Note that S/N is inversely related to integration time, and that the energy threshold increases with $\tau^{0.5}$. Minimizing integration time is considered preferable, and VERITAS' method for doing so is discussed in 4.4

2.5.1 Imaging Atmospheric Detectors

PMT's are typically selected for their fast response and near-UV sensitivity. The major installations of the third generation of IACT are typified by arrays of large-area reflectors with fast electronics capable of handling the enormous quantity of data taken in by these telescopes with nanosecond resolution. These arrays include HESS in the Khomas Highlands of Namibia ([Bernlöhr et al. 2003], [Cornils et al. 2003]), MAGIC on the Canary Island of La Palma (Cortina et al. 2005), CANGAROO-III in Woomera, Australia, and VERITAS at Mt. Hopkins, AZ (see 2.6).

2.5.2 Particle Detectors

Milagro is a water Čerenkov air-shower detector located near Los Alamos, NM (Smith 2005), now no longer in operation. This system used a 6 million gallon

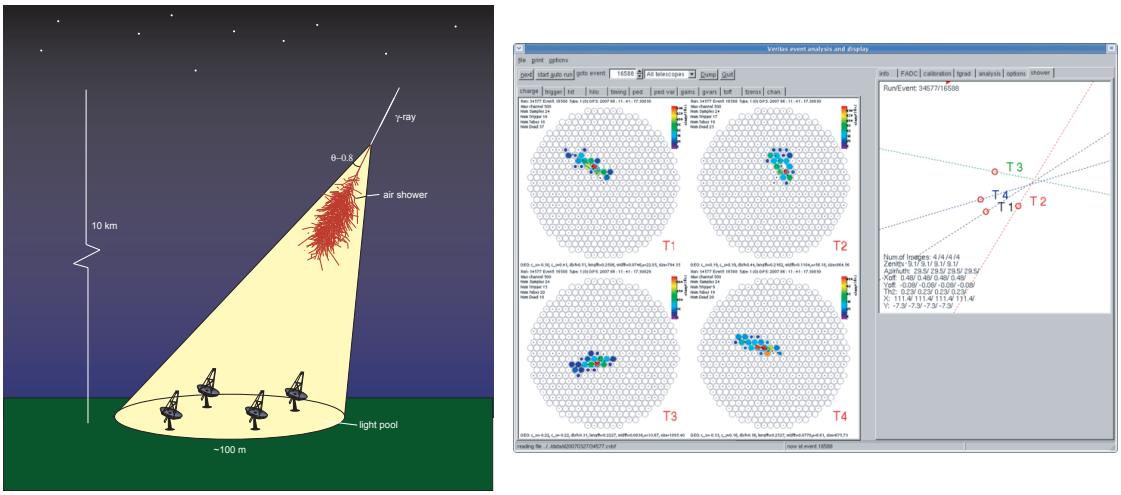

Figure 2.5 This is a schematic of an IACT array imaging and incident gamma-ray induced air shower. The intersection of the major axes of the properly rotated event images in each telescope are used to reconstruct the direction of the gamma-ray primary.

tank of water in much the way ACT telescopes use the Earth's atmosphere. A primary plane of PMTs is placed 4 radiation lengths deep in the water tank to detect Čerenkov light from relativistic particles entering the tank. Beneath this, another layer of PMTs is placed 16 radiation lengths deep; these are used to identify and select out cosmic rays which have a more penetrating component. The next generation of this technique, HAWC (Sinnis 2005), is currently under construction and consists of a 22000 m^2 instrumented area at 4100m on Volcan Sierra Negra in Mexico.

More conventional (but less successful) experiments at these energies have relied on arrays of particle detector spread over large areas, largely geared toward the detection of more penetrating ultra high energy gamma-ray showers. These include

the large scale array of scintillation detectors at high altitude in Tibet (Amenomori et al. 1992) and CASA-MIA at Dugway, Utah (Borione et al. 1993).

2.5.3 Solar Arrays

An interesting, if largely abandoned, idea was that of using large arrays of optical heliostats designed for solar collection as Čerenkov light collectors. This represents an extremely economic usage of existing facilities and the collection areas are typically very large. The resultant low energy threshold (30 - 100 GeV) simplifies the exclusion of hadronic showers (which are inefficient at producing Čerenkov light at these energies). However, the challenges in employing such a dual-purposed instrument are difficult to overcome. These arrays included STACEE at Sandia Labs in Albuquerque, NM [Bhattacharya et al. 1997], Solar Two in Barstow, CA (Zweerink 1999) and CELESTE in the Pyrenees in France [Smith et al. 1997].

2.6 VERITAS

The VERITAS array is located at the administrative center of the Fred Lawrence Whipple Observatory near the base of Mount Hopkins in southern Arizona. VERITAS is composed of 4 12-m IACT telescopes of the Davies-Cotton design. The following chapter describes the hardware comprising these telescopes, the systems used in acquiring the data, and the performance of the VERITAS system.

2.6.1 Telescopes

The Davies-Cotton reflector was originally designed as a collector for a solar furnace (Davies and Cotton 1957). The reflector consists of a series of small spherical mirrors set onto a spherical surface. The spherical reflector cannot simply be treated as a single huge spherical mirror, where the focal length is given by $F = C/2$, where C is the radius of curvature of the dish. Instead, the telescope has the focal length of the individual mirrors, that is

$$F = f = c/2 \tag{2.13}$$

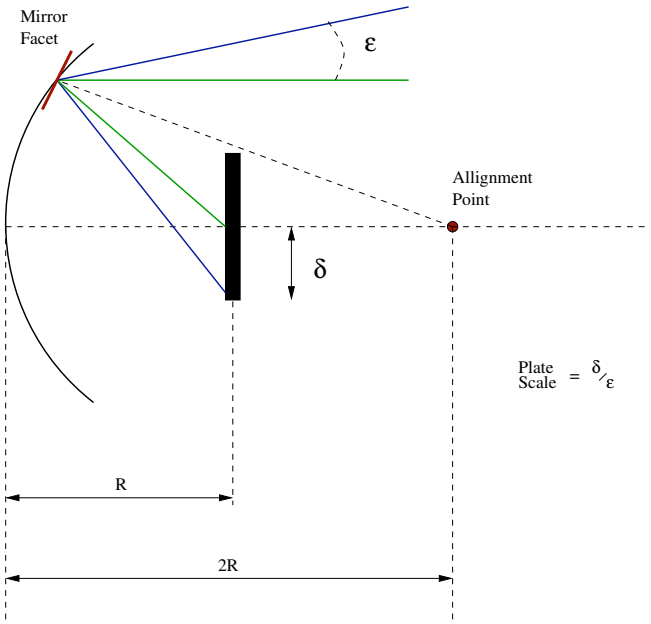

Figure 2.6 This is a schematic of the Davies-Cotton reflector with both the focal point (R) and the alignment point (2R) shown. Figure taken from Cogan (2006).

where c is the radius of curvature of the individual mirrors. The focal length F = 12m was chosen in part to achieve an f-number of f/1.0. The increased f/# (relative to the Whipple 10m's f/0.7) is intended to reduce aberration due to off-axis mirrors.

The key drawback of the Davies-Cotton design is that it anisochronous; that is, the arrival time at the focal point of a planar wavefront is not the same for light reflected from mirrors closer to the axis than for the light from the mirrors farther out. In VERITAS, this delay is roughly 4ns. Since VERITAS does not currently employ the shower evolution (which occurs over a roughly equivalent time scale) in characterizing the images, the only drawback of this anisochronicity is a decreased sensitivity to short pulses.

The 345 hexagonal mirrors are closely tessellated to cover the full dish, resulting in a total reflector area of $\sim 110m^2$. Side to side, each mirror measures 61

cm across and have a thickness of 11.5 mm. Each mirror is cleaned and coated locally to a thickness of $\sim 1350\mathring{A}$ with evaporated aluminum. The coating is anodized in place. The reflectivity exceeds the design specifications of $\geq 85\%$ between 280 - 450 nm, and $> 90\%$ at 320 nm (Roache et al. 2008). The reflectivity is geared to be highest in the UV, where most of the Čerenkov light is found. Reflectivity is maintained by a rotating schedule of cleaning and recoating of the facets.

The Optical Support Structure (OSS) is a custom-built steel frame of D $\sim$ 12m . Facets are mounted on a triangular mounting structure which isolates the mirror from any flexing in the OSS and allows for independent mirror alignment via adjustments of the 3 mirror mounting screws. For more details on alignment of the mirrors, see Appendix B.

The OSS is supported and moved by an altitude-over-azimuth positioner. The mount is capable of a slew speed of $1^{\circ}s^{-1}$. Tracking software, custom designed for the VERITAS telescope, tracks with errors $< 0.01^{\circ}$ (Holder et al. 2006).

2.6.2 Cameras

Each VERITAS camera is contained in an enclosure, hereafter the "focus box", held at the focal point by quadrapod arms extending from the OSS. The focus box has a remote-controlled shutter to protect the camera face when not observing. In addition to the photomultiplier tube (PMT) camera, each focus box houses the signal pre-amplifiers, the current monitor boards, charge injection boards, environmental sensors and focusing light cones.

PMTs are the most readily available detectors for the extremely fast, faint Čerenkov flashes associated with air showers. Within a PMT, an incident photon strikes the metal photocathode and an electron is released via the photoelectric effect. This photoelectron is accelerated toward a series of of dynodes held at sequentially increasing potential. Each dynode is covered with an emissive material which releases more electrons when struck by the primary photoelectron. The resultant cascade of electrons eventually collect at the anode, which registers a current.

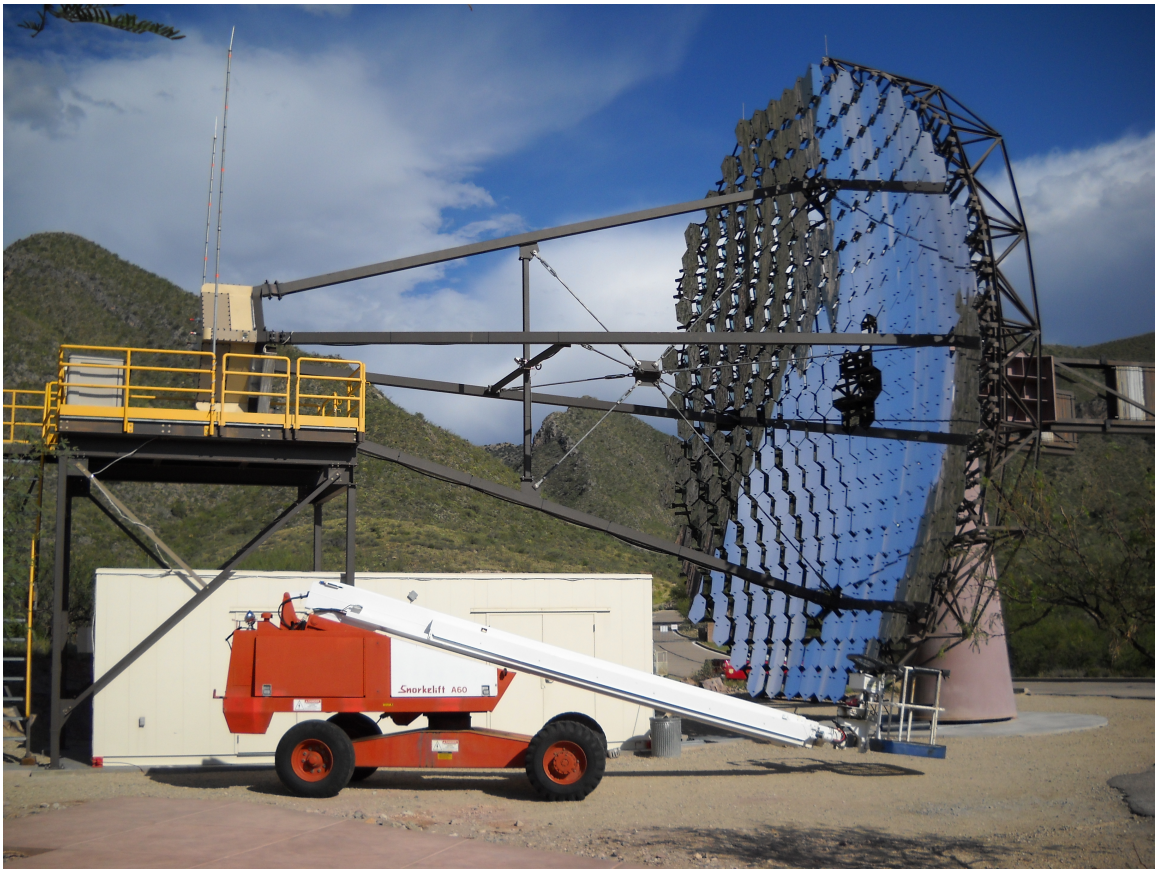

Figure 2.7 This is an image of the newly relocated Telescope 1. The four telescopes of VERITAS are essentially identical in construction.

The average number of electrons produced by a primary photoelectron at the final dynode is the *gain* of the PMT, and depends on the number of dynodes and the applied potential. The VERITAS cameras consists of an array of 499 Photonis XP2970/02 10-stage PMTs. Each tube is 29 mm in diameter, has a QE of 0.25 at 320 nm and provide a gain factor of $\sim 2 \times 10^5$ at V = 850 V.

Due to the width of the PMT bases, glass windows of the PMTs are not perfectly tesselated, resulting in space between the PMTs to which light would be lost. To compensate for this, a hexagonal grid of Winston light cones is placed over

Figure 2.8 This is the VERITAS array layout as of the taking of data used in this work. T1 has since been relocated to give the array a more symmetric layout.

the camera to channel light into the PMT. These light cones are aluminum with a SiO_2 coating to improve reflectivity above 350 nm.

At the base of each PMT, a low-noise preamplifier board is included to boost the signal by a factor of 6.6. This minimizes the impact of any noise generated in the 45m of coaxial cable between each PMT and the FADCs (see 2.6.4), and to trigger on the low signal produced by a few photoelectrons. The preamps are also fitted with an output so that the anode current can be monitored by the current monitor system. The current monitor prevents permanent damage to the PMTs caused by exceedingly high anode current. To improve the PMT lifetimes, the current monitor signals the observer and high voltage (HV) program when the current on a PMT exceeds a preset kill limit. The HV program will then automatically switch off the HV in order to stop the charge being deposited on the anode, thus extending its lifetime. The typical example of this is when a bright star is in the field of view of an observation, causing excessive current in a few pixels.

The current monitor system also includes power and readout channels for the humidity and temperature sensors within the focus box. Monitoring the temperature is important, as PMT gain decreases with increase in temperature by roughly 1%/C°. An exhaust fan is used to cool the focus box in the evenings before operations commence. Humidity monitoring is also important, as the resulting increase in the conductivity of the air can allow for electrical discharge between the PMTs.

2.6.3 Triggers

Before any discrimination between shower types can occur, the overall Čerenkov signal must be filtered from the ambient fluctuations in the NSB. This discrimination is done live during observations in order to maintain a data rate which the data acquisition system can handle.

Triggering occurs on three separate levels, referred to as L1, L2 and L3. The first two of these triggers occur at the individual telescopes and can discriminate between extensive air showers and non-shower NSB fluctuations, while the third takes place on an array level.

L1: Pixel Threshold Trigger

The PMT signal is split between a Flash Analog to Digital Converter (FADC) and a Charge Fraction Discriminator (CFD). At the FADC, the signal is stored short-term to await a "pass/fail" from the trigger system. The CFD will check the signal against a set threshold; if the threshold is exceeded then the L1 is triggered. To determine the correct trigger time, the PMT signal is again split, this time into 3 signals, before arriving at the CFD. The first signal is checked against the threshold. The second signal is inverted and delayed, while the third is attenuated. The second and third signal are fed into a Zero Crossing Discriminator (ZCD). The ZCD determines the time at which the signals cancel, and this becomes the trigger time.

Minor fluctuations due to NSB introduce a jitter in the timing resolution due to resultant offsets in the zero-crossing time. A small offset in the current to the CFDs would reduce such a jitter, but would also raise the threshold for detection. Instead, this jitter is compensated for with a Rate Feedback Loop (RFB

Loop) (Kieda et al. 2003). The RFB loop adds a DC offset to the zero-point crossing calculation proportional to the ZCD trigger rate. Effectively, as the PMT is exposed to more random fluctuations, the CFD compensates by offsetting the signal to the ZCD. This implementation results in a $\sim 10\%$ reduction in the timing jitter.

L2: Pattern Selection Trigger

The second trigger level, L2, is the Pattern Selection Trigger (PST). Upon triggering, the CFD passes the pixel signal to the PST. This level triggers on groups of adjacent pixels triggered at the CFD within a certain time window. To facilitate this, the camera is divided into 61 overlapping sections of 19 adjacent pixels by means of a signal splitter (Bradbury 1999). Each patch is searched for a set number of adjacent pixels (typically 3) firing within a set coincidence window (typically 6 ns). Having a narrow coincidence window eliminates a large number of false triggers, and contributes to the reduction of the energy threshold. Typical L2 rates are on order 1 kHz at each telescopes.

L3: Array Trigger

At the single telescope trigger level, no discrimination between shower types occurs. While shape parameterization will allow for discrimination during analysis, muon-induced showers with large impact parameters will appear gamma-like at the single image level. The Level 3 array trigger eliminates these by requiring a trigger on multiple telescopes in the array. Single muon events are highly localized and will generally not trigger multiple telescopes. Since muons dominate the low energy background of the Čerenkov light, a reduction in muon triggers lowers the energy threshold of the array.

The VERITAS L3 is triggered when a set number of telescopes trigger within a specified coincidence window which can be set from 10 - 250 ns. The array trigger is capable of handling a data rate up to 1 kHz with a 10% deadtime (with a decision time of 1 μs). Further, the array trigger system sets event numbers and masks, and records rate, timing and diagnostic information. The array trigger is also capable of running on a subset (or multiple subsets) of telescopes. This is regularly implemented for a subset of the array (as in the case of one or more telescopes being

down for maintenance), but the author is not aware of any instance of VERITAS running in multiple subarrays simultaneously.

If the shower passes the L3 trigger criteria, a signal is sent to each telescope and the shower data is read out from each FADC buffer.

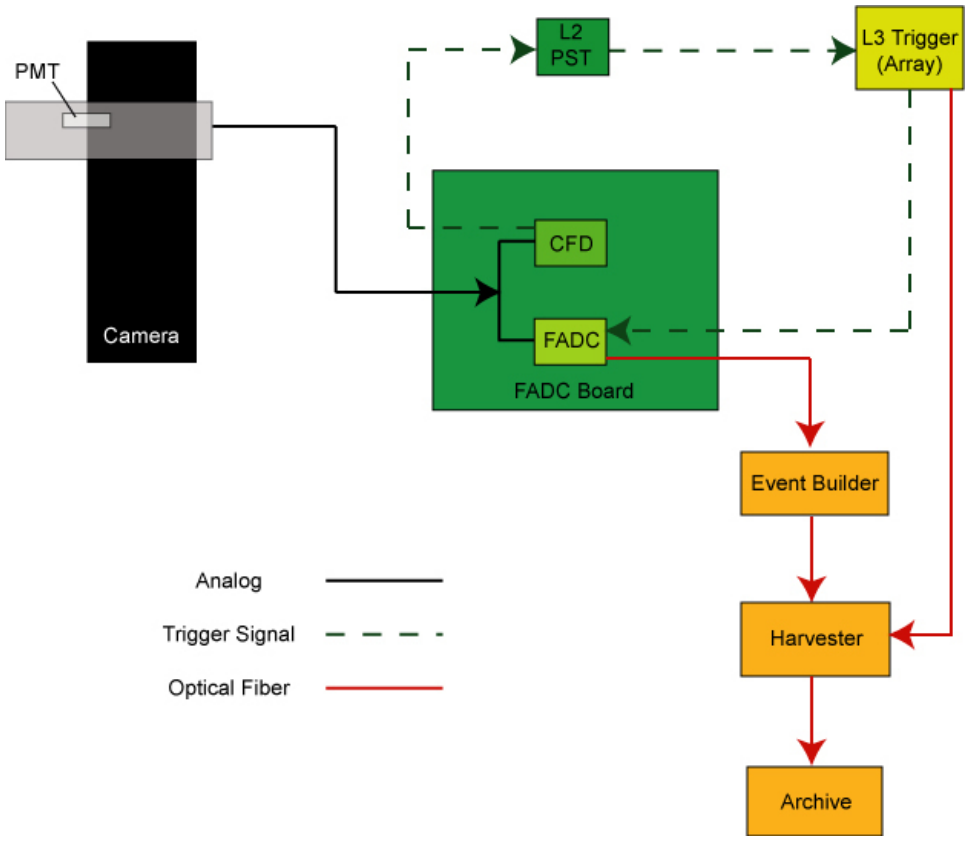

Figure 2.9 This is a schematic of the VERITAS Trigger System. .

2.6.4 Data Acquisition

FADC

As mentioned before, the first stage of the VERITAS data acquisition is carried out by the 50 custom FADC boards with 10 pixels per board. The FADC boards are capable of measuring the voltage on a timescale of 2 ns. This temporal

resolution is important in minimizing the integration window for each event to lower the S/N. With such fine resolution, it is also possible that the timing information could be used for an enhanced FADC trace, allowing for characterization of showers by their temporal development, though no such characterization is currently employed. The profile of events as handled by the FADC is further discussed in 4.4, and the L1 trigger handled by the FADC's is discussed in 2.6.3.

event builder

Upon readout, the shower data is transferred to the *event builder* computer. The event builder assembles the event information from the 4 VME crates, plus the time stamp information from the auxiliary crate, into a telescope event file. The event builder also carries out basic quality control on events by handling incomplete events. This telescope event file is written to disk and then passed on to the next stage.

harvester

The telescope event files are sent to the *harvester* computer. The harvester assembles the telescope files into a single array file. This file is of the custom VERITAS Bank Format (VBF), which serves as the starting point of the Offline Analysis. The file is also compressed to $\sim$ a few GB per run, with one file per run. This is significantly more manageable than the $\sim$ 1 TB which would result from a comparable system with no trigger discrimination. It is worth noting that, at this point, the separate telescope events are already matched, thus eliminating any need to match them in the Offline Analysis.

database

At the same time as the events are being assembled, the *database* is continuously recording the observation conditions and settings, such as the CFD settings, L2 triggering patterns, high voltage levels, the look-back times (i.e., signal delays), etc. The database also records any changes in settings by observers and acquisition information for a given run including run types, source names or positions, selected trigger types and diagnostic information such as weather, PMT currents telescope

tracking and any comments logged by the observer. The database is later queried for relevant details by the Offline Analysis (see 4.5).

2.6.5 Performance

T1 has been in operation since Fall of 2003, and VERITAS has taken data as a full 4-telescope array since Spring of 2007. In this time, the performance and sensitivity of the array has been extensively measured and monitored. Here we present values for the sensitivity to gamma-ray events, energy and angular reconstruction (Holder et al. 2008). Note that all values are dependent on both telescope parameters and the applied analysis.

Angular Resolution

The angular resolution of VERITAS is dependent on both the absolute pointing of the telescopes in the array and the analysis procedure. The dependence on analysis is largely due to the uncertainty in the reconstruction of the position of the event on the sky. Telescope pointing calibration is done ~ 1/month by imaging bright stars of well-known position in the telescope's Optical Pointing Monitor cameras. The offset is measured and applied as a correction to the telescope positioning at various values of altitude and azimuth. This compensates for minor inaccuracies in the positioning system and flexing of the OSS during tracking. The resultant pointing accuracy is $\sim 0.02\,\mathrm{deg}$.

In offline analysis, the best angular resolution is obtained by requiring strict cuts on the allowed gamma-ray events. Figure 2.11 gives the angular resolution for a dataset requiring a 4 telescope trigger and a relatively large size cut of >75 photoelectrons. Over the full energy range, the averaged single event angular resolution is $\sim 0.1^{\circ}$, where the resolution is defined as containing the event out to a 68% likelihood.

Sensitivity

VERITAS is currently the most sensitive of the major IACT arrays. For a steady VHE source smaller than the angular resolution, VERITAS is able to detect a flux of 1% of the Crab Nebula in 47 hours of observation and a flux of 5% of the

Crab Nebula in only 2.5 hours. Note that this sensitivity depends strongly on the source's position on the 2.5° field of view, tending to fall below usable levels outside 2° or so. Figure 2.10 shows gives both the sensitivity of the array with time and radially across the FoV.

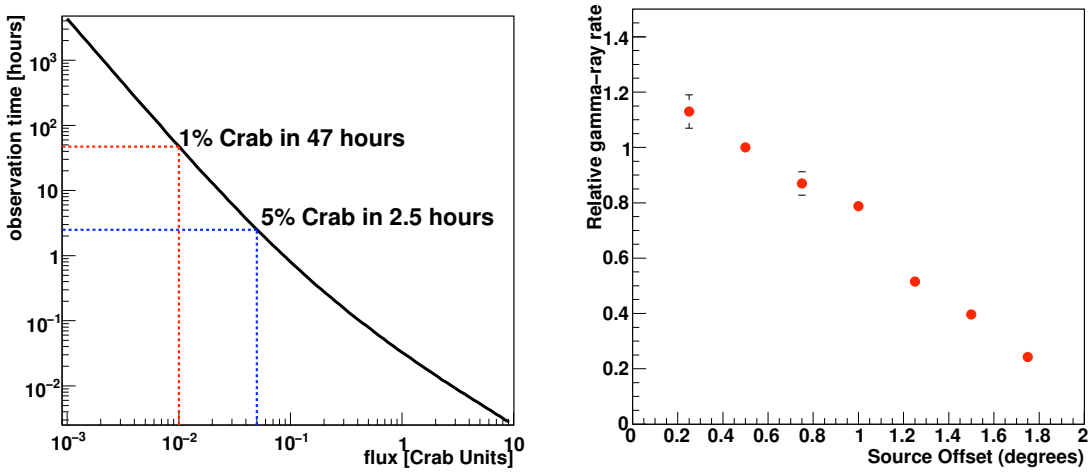

Figure 2.10 This is the time needed for a 5σ detection versus source rate (left) and the normalized photon rate with respect to source position in the FoV (right). Taken from Holder et al. (2008)

Energy Resolution

The energy of incident gamma rays is calculated based on the parameterized values of the Čerenkov images using lookup tables filled from simulated gamma-ray events, as discussed in 4.7.4. Spectral reconstruction, given a sufficient source flux, is possible above 150 MeV with an energy resolution of $\Delta E/E \sim 0.15$

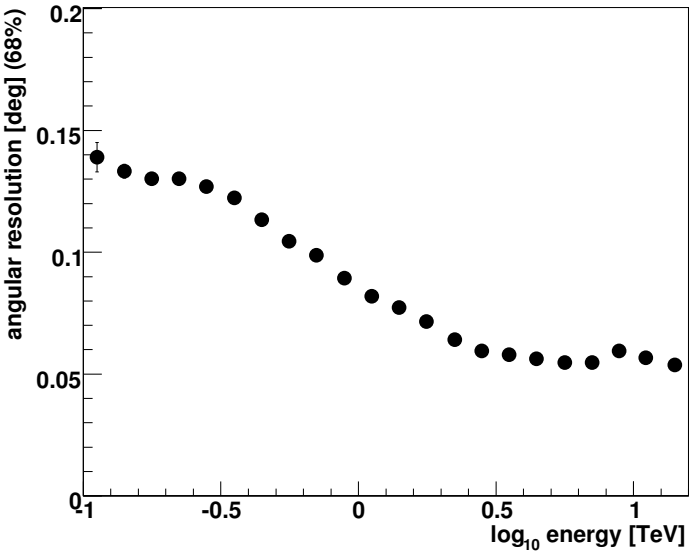

Figure 2.11 This is the angular resolution for VERITAS at a given energy. Taken from Holder et al. (2008)

CHAPTER 3

CYGNUS REGION SKY SURVEY

The Cygnus Region is a complex region which spans the sky between $52^\circ < l < 82^\circ$ along the Galactic plane. The region is populated with a number of molecular clouds and is one of the richest known star forming regions within our Galaxy (Dobashi et al. 1996), and spans much of the nearby Cygnus Arm of the Galaxy.

Three unresolved EGRET sources lie within the region (Casandjian and Grenier 2008), as does the TeV source J2032+413 (Aharonian et al. 2005). Most recently, Milagro observations of the region have revealed a TeV excess beyond that expected based on either Galactic cosmic ray models or EGRET limits on the region (Abdo 2007). This diffuse emission may be caused by the normal galactic cosmic ray density interacting with the enhanced density of hydrogen in the region (Bi et al. 2009).

The Cygnus Sky Survey was a VERITAS Key Science Project for the first 2 years of 4-telescope operation. The Survey was intended to be completed in two parts, Y1 covering the region $67^\circ < l < 82^\circ$, the second $52^\circ < l < 67^\circ$, with both spanning the Galactic Plane $-1^\circ < b < 4^\circ$. This RA band poses particular difficulties for observation. First of all, it is crowded with sources of potential interest, include sources outside the survey band that provide competition for limited observing time. Secondly, the Cygnus region first becomes observable at the end of the monsoon period in southern Arizona. During the monsoon, operations at VERITAS shut down entirely due to cloud cover, rain, and potential lightning strikes. The Fall start of observing is entirely dependent on the end of the monsoon season, and thus a longer monsoon reduces the available time for Sky Survey observations. Due to these observational constraints, only Y1 has been completed to date. Figure 3.1 shows the completed observations in the framework of the original observational scheme, which was planned to optimize observation time while producing an even

exposure across the surveyed region. Follow-up observations on "Hot Spot" areas have given a somewhat less even exposure over the survey region.

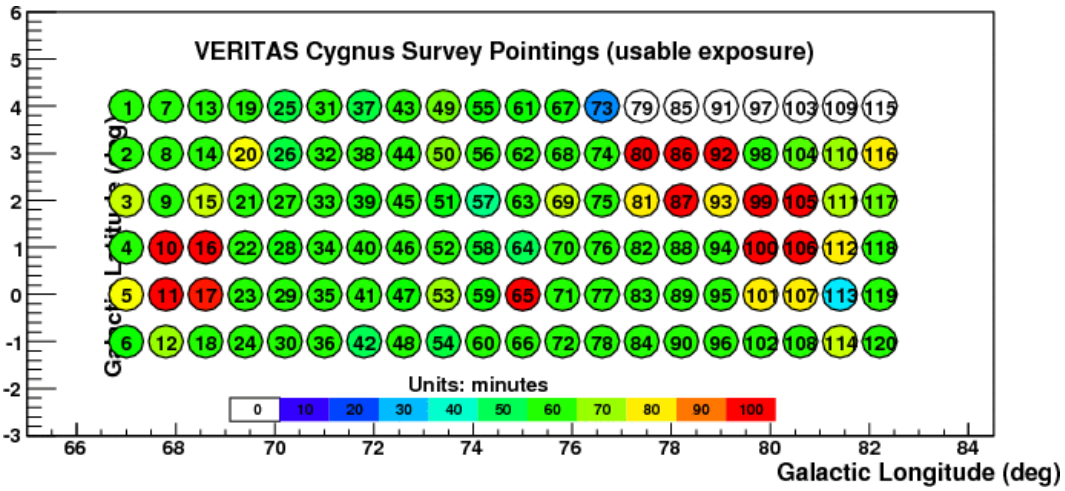

Figure 3.1 This figure shows the total usable exposure of the Cygnus Sky Survey. Plot taken from http://veritasm.sao.arizona.edu/DQM/cgi-bin/skysurvey/survey_tools

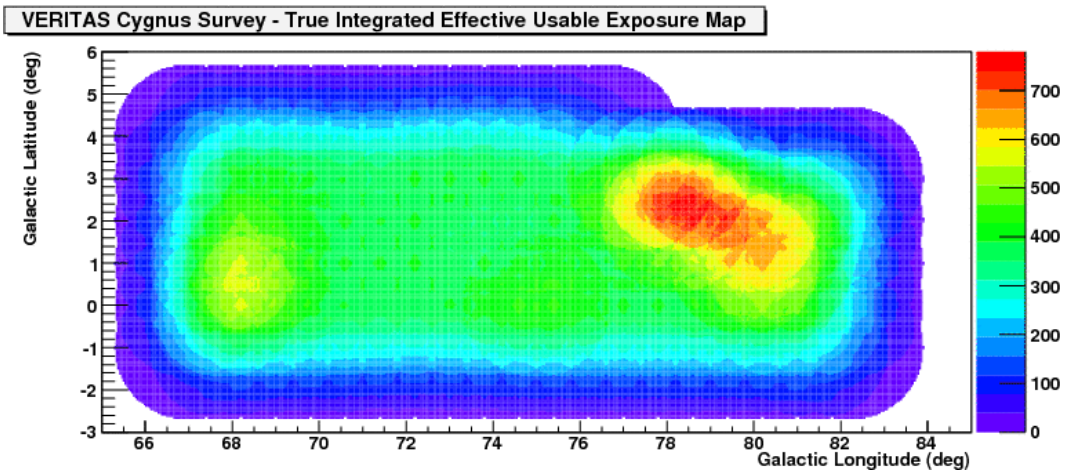

Figure 3.2 This figure shows the true integrated exposure of the Cygnus Sky Survey. Plot taken from http://veritasm.sao.arizona.edu/DQM/cgi-bin/skysurvey/survey_tools

CHAPTER 4

ANALYSIS

The earlier chapter covered the means by which VERITAS collects gamma-ray events. The extraction of astrophysical data from this information is an involved process. A basic description of the data is given in 4.1. Selection of data to ensure quality is covered in 4.2. The settings used in event triggering are outlined in 4.3 The data is processed through basic calibration (4.5) and parameterized on the single telescope (4.6) and stereo level (4.7). Finally, the analysis as carried out in the multi-stage VEGAS software package is discussed in 4.8.

4.1 Data

For the purposes of this work, data analysis begins with the VBF files for each individual 20 minute run. For a more in-depth discussion of the data acquisition and storage, see 2.6.4.

There are two distinct data types presented in this work: pointed observations of individual SNRs, and those taken as part of the two-year Cygnus Region Sky Survey. All data have been taken with the VERITAS array in either 3- or 4-telescope mode.

Pointed observations were all taken in "Wobble" mode, wherein data is taken with a constant offset (typically 0.5°) from the target. This allows for the simultaneous collection of both On and Off data at the same radial position on the camera. As the acceptance of the telescope varies approximately radially over the field of view, this avoids the necessity of using an acceptance correction when determining excess counts or detection significance at the source position.

Data for the Sky Survey were taken as direct, evenly spaced pointings hereafter referred to as "survey mode." There are potential advantages and disadvantages to this method. Survey mode, when taken evenly, creates a larger continuous area of smooth coverage. Variations in sensitivity over the survey dataset are thus

minimized. The primary disadvantage to this method is the investment of observation time relative to the achieved exposure at any given point; put simply, spreading observations over a larger region reduces the time spent observing any specific point.

A full list of runs included in this work with observational details can be found in Appendix A.

4.2 Quality Selection

Specifying the selection of useful data . Of primary importance is consistency in the data-taking configuration and conditions, especially given the continuing evolution of VERITAS as a scientific instrument.

4.2.1 Observing Conditions

Weather conditions are by far the most difficult variable to account for, both due to lack of control on the part of the observers, as well as difficulty in consistently gauging the quality of the observing conditions from night to night. Observing conditions are ranked on two separate scales, both ranging from A weather (near optimum observing) down to F (completely untenable). The first scale is the assessment of overall conditions by the observers. While this method is somewhat subjective, relying as it does on observer fiat, the ready availability of local atmospheric data and direct on-site assessment of sky coverage allows for a reliable assessment of current conditions.

The second measure is based on the infrared radiometers mounted on T1, T3 and outside the control trailer. These devices image the infrared emission from the atmosphere. In the case of the T1 and T3 units, this is along the line of sight of the telescope, while the control trailer unit is directed at zenith. Variation in the temperature of the radiation along the line of sight is a good indication of variations in the airmass; low-altitude cloud cover return considerably warmer signals than clear skies.

Data runs are passed with minimal inspection given an A or B ranking by both the observers and the automated FIR system. The rates on any run given a

C ranking by either method were inspected before giving a pass or fail for analysis; anything marked below C by either method was excluded.

4.3 Trigger Settings

To eliminate events caused by fluctuations in the night sky background, VERITAS employs a series of hardware triggers that must be passed by any event before being recorded.

CFD Trigger (L1): The Level 1 trigger discriminates by only triggering on events which exceed a set voltage in the CFD. All the data in this work were taken with the standard dark-sky threshold of 50 mV for all telescopes.

Pattern Trigger (L2): The Level 2 trigger is based on the number of adjacent CFDs which trigger within a set coincidence window. All the data in this work were taken with an L2 3-fold multiplicity trigger.

Array Trigger (L3): The Level 3 trigger is based on the number of telescopes in which an event is triggered within a set time interval. This trigger level primarily eliminates muon events, which typically only trigger a single telescope. The 3-telescope data in this work uses a 2/3 array trigger. The 4-telescope data uses a 2/4 array trigger.

4.4 FADC trace

Each photon striking the PMT is converted into a number of electrons. This produces a pulse, the total charge of which is proportional to the number of photons incident on the PMT photocathode. This pulse is digitized by the FADC for each channel as a series of amplitude values in digital counts (dc) for each 2 nanosecond (ns) bins. The voltage profile of a light pulse as registered by the FADCs is referred to as the *FADC trace*. The total charge stored in the FADC trace (in digital counts) for each event is proportional to the total number of photo-electrons detected. In addition to charge information, the recorded FADC trace also contains the arrival time of the signal at each pixel.

A typical Čerenkov pulse has a duration of 8-10 ns, including optical and electronic delays. VERITAS data are recorded in a 24-sample FADC trace. This 48 ns window, then, covers a large period during which night-sky background (NSB) is the only source of photoelectrons. In order to minimize the contribution from the NSB, a "signal window" is established to bracket the Čerenkov pulse as closely as possible. To this end, only pulses with a charge greater than a set threshold are recorded. VEGAS uses a user-defined integration window, and the integration windows are set to start 4 ns (2 samples) before start time of each pulse. For the Targeted Remnant datasets, a standard 7 sample integration window width was used. For the Cygnus Region Sky Survey dataset, a longer 12 sample width was used as part of the Sky Survey optimization.

For timing purposes, an event's start time in a given channel is defined as the point at which the pulse achieves half of its peak value. This is evaluated after the subtraction of the pedestal baseline.

Determination of the integrated charge for the FADC trace is simply calculated by adding up the signal amplitude values from each sample in the integration window.

4.5 Calibration

Before any reconstruction or selection of gamma rays can occur, calibration of the collected data must be carried out. Within VEGAS, these calibration constants are generally calculated in Stage 1 and applied in Stage 2 (see 4.8).

4.5.1 Pedestals

The individual PMT output is an AC coupled signal. However, signal digitalization is limited such that any positive voltage fluctuation due to the NSB cannot be digitized. To compensate, a signal corresponding to roughly 16 digital counts is injected into the AC coupled output. In order to measure these fluctuations, artificially triggered events or *pedestal events* are created. Each pedestal event essentially samples the NSB in each channel. The FADC charge is then integrated

per "pedestal event" as normal to generate pedestal statistics over the course of the observation. The pedestal event rate for VERITAS is between 1-3 Hz, yielding good statistics while minimizing dead time for the collection of true events. In addition, the standard deviation of the pedestals for each channel (the *pedvar*) are calculated and compared to median pedvar over all channels. Any pixel with a pedvar above a set threshhold is excluded from analysis of Čerenkov events as noisy.

Corrections based on the pedestal statistics are calculated in VEGAS in Stage 1 and applied in Stage 2, concurrent with the gain corrections.

4.5.2 Timing Offsets

Due to electronic delays within the instrument, the arrival time of individual channels associated with the same event will be different. This relative timing between channels is given by the calculation of T_{Offset}

$$(T_{Offset})_i = \frac{1}{M} \sum_{event=1}^{M} (\Delta t_i)_{event} \tag{4.1}$$

where

$$\Delta t_i = (T_0)_i - T_{event} \tag{4.2}$$

$(\mathrm{T}_0)_i$ is the arrival time at pixel i and T_{event} is the average arrival time of the signal over all the pixels.

The individual channel values are calculated by measuring the delay in laser flashes illuminating the camera pixels. These flashes are recorded during a "laser run" taken once per night and analyzed in Stages 1 and 2 of VEGAS.

4.5.3 Gain Calibration

In an ideal scenario, the charge recorded at the FADC channel level is proportional to the number of Čerenkov photons incident on that pixel; thus the sum of the charges for a particular channel yields a total charge proportional to the amount of incident light. In reality, variations in the high voltage due to unavoidable environmental and electronic variables causes there to be a different response for every

given pixel. This difference is measured and corrected in a similar way to the timing corrections.

The average charge deposited on a single channel during an event is calculated as

$$\langle Q_{event} \rangle = \frac{1}{N} \sum_{i=1}^{i=N} Q_{i,event} \tag{4.3}$$

The relative charge per channel is the given by:

$$(R_{Qi})_{event} = \frac{Q_{i,event}}{\langle Q_{event} \rangle} \tag{4.4}$$

For a large number of laser events, the Relative gain is then calculated for each channel

$$\text{Relative Gain}_i = \frac{1}{M} \sum_{event=1}^{M} (R_{Qi})_{event} \tag{4.5}$$

This is then applied to the data on a channel-by-channel basis. Relative Gain values close to one are clearly preferable, and adjustments are made to the voltages annually to minimize the differences in the responses of each pixel.

4.5.4 Other Calibration

During data calibration, checks on pixel status are also carried out. Pixel status is evaluated in two ways. First, bad or deactivated pixels are logged as such by the HV system to the Database, and this information is retrieved and applied during calibration. Secondly, the pixel pedvar is evaluated as a check on the pixels status. An inactive pixel will return a pedvar close to zero, while a "noisy" pixel will return a particularly high pedvar. To evaluate this we calculate the Scaled Pedvar

$$\frac{pedvar - \langle pedvar \rangle}{\sigma_{pedvar}} \tag{4.6}$$

VEGAS requires a safe range of -1.5 $<$ S.P.$<$ 4.0

Similarly, a scaled relative gain is calculated to exclude any channel with a significantly different response from the rest of the camera. For the scaled relative gain, VEGAS uses a safe range of -3 < S.R.G. < 3.

4.6 Single Telescope Parameterization

Once the data has been calibrated, the Čerenkov showers must now be identified and parameterized according to their geometries. The cleaning process identifies those active pixels belonging to potentially reconstructable events. Once cleaned, these images are parameterized according to the process developed by [Hillas 1985].

4.6.1 Image Cleaning

At the camera level, the image cleaning requires two steps. In the first, image pixels are identified. "Picture Pixels" are identified as those pixels which, for a given event, have an integrated charge in excess of five (5) times greater than that channel's pedvar. Any pixel adjacent to a Picture Pixel with an integrated charge greater than 2.5 times greater than its pedvar is labelled as a "Boundary Pixel." In the second step, all isolated pixels not neighboring either a Boundary or Picture Pixel are removed. The remaining pixels then define the image of the Čerenkov shower.

4.6.2 Parameterization

Given the geometric distinction between Čerenkov images of gamma rays and cosmic rays, it is not surprising that parameterization of these images is seen as a direct means of discriminating between them. Some of the most successful parameterization schemes are variations on the developments in [Hillas 1985]. In this arrangement, the camera coordinates (x,y) of the image pixels are codified according to their *Distance*, *Width*, *Length*, *Miss*, *Azwidth*, *Asymmetry*, *Alpha*, *Size*, *Frac(3)*. A definition of each can be found in Table 4.1. Each is essentially a moment of the image.

To use these parameters, simulated air showers are used to determine the range of values for each parameter occupied by air showers of different primary

Parameter	Description
Distance	Distance of the image centroid from the center of the FoV.
Width	R.M.S. spread of the light perpendicular to the major axis.
Length	R.M.S. spread of the light parallel to the major axis.
Miss	Perpendicular distance of the center of the FoV from the image axis.
Azwidth	R.M.S image width relative to an axis through the centroid and the center of the FoV.
Asymmetry	Measure of the asymmetry in the distribution along the major axis.
Alpha	Angle between the line from the centroid to the center of the FoV and the major axis of the image.
Size	The total charge in all image pixels, corresponding to the total light of the image.
Frac(3)	Percentage of the image's light content contained in the 3 brightest pixels.

Table 4.1 A summary of the Hillas parameters as laid out in [Hillas 1985]. Note that Frac(3), Asymmetry and Alpha are later variations on the original parameters.

particles. For single telescope images, Hillas predicts that specifying each event must have at least four (4) parameters within the gamma-ray primary "phase space" to allow for effective discrimination against non-gammas. For multiple telescope data, the Hillas parameters (specifically *Distance*, *Width*, *Length* and *Size*) are primarily used to select good-quality images to use in event reconstruction.

4.7 Stereo Parameterization

The advantage of the current generation of VHE Čerenkov arrays over the previous generation of single telescope instruments is that of stereo reconstruction of events. In VERITAS, individual telescope images are combined to obtain shower-level information. Of primary value are the arrival direction of the shower, and the *Shower Core*, the projected point of shower intersection with the plane of the telescope.

4.7.1 Quality Cuts

In order to ensure well parameterized events, a set of cuts is established in order to eliminate events without a high probability of correct reconstruction. For this work, the *Size*, *Distance*, and the total number of pixels in the image are used to select for quality image events. In addition to image quality selection, cutting is done on parameters to select for event quality as well. For this work, telescope multiplicity is used- telescopes without at least two good telescope images are eliminated, as are those with images only in T1 and T4. This last cut is due to the proximity of T1 to T4; a short baseline increases the number of coincidence triggers by small showers. Both the image quality and event quality cuts are given in 4.8.1. These cuts are made in Stage 4.2 of VEGAS.

4.7.2 Shower Direction Reconstruction

As mentioned before, the arrival direction of the primary particle can be traced back by determining the intersection of the major axes of the images from each camera in the field of view (FoV) of the telescope. Given that a perfect intersection of these axes does not always occur, the perpendicular distances of each image's major axis from a potential core position is weighted by the image's *Size*. This weighted distance is then minimized to determine the reconstructed shower direction.

The angular parameter θ^2 is defined as the square of the angular distance between an event's reconstructed intersect point and the targeted source position or test position. This value is useful for rejecting background events and generally specifying the reconstructed direction of an event in useful terms. θ^2 cuts are carried out in Stages 5 and 6 and are particularly important for extended sources.

4.7.3 Mean Scaled Width & Length

The Mean Scaled Width (MSW) and Mean Scaled Length (MSL) are extremely useful properties for discriminating between gamma-ray and hadronic events. The Mean Scaled (MS) parameters are obtained for each event from the measured

image length and the simulated length as drawn from a look-up table of simulations. For an individual telescope, we define the Scaled Width/Length to be

$$SW = \frac{W}{\langle W_{sim}(S,I)\rangle} \tag{4.7}$$

where W is the measured image length for an event, and $\langle W_{sim}(S,I)\rangle$ is the simulated image width value read from the look-up tables using the measured size S and the measured impact parameter, I. The scaled length is determined similarly. For an array of n telescopes one can find the MS parameters

$$MSW = \frac{\sum_i^n S_i(SW_i)}{\sum_i^n S_i} \tag{4.8}$$

$$MSL = \frac{\sum_i^n S_i(SL_i)}{\sum_i^n S_i} \tag{4.9}$$

which are thus effectively weighted per event by the image size S.

4.7.4 Energy Reconstruction

Energy estimation, when carried out, requires the usage of an energy lookup table. The primary particle energy is calculated as an average of the individual telescope image energies. These values are estimated from the look-up table based on the image size. The fractional error in energy reconstruction is given by

$$\Delta E = \frac{E_{rec} - E_{true}}{E_{true}} \tag{4.10}$$

where E_{rec} is the reconstructed energy, and E_{true} is the true energy. The mean value of ΔE, ϵ_{bias}, gives a good measure of how trustworthy the energy reconstruction is, and a bias of greater than 10% is typically not used.

4.7.5 Gamma/Hadron Separation

The separation out of hadronic events from our gamma-ray events is crucial to our ability to do astronomy with VHE gamma rays. Luckily, the established

properties of MSW, MSL and θ^2 prove to be excellent discriminators. Again, the values of these cuts used in this work are given in 4.8.1.

4.7.6 Background Estimation

In order to derive any meaning from a number of "ON" events satisfying all the given cuts, we must establish a similar "OFF" value without any expected association with our putative source. Assuming an isotropic cosmic ray background, the estimation of background can be accomplished from events in our same FoV. We can then establish an excess of events from our putative source

$$N_{Excess} = ON - \alpha OFF \tag{4.11}$$

where α is a normalization between the ON and OFF regions' effective exposures. Two methods are employed for background estimation

Reflected Region Model

In this method, the source offset from the center of the field of view is exploited by defining a number of regions of extent equal to the source region at the same offset from the center of the field of view, but well away from the source region. For this method, α is simply

$$\alpha_{refl} = \frac{1}{N} \tag{4.12}$$

Ring Background Model

The Ring Background Model (RBM) defines an annulus around every possible source region in the field of view and uses it to calculate an OFF value. Thus every point has a value for the excess and significance, making this method preferable for survey analysis and poorly localized sources. Since the annulus covers a range of radial values, the overall acceptance of the camera must be considered as it

Stage	Input	Description
Stage 1	data or laser .vbf file	Calibration calculations, relative gains from laser files
Stage 2	data and laser stage1 output (.root) file	Application of calibration and relative gain information to data.
Stage 4.2	stage2 output	Event cleaning, picture/boundary cutting and shower reconstruction.
Stage 5	stage4.2 output	Optional- stereo parameter cutting
Stage 6	stage4.2 or stage5 output	Stereo parameter cutting; statistics and plot/distribution production.

Table 4.2 The stages of VEGAS as of version 2.0.5.

is not uniform over the FoV. To first order, the acceptance depends only on radius, thus

$$\alpha_{RBM} = \frac{\int^{source} \epsilon(r) dA}{\int^{ring} \epsilon(r) dA} \tag{4.13}$$

where ϵ(r) is the radial acceptance profile.

4.8 VEGAS Analysis

VEGAS (Very Energetic Gamma-Ray Analysis Suite) is a multi-staged offline analysis system for VERITAS data. VEGAS was developed by VERITAS' Offline Analysis Working Group (OAWG) as the primary analysis suite for all VERITAS data (Cogan 2008). A VEGAS analysis, along with one other secondary analysis, is required for all published results to ensure consistent results.

Updated versions of VEGAS were released during the completion of this work. The final analysis for all sources has been completed with v2.0.5.

4.8.1 Events Cuts

The cuts used on each source are based on the standard optimized cuts for VEGAS 2.0.4, with small modifications for individual sources.

Targeted Remnants

Stage 1/2: 7-sample window

Stage 4.2: distance >1.43
size >400/1000 dc
Ntubes $\geq$ 5
Exclude T1-T4 pairs

Stage 6: *3% Crab Cuts*
$0.05 \leq$ MSW ≤ 1.20
$0.05 \leq$ MSL ≤ 1.49

100% Crab Cuts
$0.05 \leq$ MSW ≤ 1.20
$0.05 \leq$ MSL ≤ 1.49

In addition to the above, a limit was placed for each source on the allowed θ^2 value- the angular distance of a given reconstructed event from the source position- for the ON events. This value was increased for remnants that are extended beyond

the optimized θ^2 value for a point source. The θ^2 values for each remnant are given in, e.g., Table 5.1.

Cygnus Remnants

Stage1/2:	12-sample window
Stage 4.2:	distance <1.43
	size >600/1000 dc
	Ntubes $\geq$ 5
	Excludes T1-T4 pairs
Stage 6:	$0.05 \leq$ MSW ≤ 1.23
	$0.05 \leq$ MSL ≥ 1.35

To maintain consistency with the standard Sky Survey analysis, only two values for θ^2 are used: $\theta^2 = 0.014$ (point-like) and $\theta^2 = 0.055$ (extended). In the cases where a remnant's angular extent in some dimension is greater than twice the extended θ cut value, we accept an additional trials factor of r_a^2/θ^2

4.8.2 Flux Determination

Extraction of any flux value from photon rate data requires a measurement of the effective collection area of our instrument. In the case of VERITAS this effective area is strongly dependent on a number of factors:

- **Energy:** As the size of the shower pool strongly varies with energy, the distance of the shower core from the center of VERITAS at which the shower can still be meaningfully resolved
- **Offset:** The strong change in sensitivity across the VERITAS camera means that the effective area of the instrument as a whole depends on what offset the presumptive source is observed.
- **Noise Levels:** The presence of a strong background light component reduces the effective area.
- **Zenith Angle:** The zenith angle of a given observation determines the air mass through which the observed showers propagate.

To account for these variables, models of extensive gamma-ray air-shower must be analyzed and reconstructed in a similar fashion to the process described above for real data. Effective area tables are then generated from the Stage 4.2 output. For each such model, the reconstructed energies of the simulated showers are compared to the true energies of the original simulated particle. For this work each generated effective area is only used if the reconstructed energies are within 10% of the energy range. Since reconstruction will typically grow less accurate at more extreme energies, we can define a "safe energy range" for employing each effective area. The effective area tables are used either by Stage 6 in its spectral calculations, or by a secondary macro for determining photon flux upper limits.

Significances are determined via the method described by [Li and Ma 1983] . The significance at a given point can best be described as the confidence with which the null hypothesis- here, that all counts in the ON region are from a uniform background- is rejected. This significance (in standard deviations or σ) is given by

$$\begin{aligned} S &= \Big[2N_{\mathrm{ON}} ln \left\{ \frac{(1+\alpha)}{\alpha} \frac{N_{\mathrm{ON}}}{N_{\mathrm{ON}} + N_{\mathrm{OFF}}} \right\} \\ &\quad + 2N_{\mathrm{OFF}} ln \left\{ (1+\alpha) \frac{N_{\mathrm{OFF}}}{N_{\mathrm{ON}} + N_{\mathrm{OFF}}} \right\} \Big]^{1/2} \end{aligned} \tag{4.14a}$$

Since the exact nature and intensity of the signal from a source is not known *a priori*, multiple attempts to detect a source are often made with the same data. In the case of VERITAS, any variation in the cuts employed is considered such a trial. These trials affect the reportable statistical certainty of detection. For a single trial, the probability of a positive result is given by

$$P = N(u = S; 0, 1) = \frac{1}{\sqrt{2\pi}} \int_{-\infty}^{S/\sqrt{2}} e^{-x^2/2} dx \tag{4.15}$$

i.e., the normal distribution function for a mean of 0 and a standard deviation of 1. Since we are interested in rejecting our null hypothesis, the appropriate single trial probability of a real source is given by:

$$P_1 = 1 - P \tag{4.16}$$

For n trials, this becomes:

$$P_n = (1 - P)^n \tag{4.17}$$

As is standard, a 5-sigma post-trials significance is considered the threshold of detection in this work.

The gamma-ray rate (photons s^{-1}) and its uncertainty are given by

$$R_\gamma = \frac{\mathrm{ON} - \alpha \mathrm{OFF}}{T} \tag{4.18}$$

$$\sigma_R = \pm \frac{\mathrm{ON} - \alpha \mathrm{OFF}}{T \times S} \tag{4.19}$$

where T is the livetime of the observation and α is the ratio of the ON and OFF exposure. In Wobble data, the On and Off exposure times are always the same. α then is the simply the ratio of the areas of the source region and the background region(s).

Once a gamma-ray rate is established for the source and effective areas are generated for the relevant observation parameters, a flux or upper limit can be established. The total rate of events counted from a source can be represented as

$$R = \int_0^\infty A(E)\Phi(E)dE \tag{4.20}$$

Where Φ is the incident source flux, R is the (known) event rate and A(E) is the true effective area of our telescope at energy E. As discussed in 1.5.3, a simple falling power law form is assumed for all sources.

$$\Phi(E) = \Phi_0 E^{-\Gamma} \tag{4.21}$$

In the case of Cassiopeia A and the Crab Nebula, spectral fitting is carried out in stage6 to determine appropriate spectral index. A power law of γ = -2.5 is applied for those sources without sufficient statistics to carry out spectral fitting.

It should be noted that A(E) is the effective area selected to match the zenith, azimuth and noise levels appropriate for the observation.

In practice, we must treat our effective areas as constant over some finite bin width.

$$R_i = \frac{C_i}{T} = \int_{E_{iMin}}^{E_{iMax}} \Phi(E)A(E)dE = \Phi_0 A_i (E_{iMax}^{1-\Gamma} - E_{iMin}^{1-\Gamma})(1-\Gamma)^{-1} \tag{4.22}$$

summing over i then gives us

$$R = \Phi_0 A_i (E_{iMax}^{1-\Gamma} - E_{iMin}^{1-\Gamma})(1-\Gamma)^{-1} = \Phi_o \hat{A} \tag{4.23}$$

$\hat{A}$ here is the spectrally convolved effective area. Thus, our flux normalization is simply

$$\Phi_0 = \frac{R}{\hat{A}} \tag{4.24}$$

and our integrated flux is

$$F = \int_{E_{thresh}}^{E_{max}} \Phi(E)dE = \Phi_0 (E_{max}^{1-\Gamma} - E_{thresh}^{1-\Gamma})(1-\Gamma)^{-1} \tag{4.25}$$

4.8.3 Upper Limits

All upper limits are determined by the statistical technique outlined in [Helene 1983]. The statistical confidence with which we can state that the counts

Object	Data Type	VEGAS through stage6	Spectral Analysis	Analysis Notes
Crab Nebula	0.5 Wobble	✓	✓	Calibration source
Cas A	0.5 Wobble	✓	✓	
CTB 109	0.5 Wobble	✓	✗	Extended Source
W44	0.5 Wobble	✓	✗	Extended Source
Tycho	0.5 Wobble	✓	✗	
G67.7+1.8	Survey Mode	✓	✗	
G68.6-1.2	Survey Mode	✓	✗	
G69.0+2.7	Survey Mode	✓	✗	
G69.7+1.0	Survey Mode	✓	✗	
G73.9+0.9	Survey Mode	✓	✗	
G74.9+1.2	Survey Mode	✓	✗	
G76.9+1.0	Survey Mode	✓	✗	
G78.2+2.1	Survey Mode	✓	✗	

Table 4.3 Summary of the analyses applied to each source.

collected from a source were less than or equal to a particular value C_{UL} is (1 - β), where

$$\beta = I\left(\frac{C_{UL} - ON + OFF}{\sqrt{ON + \sigma_B^2}}\right) / I\left(\frac{-ON + OFF}{\sqrt{ON + \sigma_B^2}}\right) \tag{4.26}$$

ON and OFF are the count values for the On and Off regions, σ_B is the standard deviation on the background counts, and I is the error function

$$I(z) = \frac{1}{\sqrt{2\pi}} \int_z^\infty e^{-z^2/2} dz \tag{4.27}$$

CHAPTER 5

RESULTS

5.1 Chapter Overview

In the first portion of this chapter the results of the targeted remnant observations are discussed individually. In Section 5.8, the collective Sky Survey results are discussed, with each remnant singled out as warranted.

5.2 Trials

In properly reporting the significance of detection for our sources, we must account for the independent trials applied in analyzing the data. While not necessarily strictly independent, we conservatively account for each application of a different θ^2 or digital count cut as a separate trial. For each of the targeted remnants, then, we apply a trials factor of 4 in reducing the measured significance. In the case of those Sky Survey Remnants with an angular diameter less than the applied θ^2 cut, we have only 2 trials- the two minimum limits of 600 and 1000 image digital counts. For those in which the applied standard θ^2 cut is less than the expected angular diameter, we accept a trials penalty for searching the full area of the remnant for significant emission. Thus, for these remnants we apply a trials penalty of $\frac{\theta^2}{r_{SNR}^2}$, where r_{SNR} is the remnant's angular radius.

5.3 Crab Nebula

As the first confirmed steady astrophysical TeV source, the Crab Nebula (G 184.6-5.8) serves as a standard candle for VHE gamma ray telescopes. The Crab analysis in this work is presented as both a proof-of-technique and as a standard analysis against which other remnant analyses may be compared. In some previous work in this field, gamma ray rates for potential sources were often presented in terms of a "% Crab" rate in order to allow an easier conversion of gamma ray rate to gamma ray flux. However, given the strong dependence of the flux on factors

such as observation zenith angle and telescope multiplicity, gamma ray rates for different targets are not necessarily directly comparable. Instead, we independently derive the fluxes (or flux upper limits) for each remnant. This takes into account the varying observational parameters through the effective area lookup tables. For convenience, we then convert this flux to a % Crab flux for ready comparison.

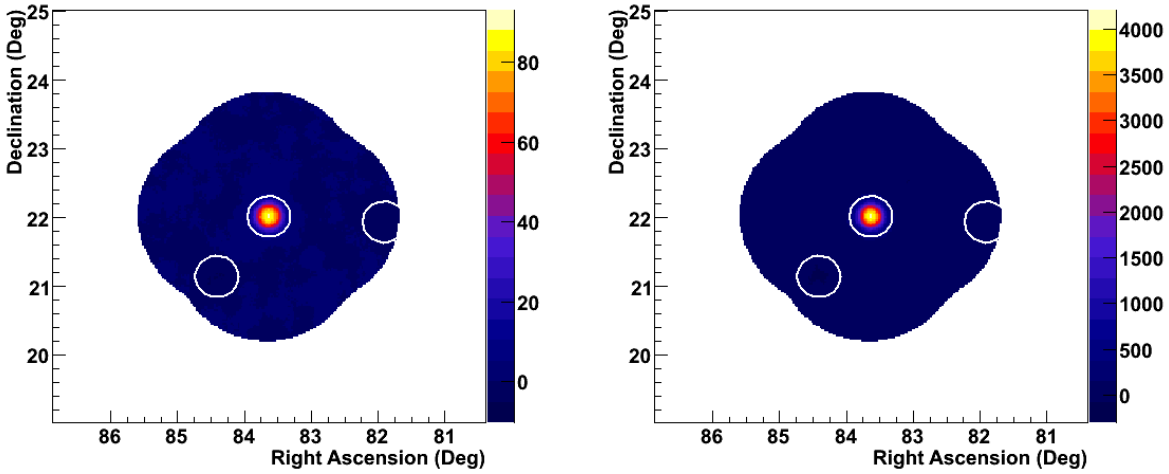

Figure 5.1 The plot of the excess counts (left) and the Ring Background Model-derived significance (right) for the Crab Nebula for a size cut >400 digital counts. The white ring indicates the exclusion regions for the remnant and the bright stars ζ Tau and o Tau.

5.3.1 Source Detection

Emission from the Crab Nebula is clearly detected in the analysis of the 31 runs presented here. For our standard-cuts analysis, we arrive at a significance of 75 σ. For the hard-cuts analysis, we find a lower significance of 41 σ. As will be discussed later, the reason for this severe reduction is not entirely clear since we do not expect to preferentially cut on source rather than background cuts. Given the higher significance of detection, any quantities derived from this point are from the

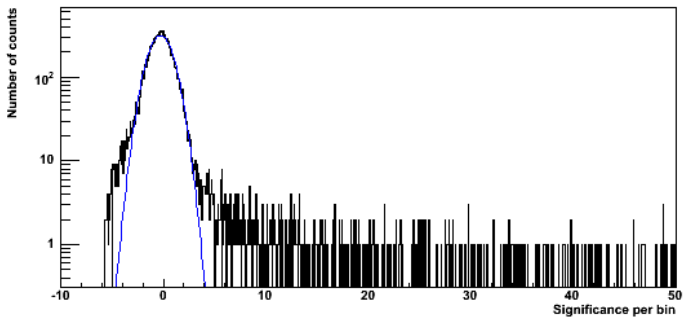

Figure 5.2 The plot of the distribution of significances in the Crab Nebula FoV. In the case of a clear detection such as this, the distribution is extended well beyond the normal distribution (blue line).

standard cuts analysis unless otherwise stated. From the determined excess events and the effective area table, we derive a flux of $1.33 \pm 0.028 \times 10^{-10}$ cm^{-2} s^{-1} TeV^{-1}.

5.3.2 Spectrum

The spectrum for the Crab Nebula is given in Figure 5.3. Fitting a simple power-law, we derive a spectral index of $-2.35 \pm 0.25_{stat}$, with a flux normalization of $(-2.9 \pm 0.071_{stat}) \times 10^{-7} \gamma$ m^{-2} s^{-1} TeV^{-1}. This is within systematic errors of the VERITAS Crab spectrum from Celik (2008). For the purposes of systematic error estimation, we will use in this work the estimates from Celik (2008), of 22% for the flux normalization N, and 0.17 for the spectral index. This estimate accounts for errors in atmospheric and shower modeling, detector response, variation in observing conditions and uncertainties in the offline data analysis.

Integrating the power-law fit above 300 GeV gives us a a total flux of $F = (1.10 \pm 0.31) \times 10^{-10}$cm^{-2}s^{-1}. This lies within errors of both our directly derived source flux and canonical values for the Crab.

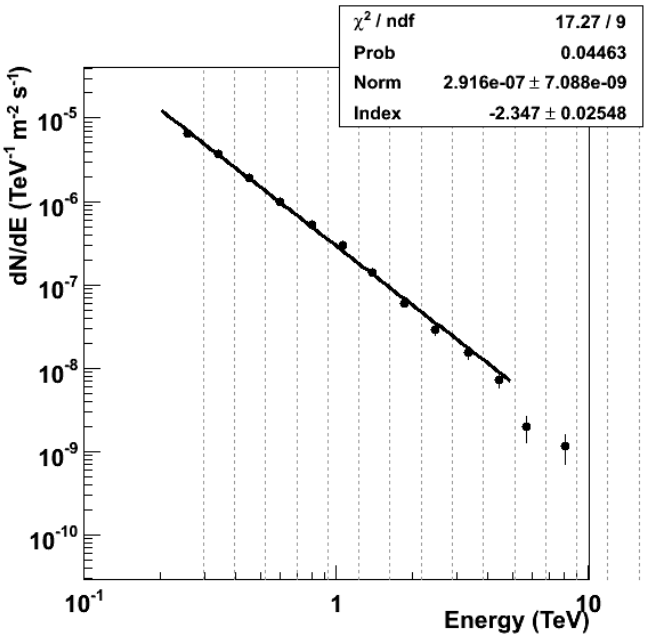

Figure 5.3 The differential flux spectrum for the Crab Nebula for the standard cuts analysis, fit with a simple falling power law.

5.4 Casseiopeia A

Cassiopeia A, as another known TeV SNR, is a secondary point of comparison for our analysis with known quantities. As discussed in 1.6.2, recent MAGIC observations give a flux above 1 TeV of $7.3 \pm 0.7_{stat} \pm 2.2_{sys}) \times 10^{-13}\mathrm{cm}^{-2}\mathrm{s}^{-1}$ and a power-law spectrum with $\Gamma = 2.3 \pm 0.2_{stat} \pm 0.2_{sys}$ and $\mathrm{N} = (1.0 \pm 0.1_{stat} \pm 0.3_{sys}) \times 10^{-12}\mathrm{TeV}^{-1}\mathrm{cm}^{-1}\mathrm{s}^{-1}$ (Albert et al. 2007a).

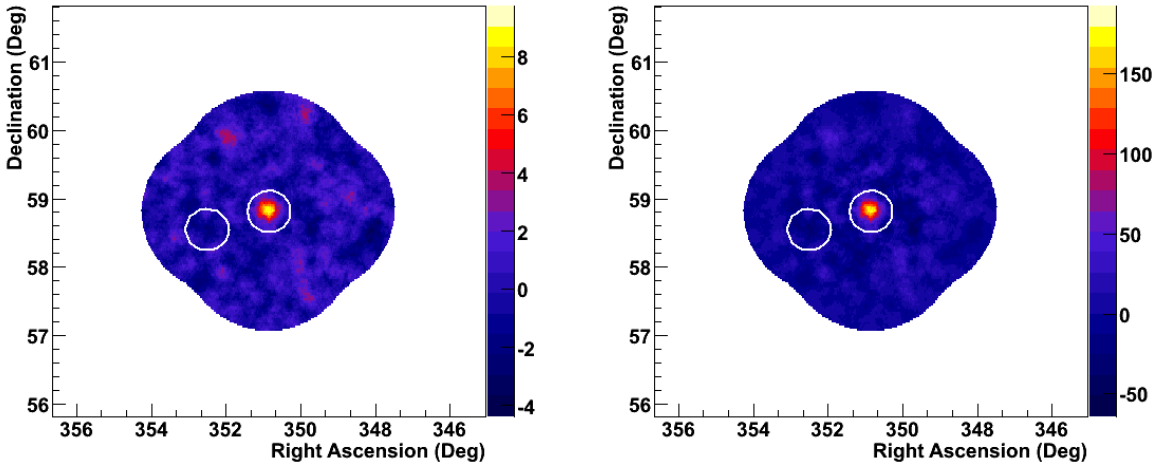

Figure 5.4 The plot of the excess counts (left) and the Ring Background Model-derived significance (right) for the Cassiopeia A for a size cut >400 digital counts. The white ring indicates the exclusion regions for the remnant and the bright star AR Cas.

5.4.1 Source Detection

Cassiopeia A is clearly detected in the analysis of the ∼1150 minutes of observation presented here. For our standard-cuts analysis, we arrive at a pre-trials significance of 7.1σ. For the hard-cuts analysis, we find a lower significance of 5.6 σ. From the determined excess events and our effective area table, we derive a flux of $2.5 \pm 0.39 \times 10^{-12}$ cm^{-2} s^{-1} TeV. We report here the results of the 3% Crab source optimized analysis for Cas A.

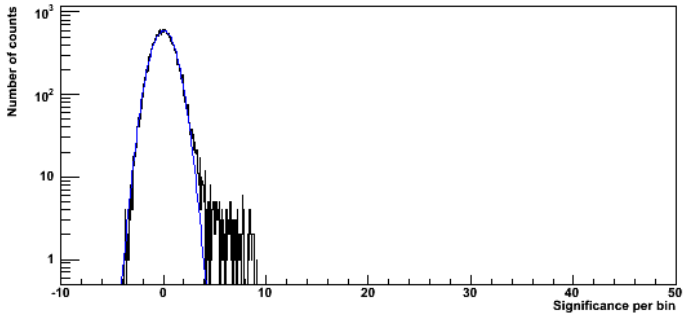

Figure 5.5 The plot of the distribution of significances in the Cassiopeia A field of view. In the case of a clear detection such as this, the distribution is extended well beyond the normal distribution (blue line).

5.4.2 Spectrum

The spectrum for Cassiopeia A is given in Figure 5.6. Fitting a simple power-law, we derive a spectral index of $-2.8 \pm 0.26_{stat}$, with a flux normalization of $(7.1 \pm 1.1_{stat}) \times 10^{-9}\gamma$ m^{-2} s^{-1} TeV^{-1}. This result appears to show a steeper spectral fall off than the MAGIC result, but normalization and spectral index lie within errors of the MAGIC value.

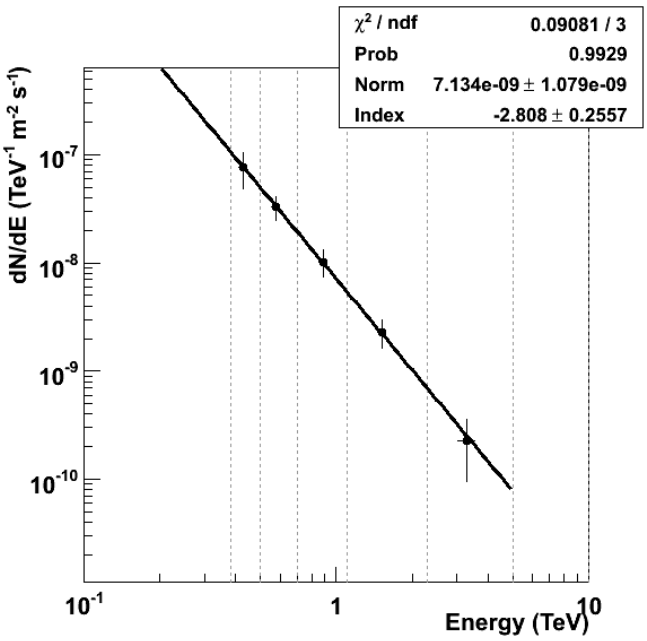

Figure 5.6 The differential flux spectrum for Cassiopeia A. Dotted lines indicate the edges of the energy bins.

5.5 Tycho's SNR (G120.1+1.4)

The remnant of SN 1572, known as Tycho's Supernova (G120.1+1.4), is a young Type Ia remnant. It has been the target of several investigations in the TeV regime, and HEGRA established a 3σ upper limit of $5.78\times10^{-13}\gamma$ cm^{-2} s^{-1}, or 3.3% Crab, above 1 TeV. We present here the results of the 3% Crab source optimized analysis.

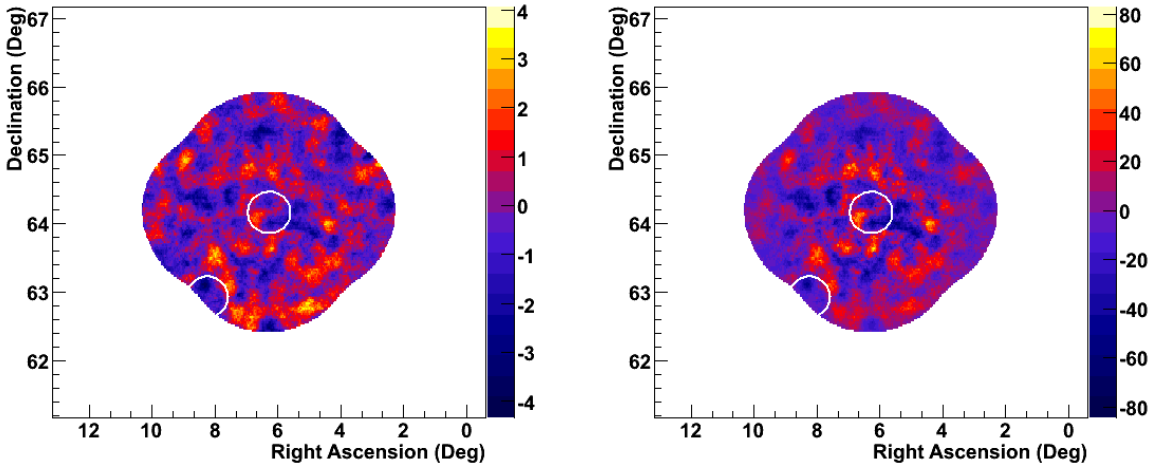

Figure 5.7 The plot of the excess counts (left) and the Ring Background Model-derived significance (right) for Tycho's SNR for a size cut >400 digital counts.

5.5.1 Upper Limit

We make no significant detection of Tycho in the ∼1250 minutes of data presented in this work, with either set of cuts or background modeling method. From the standard energy cuts analysis, we can establish a 99% upper limit on emission from Tycho above 300 TeV $F_{UL} = 1.0 \times 10^{-12}\gamma$ cm^{-2} s^{-1}.

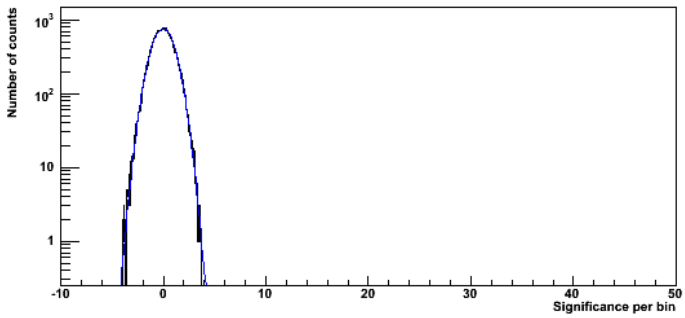

Figure 5.8 The plot of the distribution of significances in the Tycho FoV. The distribution is well matched to the normal distribution (blue line).

5.6 W44 (G34.7-0.4)

Within the same field of view as W44 are two unidentified VHE sources: HESSJ 1857+026 and HESSJ 1858 + 020. Both have extended morphologies consistent with PWN emission and do not appear to be associated with W44. If these sources are indeed unrelated, then their presence within a few degrees of one another is a striking commentary on the growing abundance of observed VHE emitters.

W44 has previously been observed by a number of ground-based Čerenkov detectors (Buckley et al. 1998), . The lowest available upper limit is $F_{UL}(E > 1.36TeV) = 3.6 \times 10^{-12}\gamma \text{ cm}^{-2} \text{ s}^{-1}$ presented by Yukawa (2008). Deeper limits may be determined as a part of the HESS Galactic Plane Survey or the MAGIC observations (Bartko et al. 2008), but these are as yet unpublished.

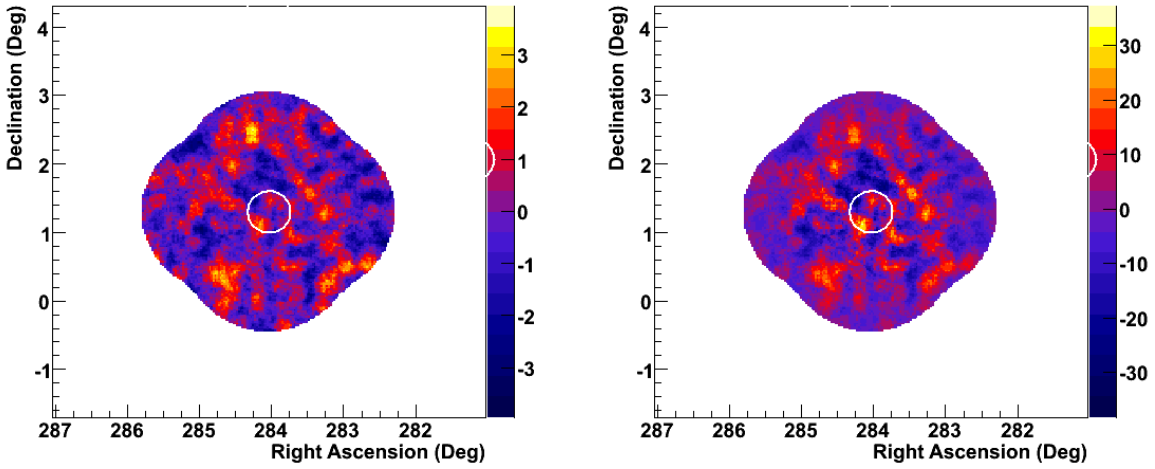

Figure 5.9 The plot of the excess counts (left) and the Ring Background Model-derived significance (right) for W44 for a size cut >400 digital counts. The white circle indicates the region excluded from the background model for the remnant.

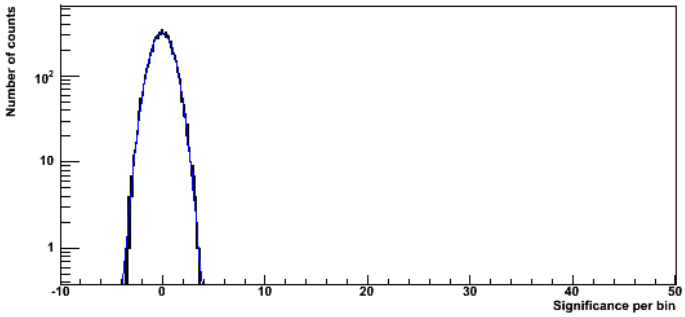

Figure 5.10 The plot of the distribution of significances in the W44 FoV. The distribution is well matched to the normal distribution (blue line).

5.6.1 Upper Limit

We make no significant detection of W44 in the ∼500 minutes of data presented in this work, with either set of cuts or background modeling method. We employed a widened θ^2 cut of 0.09 to encompass the entirety of the remnant. From the standard energy cuts analysis, we can establish a 99% upper limit on emission from Tycho above 300 TeV $F_{UL} = 2.6 \times 10^{-12}\gamma$ cm^{-2} s^{-1}.

5.7 CTB 109 (G109.1-1.0)

Because of its high positive declination, CTB 109 is accessible to neither HESS nor CANGAROO. Despite extensive measurements at a variety of wavelengths, no published upper limits for VHE gamma ray emission exist for CTB 109.

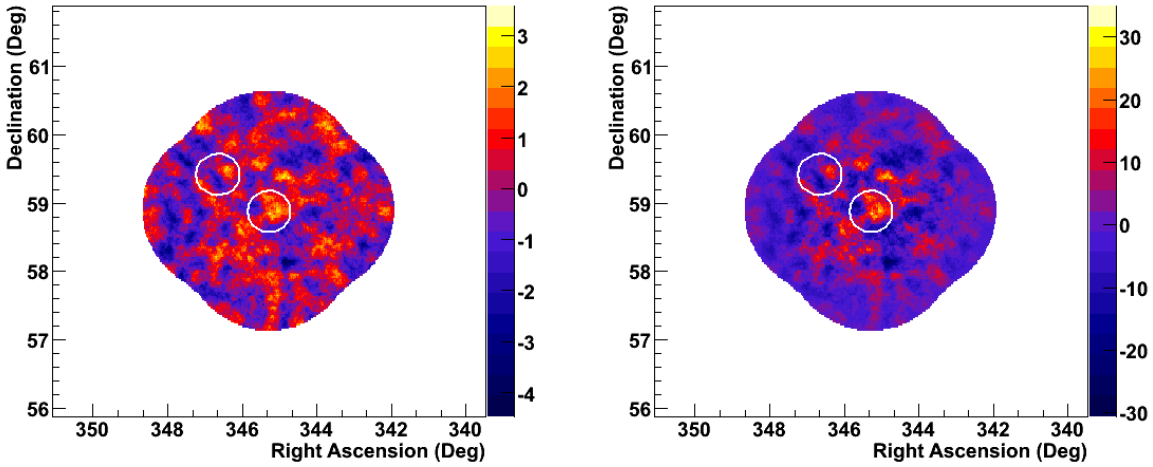

Figure 5.11 The plot of the excess counts (left) and the Ring Background Model-derived significance (right) for CTB 109 for a size cut >400 digital counts. The white circles indicate the regions excluded from the background model for the remnant and the bright star 1 Cas.

5.7.1 Upper Limit

We make no significant detection of CTB 109 in the $\tilde{3}50$ minutes of data presented in this work, with either set of cuts or background modeling method. We employed a widened θ^2 cut of 0.09 to encompass the entirety of the remnant. From the standard energy cuts analysis, we can establish a 99% upper limit on emission from Tycho above 300 TeV $F_{UL} = 8.8 \times 10^{-12}\gamma$ cm^{-2} s^{-1}.

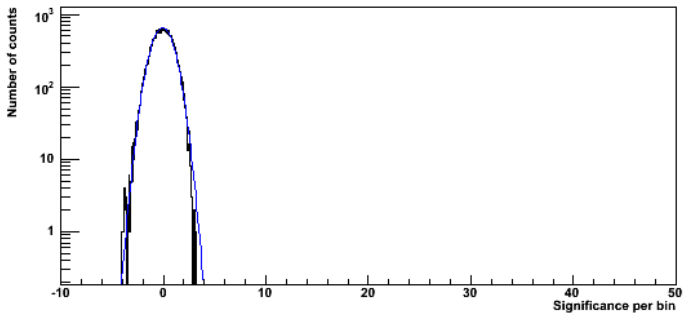

Figure 5.12 The plot of the distribution of significances in the CTB 109 FoV. The distribution is well matched to the normal distribution (blue line), indicating no meaningful excesses above the background.

Remnant	Livetime (min)	Cuts (%Crab)	θ^2	σ_{pre}	σ_{post}	Upper Limit	Flux	$\frac{F}{F_{Crab}}$
Crab Nebula	407.0	100%	0.0132	88.4	88.4	—	133 ± 2.75	1
Cas A	1168.7	3%	0.0132	9.11	9.00	—	2.52 ± .387	.019
CTB 109	342.2	3%	0.09	2.67	2.14	8.83	—	.066
W 44	492.9	3%	0.09	-1.36	—	2.61	—	.020
Tycho	1235.2	3%	0.0132	0.16	0.0	1.00	—	.0075

Table 5.1 A summary of the results for all of the targeted remnants for the 3% Crab cuts and dc >400. Upper limits at the 99% confidence level are given for those remnants with no detection. Both fluxes and upper limits are given in units of $10^{-12}\gamma$ cm^{-2} s^{-1}.

Remnant	Livetime (min)	Cuts (%Crab)	θ^2	σ_{pre}	σ_{post}	Upper Limit	Flux	$\frac{F}{F_{Crab}}$
Crab Nebula	407.0	100%	0.0132	71.4	71.3	—	27.0 ± 1.1	1
Cas A	1168.7	3%	0.0132	8.6	8.5	—	0.65 ± 1.4	.024
CTB 109	342.2	3%	0.09	2.8	2.3	1.60	—	.059
W 44	492.9	3%	0.09	0.10	0.0	0.31	—	.012
Tycho	1235.2	3%	0.0132	2.1	1.51	0.60	—	.022

Table 5.2 A summary of the results for all of the targeted remnants for the 3% Crab cuts and dc >1000. Upper limits at the 99% confidence level are given for remnants with no detection. Both fluxes and upper limits are given in units of $10^{-12}\gamma$ cm $^{-2}$ s^{-1}.

5.8 Cygnus Sky Survey Remnants

As discussed in Chapter 3, the Cygnus Sky Survey is an attempt at a large-scale observational survey at very high energy. The Sky Survey is one the VERITAS Key Science Projects for 2007 - 2008. The original objective was a uniform exposure over 30 degrees in Galactic latitude, taken over two observing seasons. Due to observational constraints, only the first half of the survey, originally slated to be completed in the fall of 2007, has been completed.

Within the completed portion of the Cygnus Sky Survey are located eight (8) supernova remnants in the Green's Catalog of Supernova Remnants (Green 2006). These remnants were selected out from the survey as being of particular interest for this work. The Sky Survey SNR are serendipitous observations with no special placement in the Sky Survey pointings. Thus, the Reflected Region method of background estimation is inappropriate, given the uneven nature of the exposure over the field of view. Since varying exposure is already accounted for in the Ring Background method, this technique is used exclusively here for significance estimation and flux upper limit derivation.

5.8.1 G 67.7 + 1.8

We make no significant detection of G67.7+1.8 in the ∼700 minutes of data presented in this work, with either set of cuts or background modeling method. From the standard energy cuts analysis, we can establish a 99% upper limit on emission from G 67.7 + 1.8 above 300 TeV $F_{UL} = 1.74 \times 10^{-12}\gamma$ cm^{-2} s^{-1}.

5.8.2 G 68.6 - 1.2

We make no significant detection of G 68.6 - 1.2 in the ∼700 minutes of data presented in this work, with either set of cuts or background modeling method. From the standard energy cuts analysis, we can establish a 99% upper limit on emission from G 68.6 - 1.2 above 300 TeV $F_{UL} = 3.63 \times 10^{-12}\gamma$ cm^{-2} s^{-1}.

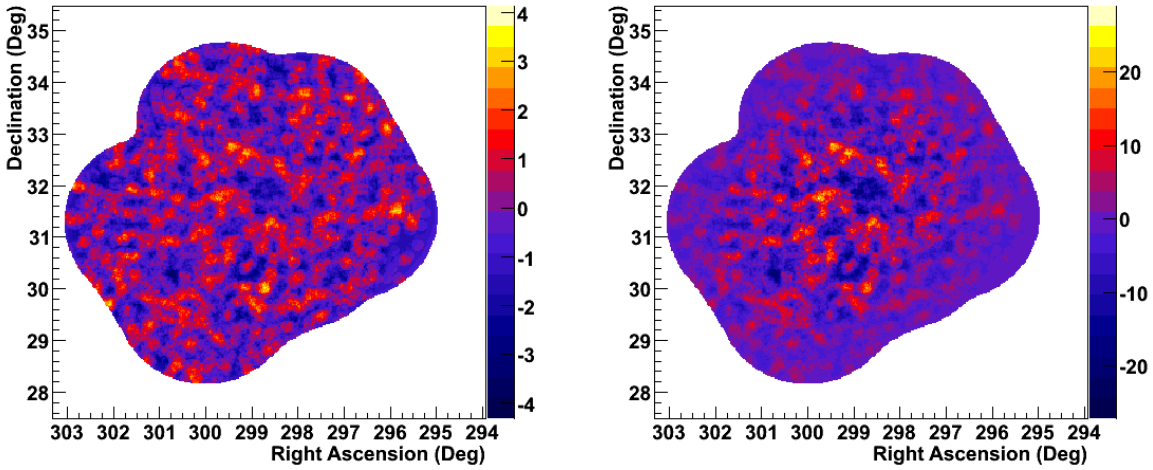

Figure 5.13 The plot of the excess counts (left) and the Ring Background Model-derived significance (right) for G67.7+1.8 for a size cut >600 digital counts.

5.8.3 CTB 80 / G69.0+2.7

We make no significant detection of G 68.6 - 1.2 in the ∼750 minutes of data presented in this work, with either set of cuts or background modeling method. From the standard energy cuts analysis, we can establish a 99% upper limit on emission from CTB 80 above 300 TeV $F_{UL} = 1.61 \times 10^{-12}\gamma$ cm^{-2} s^{-1}.

5.8.4 G 69.7+1.0

We make no significant detection of G 69.7 + 1.0 in the ∼650 minutes of data presented in this work, with either set of cuts or background modeling method. From the standard energy cuts analysis, we can establish a 99% upper limit on emission from G 69.7 + 1.0 above 300 TeV $F_{UL} = 2.11 \times 10^{-12}\gamma$ cm^{-2} s^{-1}.

5.8.5 G 73.9 + 0.9

We make no significant detection of G 73.9 + 0.9 in the ∼600 minutes of data presented in this work, with either set of cuts or background modeling method. From

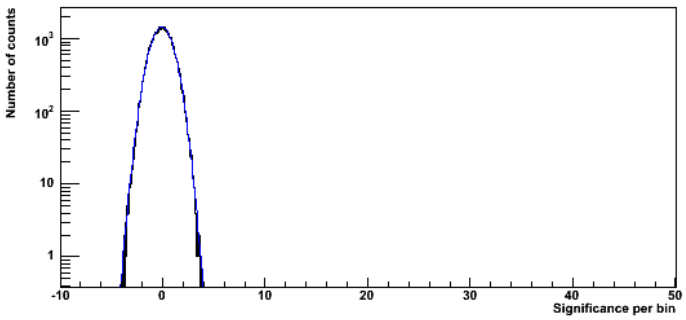

Figure 5.14 The plot of the distribution of significances in the G67.7+1.8 field of view. The distribution is well matched to the normal distribution (blue line), indicating no meaningful excesses above the background.

the standard energy cuts analysis, we can establish a 99% upper limit on emission from G 73.9 + 0.9 above 300 TeV $F_{UL} = 2.33 \times 10^{-12}\gamma$ cm^{-2} s^{-1}.

5.8.6 CTB 87 / G74.9+1.0

We make no significant detection of CTB 87 in the ∼550 minutes of data presented in this work, with either set of cuts or background modeling method. From the standard energy cuts analysis, we can establish a 99% upper limit on emission from CTB 87 above 300 TeV $F_{UL} = 6.69 \times 10^{-12}\gamma cm^{-2}$ s^{-1}.

5.8.7 G76.9 + 1.0

We make no significant detection of G 68.6 - 1.2 in the ∼700 minutes of data presented in this work, with either set of cuts or background modeling method. From the standard energy cuts analysis, we can establish a 99% upper limit on emission from G 76.9 + 1.0 above 300 TeV $F_{UL} = 1.57 \times 10^{-12}\gamma$ cm^{-2} s^{-1}.

5.8.8 γ Cygni/G78.2+2.1

Before trials, we find a hotspot within γ Cygni at 5.26 σ. After accounting for trials both in cuts and in the spatial search across the remnant, the significance of the hotspot is reduced below the threshold for detection. Given the highly suggestive

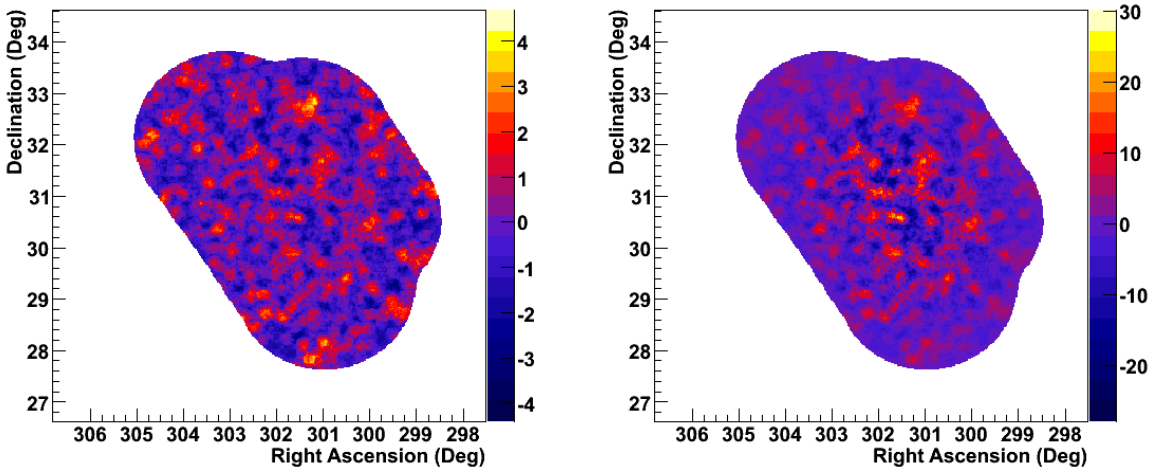

Figure 5.15 The plot of the excess counts (left) and the Ring Background Model-derived significance (right) for G68.6-1.2 for a size cut >600 digital counts.

nature of the excess, we present both the calculated flux and upper limit for γ Cygni. Above the 300 TeV, the excess corresponds to a 99% upper limit of $F_{UL} = 6.15 \times 10^{-12}\gamma$ cm^{-2}s^{-1} and a flux of $F = 4.82 \times 10^{-12}\gamma cm^{-2}$s^{-1}.

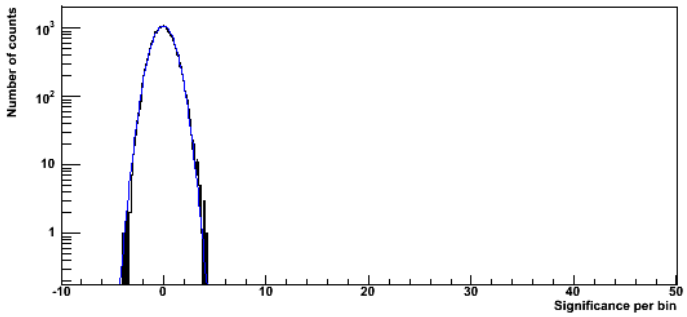

Figure 5.16 The plot of the distribution of significances in the G68.6-1.2 field of view. The distribution is well matched to the normal distribution (blue line), indicating no meaningful excesses above the background.

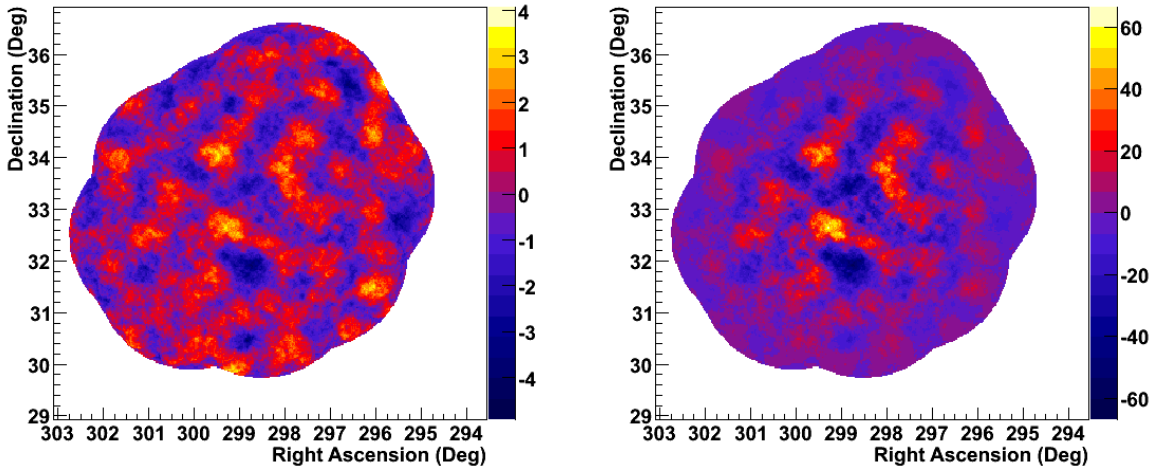

Figure 5.17 The plot of the excess counts (left) and the Ring Background Model-derived significance (right) for CTB 80 for a size cut >600 digital counts.

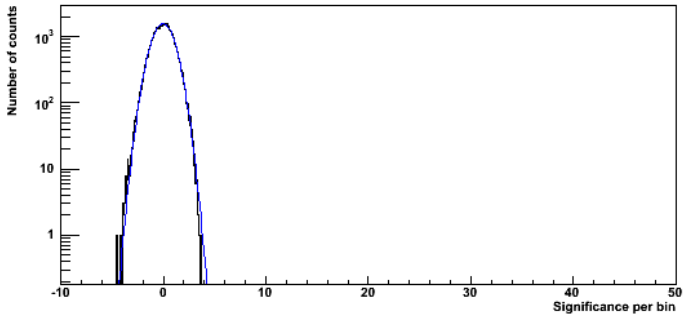

Figure 5.18 The plot of the distribution of significances in the CTB 80 field of view. The distribution is well matched to the normal distribution (blue line), indicating no meaningful excesses above the background.

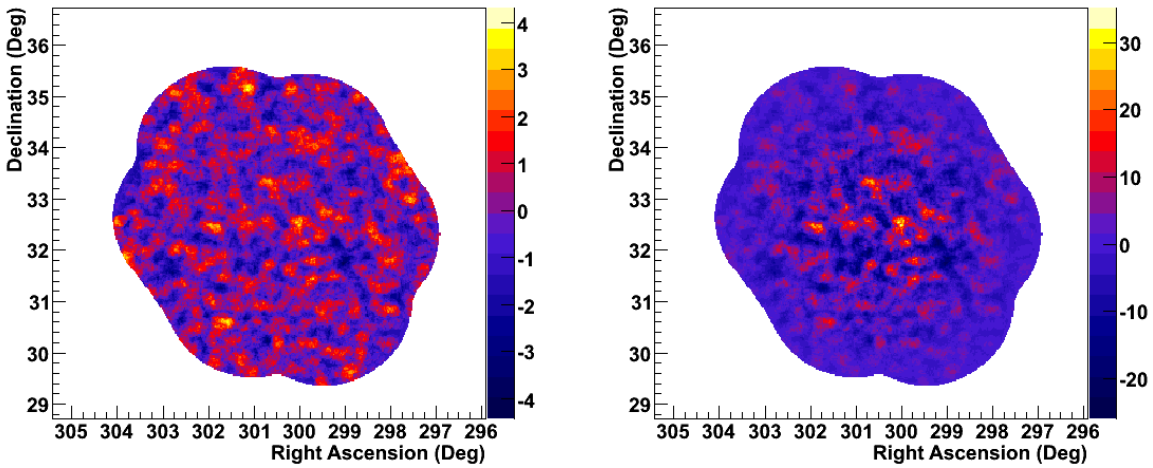

Figure 5.19 The plot of the excess counts (left) and the Ring Background Model-derived significance (right) for G 69.7+1.0 for a size cut >600 digital counts.

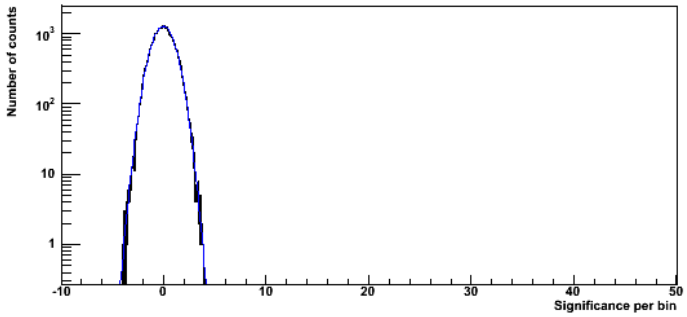

Figure 5.20 The plot of the distribution of significances in the G 69.7+1.0 field of view. The distribution is well matched to the normal distribution (blue line), indicating no meaningful excesses above the background.

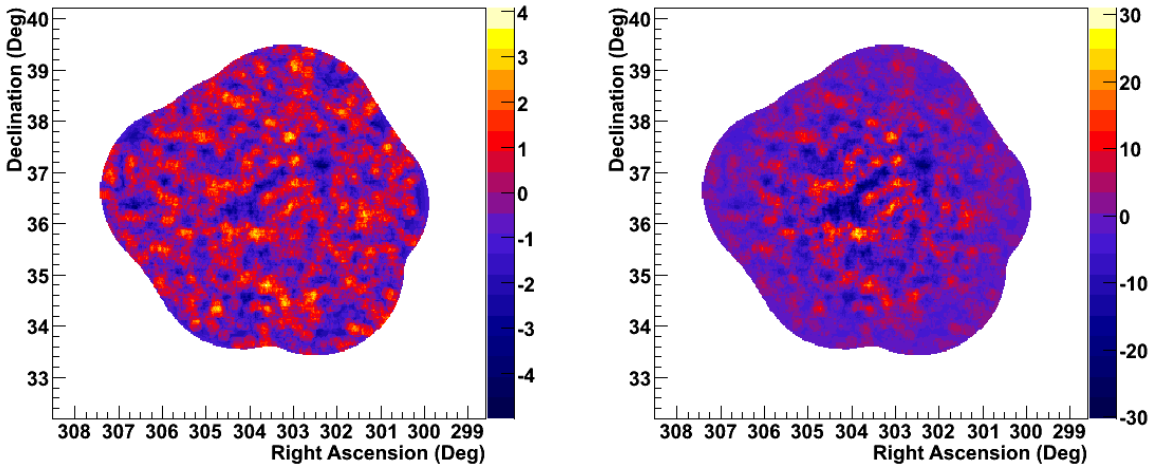

Figure 5.21 The plot of the excess counts (left) and the Ring Background Model-derived significance (right) for G 73.9 + 0.9 for a size cut >600 digital counts.

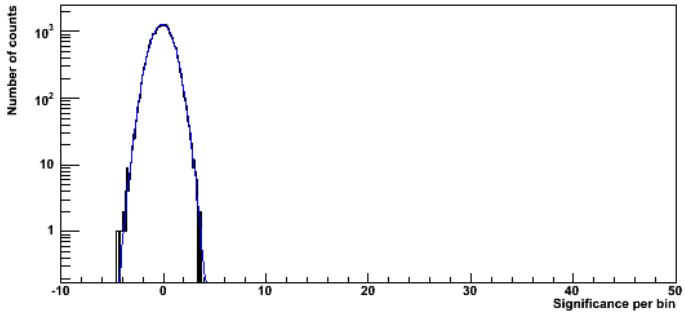

Figure 5.22 The plot of the distribution of significances in the G 73.9 + 0.9 field of view. The distribution is well matched to the normal distribution (blue line), indicating no meaningful excesses above the background.

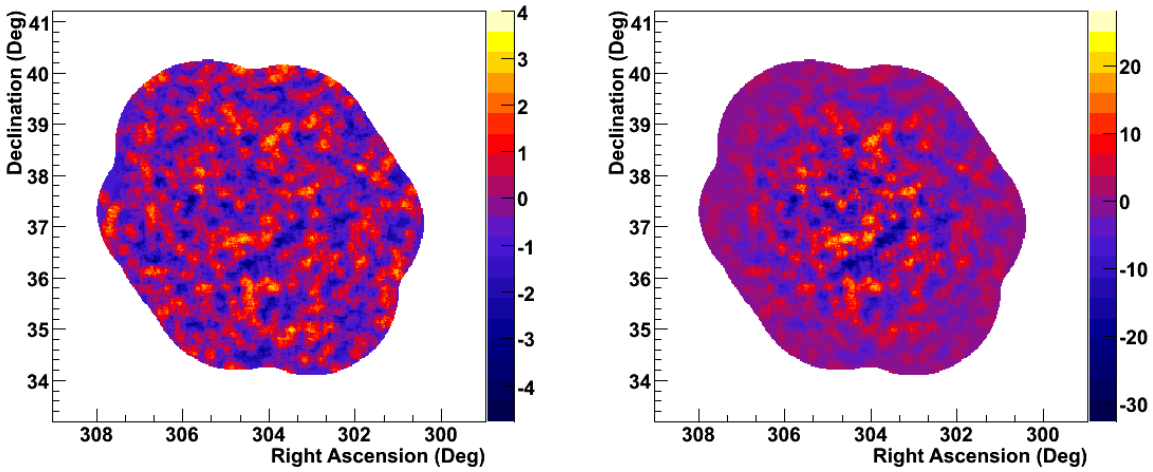

Figure 5.23 The plot of the excess counts (left) and the Ring Background Model-derived significance (right) for CTB87 for a size cut >600 digital counts.

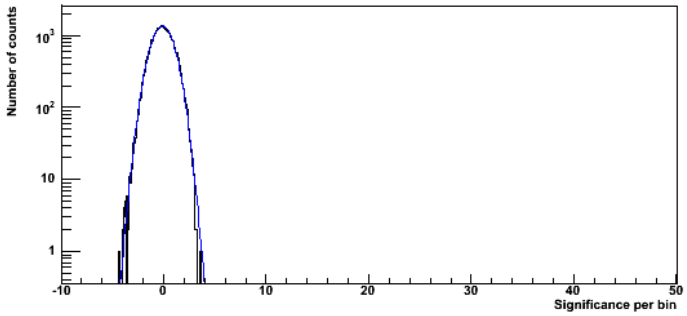

Figure 5.24 The plot of the distribution of significances in the CTB 87 field of view. The distribution is well matched to the normal distribution (blue line), indicating no meaningful excesses above the background.

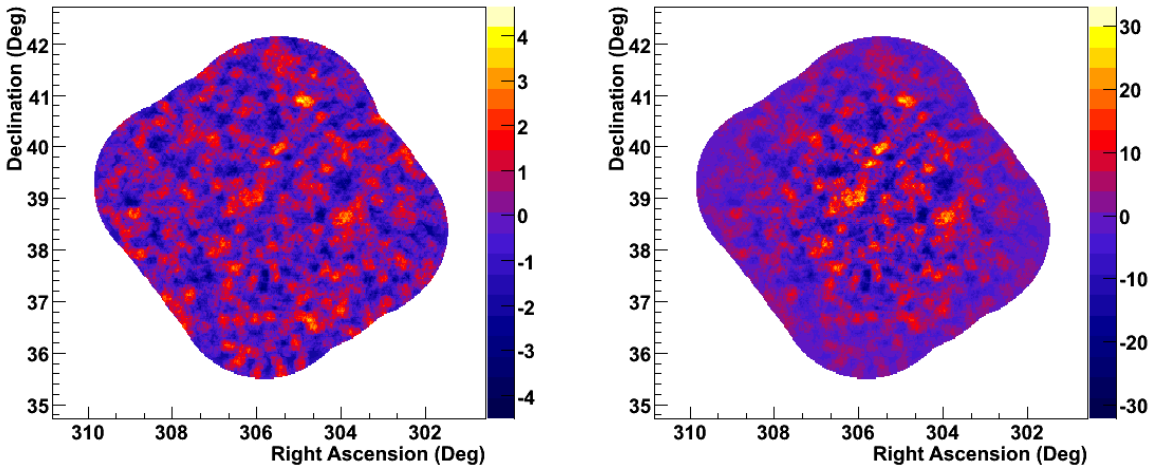

Figure 5.25 The plot of the excess counts (left) and the Ring Background Model-derived significance (right) for G76.9 + 1.0 for a size cut >600 digital counts.

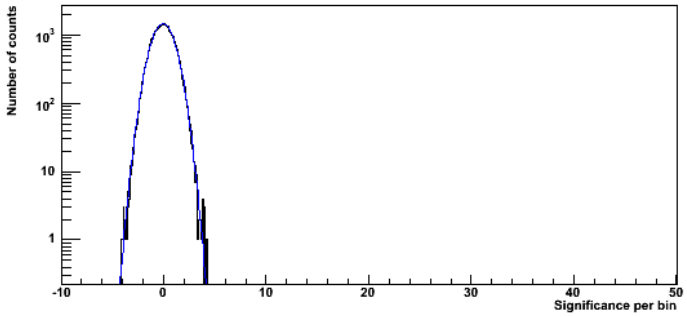

Figure 5.26 The plot of the distribution of significances in the G76.9 + 1.0 field of view. The distribution is well matched to the normal distribution (blue line), indicating no meaningful excesses above the background.

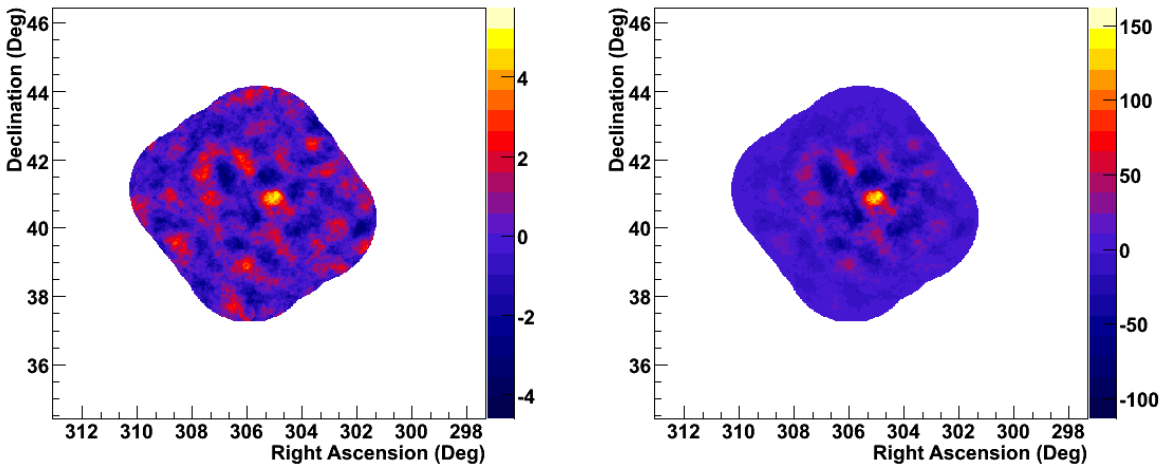

Figure 5.27 The plot of the excess counts (left) and the Ring Background Model-derived significance (right) for γ Cygni for a size cut >600 digital counts.

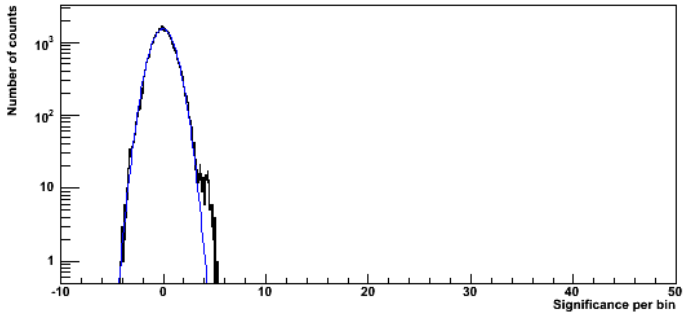

Figure 5.28 The plot of the distribution of significances in the γ Cygni field of view. The distribution is highly suggestive of a source in the field of view, as it shows extension beyond the normal distribution (blue line) in positive significance. A matching extension in the negative significances would likely indicate some systematic effect, but none is seen.

Remnant	Livetime (min)	θ^2	σ_{pre}	σ_{post}	Upper Limit	Flux	$\frac{F}{F_{Crab}}$
G67.7+1.8	715.9	0.014	-0.45	—	1.74	—	0.012
G68.6-1.2	442.1	0.014	1.50	0.56	3.63	—	0.027
G69.0+2.7 (CTB 80)	763.1	0.055	-0.99	—	1.61	—	0.012
G69.7+1.0	632.2	0.014	-0.21	—	2.11	—	0.016
G73.9+0.9	609.1	0.014	0.04	0.00	2.33	—	0.017
G74.9+1.2 (CTB 87)	552.4	0.014	1.57	1.23	6.69	—	0.050
G76.9+1.0	723.1	0.014	-1.40	—	1.57	—	0.012
G78.2+2.1 (γ Cygni SNR)	1095.8	0.055	5.26	4.82	6.15	4.46	0.046

Table 5.3 A summary of the results for all of the Cygnus region remnants for Survey-optimised cuts and dc >600. Upper limits at the 99% confidence level are given for remnants with no detection (σ <5). Both fluxes and upper limits are given in units of $10^{-12}\gamma$ cm^{-2} s^{-1}.

Remnant	Livetime (min)	θ^2	σ_{pre}	σ_{post}	Upper Limit	Flux	$\frac{F}{F_{Crab}}$
G67.7+1.8	715.9	0.014	0.81	0.14	0.63	—	0.023
G68.6-1.2	442.1	0.014	-0.32	—	0.55	—	0.020
G69.0+2.7 (CTB 80)	763.1	0.055	0.016	0.00	0.49	—	0.018
G69.7+1.0	632.2	0.014	1.46	0.73	0.81	—	0.030
G73.9+0.9	609.1	0.014	-0.77	—	0.39	—	0.015
G74.9+1.2 (CTB 87)	552.4	0.014	2.22	1.92	1.19	—	0.044
G76.9+1.0	723.1	0.014	-0.36	—	0.47	—	0.017
G78.2+2.1 (γ Cygni)	1311.58	0.055	3.83	3.23	1.07	—	0.040

Table 5.4 A summary of the results for all of the Cygnus region remnants for Survey-optimised cuts and dc >1000. Upper limits at the 99% confidence level are given for remnants with no detection (σ <5). Both fluxes and upper limits are given in units of $10^{-12}\gamma$ cm^{-2} s^{-1}.

CHAPTER 6

DISCUSSION

No new detections of VHE gamma-rays were made by our analyses from any of the remnants observed by VERITAS. In this chapter, we compare the resulting new upper limits on VHE gamma-ray emission in terms of both basic leptonic and hadronic models of emission. In addition, we summarize the conclusions drawn based on these models, and explore possible future directions for these studies.

6.1 Emission Models

The modeling of supernova shock properties and production of cosmic rays is a well-developed field, and a full treatment is well beyond the scope of this work. However, it is important to consider the implications of the limits set in this work with respect to these models. While a single upper limit is insufficient to carry out any meaningful fitting of spectral models in either the hadronic or leptonic cases, we can potentially constrain these models by their predicted flux above 300 MeV. We then discuss this constraint in terms of the evolutionary stage of the SNR for the constraining cases. What follows is a review of relavent models.

6.1.1 Hadronic Model

To fully model the acceleration of hadronic cosmic rays in SNR requires detailed hydrodynamic simulations. As an alternative, relatively simple models parameterize the efficiency of cosmic ray acceleration for the entire remnant and consider the overall production rates of VHE gamma rays. These relatively simple models stand in good agreement (to within a factor of 2 or so in the worst cases) with more detailed hydrodynamic models of VHE gamma-ray production by shock accelerated cosmic rays (Kang and Drury 1992). Given the inherent uncertainty in the underlying parameters of the SNR which feed into these models, this is considered an acceptable trade-off considering the complexity of the full hydrodynamic

treatment. For this work, we follow the methodology of Buckley et al. (1998) in estimating the key parameters n, d and E_{SN} for each remnant and using them to compare the fluxes predicted by the method of Drury et al. (1994) as discussed in 1.5.4. Rather than estimate the particle acceleration efficiency Θ based on the required efficiency to account for the cosmic ray energy density, we keep it as our limitable quantity.

6.1.2 Leptonic Model

The basic leptonic model for VHE gamma-ray emission is that of a single population of relativistic electrons upscattering lower energy photons. The source of these photons may be the cosmic microwave background (CMB), starlight, or synchrotron or infrared emission from the remnant itself. For this work, we follow primarily the approximations of [Schlickeiser 2002] and [Petruk 2009]. In the Thomson limit, where $\epsilon \ll E_e$, the power emitted by a "single" electron is given by

$$p_{mT} = \frac{4}{3} c \sigma_T U_{ph} \gamma^2 \tag{6.1}$$

where U_{ph} is the ambient photon energy density. For the purpose of this work, we consider only the CMB contribution to the energy density. This is not an unreasonable assumption for two reasons. First, multiple works ([Yukawa 2008], [de Jager and Mastichiadis 1997]) have shown that the photon energy density of starlight and local IR are, at most, comparable to that of the CMB. Secondly, for photons above $\sim 10^{-2}$ eV being scattered up to TeV energies, the Thomson cross section is no longer applicable and the Klein-Nishina cross section must be employed. This effectively reduces the scattering rate for higher energy photons relative to lower energy photons.

For a single-electron IC spectrum, emission is strongly peaked at a characteristic photon energy $E_{m\gamma}$. Numerical solutions and analytic approximations (Petruk

2009) show that in the Thomson limit ($\epsilon \ll \gamma m_e c^2$) this characteristic energy is given by

$$E_{m\gamma} \approx 4\epsilon_c \gamma^2 \tag{6.2}$$

where $\epsilon_c = kT_{ph}$. For the CMB, $\epsilon_c = 2.348 \times 10^{-4}$ eV. We estimate the full IC power of a single electron as being emitted monochromatically at $E_{m\gamma}$. We account only for emission energies within VERITAS's energy range of 300 GeV $<E_\gamma <$50 TeV. This corresponds to an underlying electron energy range of roughly 10 TeV $<E_e <$120 TeV.

Extracting an IC spectrum generally requires some assumption about the underlying electron spectrum. Typically, one assumes a spectrum of the form

$$\frac{dN}{dE} = N_o E^{-p}\ \mathrm{e}^{E/E_{max}} \tag{6.3}$$

In our case, remnants detected in the TeV regime typically have a spectrum which is well-matched to a single power law of spectral index 2.3 $<\Gamma <$2.8. Since, for a pure power law electron spectrum, the electron energy spectral index p is related to the photon spectral index Γ by

$$\Gamma = \frac{p-1}{2} \tag{6.4}$$

We will approximate our electron energy regime as following a (rapidly) falling power law of spectral index p = 6 in order to match a photon spectral index of $\Gamma = 2.5$. The total IC luminosity (or power) is given by:

$$P_{tot} = 4\pi d^2 = \int_{E_{min}}^{E_{max}} P E_e N_o E_e^{-p} dE_e \tag{6.5}$$

where

$$\int_{E_{min}}^{E_{max}} N_o E_e^{-p} dE_e \tag{6.6}$$

Results for maximum total energy 10 TeV <E_e <120 TeV in relativistic electrons of energy is given in Table 6.2, as well as upper limits on the energy density in these electrons within the remnant. Note that these limits assume that the relativistic electrons are distributed across the entire volume of the remnant. More restrictive emitting volumes will result in larger upper limits to n_e and U_e

6.2 Comparison with Results

6.2.1 Upper Limits

For this work, the upper limits are compared against both the basic hadronic observational model laid out by Drury et al. (1994) and a simplified one-zone leptonic model for IC emission in order to place limits on 1) the hadronic cosmic ray particle acceleration efficiency Θ and 2) the TeV electron energy density. The best available numbers for the relevant physical parameters, as given in Table 1.1, are used to calculate the volume and dimensionless quantity A for each remnant. In most cases, the explosion energy E_{SN} is poorly constrained, and so the canonical value of 10^{51} ergs, or 1 *Bethe*, is used. Since the environment of supernova remnants is often complex, the ambient density n_H typically varies around the remnant. Thus, A is calculated for $n_H = 1$ cm^{-2}, except where average values are available from the literature. Where there is a large uncertainty in the distance to the remnant, A is calculated for maximum distances. It should be noted that the constraints are strongly dependent on the values used and therefore as our understanding of these remnants changes, so will these constraints.

Typical values for Θ are $\sim 0.1 - 0.3$, both from SNR models and extrapolation from Galactic cosmic-ray energy densities. This value remains roughly constant throughout the remnant's Sedov phase and largely independent of the ambient density. Θ tends to be much lower during the free expansion phase, as very little energy is processed through the shocks at this point [Markiewicz et al. 1990].

W44

Remnant	F_{UL} ($cm^{-2}s^{-1}$)	A	Θ_{max}
CTB109 (G109.1-1.0)	8.83×10^{-12}	0.10	0.97
Tycho (G120.1+1.4)	1.00×10^{-12}	0.41	0.035
W44 (G34.7-0.4)	2.61×10^{-12}	0.82	0.036
G67.7+1.8	1.74×10^{-12}	0.086	0.22
G68.6-1.2	3.63×10^{-12}	0.015	1.0
CTB 80 (G69.0+2.7)	1.61×10^{-12}	0.25	0.071
G69.7+1.0	2.11×10^{-12}	4.8×10^{-3}	1.0
G73.9+0.9	2.33×10^{-12}	0.32	0.080
CTB87 (G74.9+1.2)	6.69×10^{-12}	0.027	1.0
G76.9+1.0	1.57×10^{-12}	6.3×10^{-3}	1.0
γ Cygni (G78.2+2.1)	6.15×10^{-12}	0.49	0.14

Table 6.1 This table gives a summary of some of the derivable limits to the hadronic acceleration efficiency of the remnants covered in this work which have not been detected. Where a large uncertainty exists in the distance to the SNR, the maximum distance value reported is used in calculating the term A.

Remnant	F_{UL} (cm^{-2} s^{-1})	E_{total}
CTB109 (G109.1-1.0)	8.83×10^{-12}	2.4×10^{25}
Tycho (G120.1+1.4)	1.00×10^{-12}	1.6×10^{23}
W44 (G34.7-0.4)	2.61×10^{-12}	4.5×10^{23}
G67.7+1.8	1.74×10^{-12}	6.8×10^{24}
G68.6-1.2	3.63×10^{-12}	4.7×10^{24}
CTB 80 (G69.0+2.7)	1.61×10^{-12}	1.3×10^{23}
G69.7+1.0	2.11×10^{-12}	8.7×10^{24}
G73.9+0.9	2.33×10^{-12}	7.3×10^{22}
CTB87 (G74.9+1.2)	6.69×10^{-12}	6.6×10^{24}
G76.9+1.0	1.57×10^{-12}	5.0×10^{24}
γ Cygni (G78.2+2.1)	6.15×10^{-12}	2.8×10^{23}

Table 6.2 This table gives a summary of some of the derivable limits to the relativistic electron populations of the remnants covered in this work which have not been detected. The total electron energy is given for electrons of energies $10 \leq E_e \leq 120$ TeV, which would emit photons in the VERITAS waveband.

Determining the presence of either leptonic or hadronic cosmic ray acceleration in W44 has been the goal of multiple studies. de Jager and Mastichiadis (1997) propose that the electron population seen in nonthermal X-ray emission can be accounted for by injection by the central pulsar of relativistic electrons into the surrounding remnant, and subsequent IC scattering on infrared photons. This was to primarily account for the gamma-ray emission seen by EGRET as the source 3EG J1856+0114, which is only tentatively associated with W44. This data yielded a shallow gamma-ray spectrum largely unconstrained by the earlier Whipple limits set on TeV emission ($F(>250\text{ GeV}) = 8.5 \times 10^{-11}\text{cm}^{-2}\text{s}^{-1}$). The pulsar-injection model is supported by our much lower limit on the TeV emission from W44/3EG J1856+0114. de Jager and Mastichiadis (1997) also find that the theoretical flux from hadronic emission based on the physical properties of the remnant are unable to account for the EGRET flux. Our flux limit constrains the hadronic efficiency well below even the 10% used to achieve their underestimate, thus supporting the claim that W44/3EG J1856+0114's gamma-ray emission is not likely to be the result of hadronic processes.

Tycho

Chandra observations have provided indirect evidence of acceleration of both cosmic-ray ions and electrons based on the energetics revealed by the shock geometry and emission (Warren et al. 2005). Thus, Tycho is a potential case where the contribution from both TeV components might be separable based on the remnant dynamics, since acceleration of electrons and hadrons would remove energy from the remnant with different efficiencies.

We constrain the hadronic cosmic ray efficiency for Tycho $\Theta \lesssim 0.035$. While this is significantly below the expected value over the entire lifetime of an average supernova remnant, it is not unexpected given that Tycho is a relatively young remnant (437 years) possibly still in the transition between the free expansion and Taylor-Sedov phases.

γ Cygni

Assuming an association, a naïve extrapolation of the gamma-ray spectrum of the unidentified EGRET source 3EG J2020+4017 predicts a VHE flux of $F(>$ 300 GeV$) = 2.1 \times 10^{-10}\mathrm{cm}^{-2}\mathrm{s}^{-1}$, roughly two orders of magnitude above the limits set in this work. This is not surprising, as the EGRET data suggests a spectral break at $\gtrsim 4$ GeV (Merck et al. 1996). This supports an at least primarily leptonic origin for the gamma-ray emission, as the simple hadronic model predicts a continuous emission spectrum out to higher energies, while a leptonic model allows for some cutoff energy.

For a purely hadronic origin for the (potential) emission from γ Cygni, our upper limit on the VHE gamma-ray flux constrains the cosmic ray efficiency to $\Theta \lesssim 0.14$. If we treat the signal as though it were a detection, then $\Theta \sim 0.10$, in very good agreement with the predictions for a middle-aged remnant somewhere between its adiabatic and radiative phases. Even treated as a detection, however, without more detailed spatial information we can make no distinction between the leptonic and hadronic case for γ Cygni.

Other Remnants

The maximum particle acceleration efficiency for a purely hadronic scenario is given as Θ_{max} for each remnant in Table 6.1. Of the remaining remnants, only 3 are meaningfully constrained in terms of hadronic cosmic-ray acceleration efficiency: G67.7+1.8, G73.9+0.9 and CTB 80. In all three cases, the values are near or above the naïvely expected values of 0.1-0.2. For CTB 80 and G73.9+0.9, the constraints are not surprising given the relative proximity of the objects. However, G67.7+1.8 has a very poorly constrained distance; for this work we have used d = 14 kpc, but reported values range from 7 - 17 kpc. If G67.7+1.8 is indeed much closer, then our maximum value for Θ will decrease considerably.

6.2.2 Detections

In the case of specific detections, more sophisticated models are appropriate given the level of detail which can be extracted; both Caseiopeia A ([Vink and Laming 2003], [Berezhko and Völk 2004]) and the Crab Nebula ([de Jager and Harding 1992], [Arons and Tavani 1994], [Celik 2008]) are handled in more detail as TeV emitters in other works. Since our confirmations are in good agreement with existing values, we leave these cases as proof of concept for our analyses. Further, neither of these remnants are good examples of potential TeV emission due to hadronic interactions. As a PWN, the Crab Nebula's emission is likely powered by synchrotron self-comptonization by electrons accelerated by the pulsar's magnetic field. In the case of Cas A, evidence from non-thermal X-ray emission indicates a definite strong leptonic component to the TeV emission. Also, the remnant's relatively young age ($\sim$ 320 years) means that the remnant is likely in its free expansion or very early Sedov phase, when hadronic acceleration is not at its maximum.

6.3 Conclusions

Five supernova remnants were observed between (2006-2008) by VERITAS as part of the Supernova Remnant Key Science Project. We have analyzed this data with the custom VEGAS software package. Of these, the two known TeV remnants- Cassiopeia A and the Crab Nebula - both yielded detections and spectra in good agreement with established values in our analyses. Further, we have met the accepted values for the official analyses of VERITAS' sensitivity. The remaining remnants- W44, CTB 109 and Tycho's SNR- were not detected. We have established upper limits on each of their fluxes of

$$F_{W44}(> 300 \text{ GeV}) = 2.6 \times 10^{-12}\gamma \text{ cm}^{-2} \text{ s}^{-1}$$

$$F_{CTB109}(> 300 \text{ GeV}) = 8.8 \times 10^{-12}\gamma \text{ cm}^{-2} \text{ s}^{-1}$$

$$F_{Tycho}(> 300 \text{ GeV}) = 1.0 \times 10^{-12}\gamma \text{ cm}^{-2} \text{ s}^{-1}$$

In addition, eight remnants were observed by VERITAS as part of the Cygnus Region Sky Survey. None of these remnants were detected with our analyses. We have set flux limits above 300 GeV on each of these remnants of $\sim 1-5\%$ of the Crab Nebula flux. The remnant γ Cygni appears as a likely VHE gamma-ray emitter with a significance of 4.8 σ, just below the official threshhold of detection of 5 σ. The newly established upper limits for these sources are

$$F_{G67.7+1.8}(> 300 \text{ GeV}) = 1.74 \times 10^{-12}\gamma \text{ cm}^{-2} \text{ s}^{-1}$$

$$F_{G68.6-1.2}(> 300 \text{ GeV}) = 3.63 \times 10^{-12}\gamma \text{ cm}^{-2} \text{ s}^{-1}$$

$$F_{CTB80}(> 300 \text{ GeV}) = 1.61 \times 10^{-12}\gamma \text{ cm}^{-2} \text{ s}^{-1}$$

$$F_{G69.7+1.0}(> 300 \text{ GeV}) = 2.11 \times 10^{-12}\gamma \text{ cm}^{-2} \text{ s}^{-1}$$

$$F_{G73.9+0.9}(> 300 \text{ GeV}) = 2.33 \times 10^{-12}\gamma \text{ cm}^{-2} \text{ s}^{-1}$$

$$F_{CTB87}(> 300 \text{ GeV}) = 6.69 \times 10^{-12}\gamma \text{ cm}^{-2} \text{ s}^{-1}$$

$$F_{G76.9+1.0}(> 300 \text{ GeV}) = 1.57 \times 10^{-12}\gamma \text{ cm}^{-2} \text{ s}^{-1}$$

$$F_{\gamma Cygni}(> 300 \text{ GeV}) = 6.15 \times 10^{-12}\gamma \text{ cm}^{-2} \text{ s}^{-1}$$

Each of these upper limits was compared to basic hadronic and leptonic models of VHE gamma-ray production in order to potentially constrain the efficiency of production of relativistic electrons and/or hadrons. Of these, Tycho and W44 in particular provided interesting limits. The limit on W44 seems to support the electron injection model proposed by de Jager and Mastichiadis (1997), and constrains the production of hadronic cosmic rays below the theoretical predictions for SNR shells. The relatively low limit on Tycho is somewhat surprising, given indirect evidence for cosmic ray acceleration based on remnant dynamics. However, given the relatively young age for Tycho it should be expected that the remnant has not yet reached its peak cosmic ray acceleration efficiency.

6.4 Future Work

The investigation into SNR as cosmic ray accelerators is a long-standing one, with leads in several different observational fields. In the our specific case, two major directions for future work suggest themselves: extension of existing observations, and the addition of multiwavelength data to our analyses.

6.4.1 Further Observations with VERITAS

On this specific project, deeper observations on the more promising targets- in particular, γ Cygni- could yield detections of TeV emission. A statistically significant detection of γ Cygni would allow for spectral reconstruction as well as studies of the morphology of the source at different energies. Studies of the morphology of the remnant are only viable in remnants with radii above $\sim 0.1^{\circ}$. In these extended remnants (like γ Cygni), the potential exists to localize the TeV emission. Spatial correlation of VHE emission could indicate the source of said emission; VHE emission located near a known population of electrons or pulsar wind nebula is probably leptonic in origin, while VHE emission localized on a nearby molecular cloud may be due to collisons by remnant-accelerated hadrons.

Alternately, a deeper exposure of one of the better-studied non-detections (e.g., Tycho or W44) would allow us to set more meaningful constraints on the correlation between VHE gamma-ray emission and other observed properties such as shock depth and the excitation of electron populations. This would likely require analysis of data from X-ray and GeV gamma-ray instruments.

6.4.2 Multiwavelength Observations

In the case of leptonic modeling in particular, the assemblage of a broad-band spectral energy distribution (SED) is especially useful. Simultaneous fitting of synchrotron, bremmstrahlung and inverse Compton spectra can more successfully constrain the electron energy distribution and ambient magnetic fields. For many of the remnants presented here, further observations would be required in radio and

X-ray before a meaningful SED could be assembled. For the more extensively observed remnants, however, constructing an SED would predominantly be an issue of assembling and analyzing existing data from a number of different experiments.

The high energy gamma-ray regime covered by the new Fermi LAT instrument (30 MeV - 300 GeV) is of particular interest in discerning the origin of VHE gamma rays from SNR, in part because it dovetails well with the capabilities of ground-based instruments like VERITAS. Spectral modeling indicates that hadronic and leptonic processes create a very different spectral shape in this energy regime. Thus, the combination of this lower energy gamma-ray data with even upper limits in the VHE band may ultimately distinguish between leptonic and hadronic emission and provide the "smoking gun" for cosmic ray acceleration in supernova remnants.

APPENDICES

Appendix A

DATA LIST

This appendix will lay out the observational data used in this work. Each table for the individual objects includes the Date, run number, laser calibration run number, the start-of-run time (UTC), usable duration, Offset from source, Azimuth and Elevation, the L3 triggering rate and the array trigger configuration for each run. For the Sky Survey data, a full data list is included with the above data and the Sky Survey pointing number each run is associated with. Table A.7 gives the analyses for each object that a given run was used in.

A.1 Targeted Remnants

Table A.1 Crab Nebula runlist

Date	Run	Laser	UTC	Dur. (min.)	Offset	Sky	L3 Rate (Hz)	Tel.
20071010	37009	37008	11:27	20	0.5E	B	247	2/1234
20071011	37039	37034	11:05	20	0.5W	A	260	2/1234
20071014	37195	37177	11:55	20	0.5S	A	255	2/1234
20071016	37266	37263	11:51	20	0.5W	A	239	2/1234
20071017	37297	37296	11:46	20	0.5S	A	240	2/1234
20071114	37946	37955	08:22	20	0.5S	A	257	2/1234
20071114	37947	37955	08:43	20	0.5E	A	261	2/1234
20071114	37948	37955	09:05	20	0.5W	A	262	2/1234
20071114	37949	37955	09:26	20	0.5N	A	264	2/1234
20071114	37950	37955	09:48	20	0.5S	A	264	2/1234
20071118	38063	38076	07:57	20	0.5E	A	257	2/1234
20071118	38064	38076	08:18	20	0.5W	A	253	2/1234
20071204	38200	38186	07:44	20	0.5E	A	247	2/1234

Date	Run	Laser	UTC	Dur. (min.)	Offset	Sky	L3 Rate (Hz)	Tel.
20071206	38273	38267	07:35	20	0.5W	A	269	2/1234
20071215	38405	38393	06:54	20	0.5S	A-	262	2/1234
20071230	38523	38508	06:02	20	0.5N	A	261	2/1234
20080112	38764	38786	06:11	20	0.5W	A	243	2/1234
20080130	38957	38950	04:06	20	0.5E	A	254	2/1234
20080130	38958	38950	04:27	20	0.5W	A	253	2/1234
20080202	39035	39053	03:13	20	0.5N	A-	252	2/1234
20080203	39072	39053	03:58	20	0.5S	A	250	2/1234
20080206	39109	39132	03:45	20	0.5W	A	256	2/1234

Table A.2 Cassiopeia A runlist

Date	Run	Laser	UTC	Dur. (min.)	Offset	Sky	L3 Rate (Hz)	Tel.
20070911	36271	36286	07:48	20	0.5N	B-	134	2/1234
20070911	36272	36286	08:12	20	0.5S	B-	135	2/1234
20070918	36546	36533	08:32	20	0.5N	B+	241	2/1234
20070918	36547	36533	08:56	20	0.5S	B+	238	2/1234
20070918	36548	36533	09:18	20	0.5E	B+	232	2/1234
20070918	36549	36533	09:40	20	0.5W	B+	226	2/1234
20070919	36592	36601	08:38	20	0.5N	B	225	2/1234
20070920	36626	36601	08:29	20	0.5S	B	244	2/1234
20070920	36627	36601	08:51	20	0.5N	B	243	2/1234
20070920	36628	36601	09:12	20	0.5W	B	240	2/1234
20071007	36850	36858	07:05	20	0.5E	B	240	2/1234

Date	Run	Laser	UTC	Dur. (min.)	Offset	Sky	L3 Rate (Hz)	Tel.
20071007	36851	36858	07:26	20	0.5W	B	240	2/1234
20071007	36852	36858	07:49	20	0.5N	B	240	2/1234
20071011	37024	37034	06:06	20	0.5E	A	250	2/1234
20071011	37025	37034	06:28	20	0.5W	A	247	2/1234
20071011	37026	37034	06:49	20	0.5S	A	247	2/1234
20071011	37027	37034	07:10	20	0.5N	A	242	2/1234
20071011	37028	37034	07:31	20	0.5E	A	240	2/1234
20071011	37029	37034	07:52	20	0.5W	A	233	2/1234
20071013	37114	37148	06:49	20	0.5S	A	227	2/1234
20071013	37115	37148	07:10	20	0.5E	A	224	2/1234
20071013	37116	37148	07:31	20	0.5W	A	224	2/1234
20071013	37117	37148	07:52	20	0.5S	A	220	2/1234
20071014	37169	37177	06:50	20	0.5N	A	234	2/1234
20071014	37170	37177	07:11	20	0.5S	A	231	2/1234
20071014	37171	37177	07:33	20	0.5W	A	225	2/1234
20071014	37172	37177	07:55	20	0.5E	A	222	2/1234
20071015	37214	37228	06:42	20	0.5N	A	237	2/1234
20071015	37215	37228	07:04	20	0.5S	A	234	2/1234
20071015	37216	37228	07:25	20	0.5W	A	228	2/1234
20071015	37217	37228	07:48	20	0.5E	A	225	2/1234
20071016	37245	37263	06:45	20	0.5W	A	227	2/1234
20071016	37246	37263	07:20	20	0.5E	A	224	2/1234
20071016	37247	37263	07:44	20	0.5S	A	217	2/1234
20071017	37282	37296	06:16	20	0.5N	A	232	2/1234
20071017	37283	37296	06:41	20	0.5E	A	227	2/1234
20071017	37284	37296	07:02	20	0.5W	A	221	2/1234

Date	Run	Laser	UTC	Dur. (min.)	Offset	Sky	L3 Rate (Hz)	Tel.
20071017	37285	37296	07:23	20	0.5S	A	217	2/1234
20071017	37286	37296	07:48	20	0.5N	A	212	2/1234
20071019	37385	37415	03:29	20	0.5N	A	116	2/1234
20071019	37386	37415	03:51	20	0.5S	A	118	2/1234
20071019	37387	37415	04:15	20	0.5E	A	119	2/1234
20071031	37489	37493	03:40	20	0.5N	B	245	2/1234
20071031	37490	37493	04:01	20	0.5S	B	241	2/1234
20071031	37491	37493	04:22	20	0.5E	B	230	2/1234
20071101	37505	37510	04:01	20	0.5N	C	248	2/1234
20071101	37506	37510	04:23	18	0.5S	B	248	2/1234
20071102	37521	37530	03:37	20	0.5E	A	246	2/1234
20071102	37522	37530	03:59	20	0.5W	A	249	2/1234
20071102	37523	37530	04:22	20	0.5N	A	247	2/1234
20071102	37524	37530	04:44	20	0.5S	A	245	2/1234
20071103	37549	37557	03:55	20	0.5W	A	250	2/1234
20071103	37550	37557	04:16	20	0.5E	A	249	2/1234
20071103	37551	37557	04:37	20	0.5N	A	246	2/1234
20071103	37552	37557	04:58	20	0.5S	A	245	2/1234
20071104	37578	37590	03:21	20	0.5E	A	228	2/1234
20071104	37579	37590	03:42	20	0.5W	A	232	2/1234
20071104	37580	37590	04:03	20	0.5N	A	233	2/1234
20071104	37581	37590	04:24	20	0.5S	A	235	2/1234
20071104	37582	37590	04:45	20	0.5E	A	232	2/1234
20071105	37612	37623	03:17	20	0.5W	A	236	2/1234
20071105	37613	37623	03:39	20	0.5N	A	234	2/1234
20071105	37614	37623	04:00	20	0.5S	A	233	2/1234

Date	Run	Laser	UTC	Dur. (min.)	Offset	Sky	L3 Rate (Hz)	Tel.
20071105	37615	37623	04:22	20	0.5E	A	230	2/1234
20071105	37616	37623	04:43	20	0.5W	A	231	2/1234
20071105	37617	37623	05:04	20	0.5N	A	226	2/1234
20071106	37653	37694	04:48	20	0.5S	B-	235	2/1234
20071106	37654	37694	05:10	20	0.5E	B-	232	2/1234
20071106	37655	37694	05:32	20	0.5W	B-	226	2/1234
20071106	37656	37694	05:54	20	0.5N	B-	225	2/1234
20071106	37657	37694	06:15	20	0.5S	B-	223	2/1234
20071109	37758	37780	05:00	20	0.5E	A	235	2/1234
20071109	37759	37780	05:21	20	0.5W	A	229	2/1234
20071111	37824	37845	04:58	20	0.5N	A	234	2/1234
20071111	37825	37845	05:20	20	0.5S	A	236	2/1234
20071112	37861	37868	03:16	20	0.5E	A	241	2/1234
20071112	37862	37868	03:38	20	0.5W	A	241	2/1234
20071112	37863	37868	03:59	20	0.5N	A	238	2/1234
20071112	37864	37868	04:26	20	0.5S	A	237	2/1234
20071112	37865	37868	04:48	20	0.5E	A	233	2/1234

Table A.3 Tycho runlist

Date	Run	Laser	UTC	Dur. (min.)	Offset	Sky	L3 Rate (Hz)	Tel.
20081022	42302	42215	05:13	20	0.5N	A	227	2/1234
20081022	42303	42215	05:35	20	0.5S	A	228	2/1234
20081022	42304	42215	05:56	20	0.5E	A	227	2/1234
20081022	42305	42215	06:17	20	0.5W	A	227	2/1234

Date	Run	Laser	UTC	Dur. (min.)	Offset	Sky	L3 Rate (Hz)	Tel.
20081022	42306	42215	06:38	20	0.5N	A	225	2/1234
20081022	42307	42215	06:59	20	0.5S	A	223	2/1234
20081023	42354	42346	06:46	20	0.5E	A	214	2/1234
20081023	42355	42346	07:07	20	0.5W	A	211	2/1234
20081025	42428	42433	06:13	20	0.5N	A	225	2/1234
20081025	42429	42433	06:34	20	0.5S	A	223	2/1234
20081025	42430	42433	06:55	20	0.5E	A	222	2/1234
20081025	42431	42433	07:17	20	0.5W	A	220	2/1234
20081026	42464	42460	06:29	20	0.5N	A	202	2/1234
20081026	42469	42460	07:22	20	0.5S	A	195	2/1234
20081028	42534	42547	04:45	20	0.5N	A	219	2/1234
20081028	42535	42547	05:07	20	0.5S	A	220	2/1234
20081028	42536	42547	05:28	20	0.5E	A	216	2/1234
20081028	42537	42547	05:51	20	0.5W	A	217	2/1234
20081029	42582	42594	05:32	20	0.5N	A	207	2/1234
20081029	42583	42594	05:53	20	0.5S	A	206	2/1234
20081029	42584	42594	06:15	20	0.5E	A	203	2/1234
20081029	42585	42594	06:35	20	0.5W	A	202	2/1234
20081030	42615	42635	05:04	20	0.5N	B+	192	2/1234
20081030	42616	42635	05:26	20	0.5S	B+	191	2/1234
20081030	42617	42635	05:47	20	0.5E	B+	190	2/1234
20081030	42618	42635	06:08	20	0.5W	B+	189	2/1234
20081030	42619	42635	06:30	20	0.5N	B+	186	2/1234
20081031	42654	42666	05:45	20	0.5N	B-	196	2/1234
20081031	42655	42666	06:06	20	0.5S	B+	193	2/1234
20081031	42656	42666	06:27	20	0.5E	B+	190	2/1234

Date	Run	Laser	UTC	Dur. (min.)	Offset	Sky	L3 Rate (Hz)	Tel.
20081031	42657	42666	06:48	20	0.5W	B+	187	2/1234
20081031	42658	42666	07:10	20	0.5S	B+	184	2/1234
20081031	42659	42666	07:30	20	0.5E	B+	181	2/1234
20081101	42687	42696	04:15	20	0.5W	B+	189	2/1234
20081101	42688	42696	04:35	20	0.5N	B+	191	2/1234
20081101	42689	42696	04:57	20	0.5S	B+	193	2/1234
20081103	42763	42780	05:53	20	0.5E	B	121	2/123-
20081103	42764	42780	06:15	20	0.5W	B	120	2/123-
20081103	42765	42780	06:36	20	0.5N	B	119	2/123-
20081104	42792	42799	05:14	20	0.5S	A	210	2/1234
20081104	42794	42799	05:57	20	0.5W	A	204	2/1234
20081118	43034	42981	04:30	20	0.5S	A	222	2/1234
20081120	43121	43127	05:14	20	0.5E	A	213	2/1234
20081120	43122	43127	05:36	20	0.5W	A	211	2/1234
20081124	43245	43163	04:18	20	0.5N	A	209	2/1234
20081124	43246	43163	04:39	20	0.5S	A	205	2/1234
20081124	43247	43163	05:00	20	0.5E	A	202	2/1234
20081124	43248	43163	05:21	20	0.5W	A	200	2/1234
20081201	43353	43357	04:00	20	0.5N	A	220	2/1234
20081201	43354	43357	04:22	20	0.5S	A	216	2/1234
20081201	43355	43357	04:43	20	0.5E	A	214	2/1234
20081201	43356	43357	05:04	20	0.5W	A	211	2/1234
20081203	43424	43423	04:43	20	0.5N	B	214	2/1234
20081221	43641	43614	02:20	20	0.5N	A	223	2/1234
20081221	43642	43614	02:41	20	0.5S	A	219	2/1234
20081221	43643	43614	03:02	20	0.5E	A	218	2/1234

Date	Run	Laser	UTC	Dur. (min.)	Offset	Sky	L3 Rate (Hz)	Tel.
20081221	43644	43614	03:23	20	0.5W	A	216	2/1234
20081221	43645	43614	03:44	20	0.5N	A	213	2/1234
20081225	43711	43720	02:21	20	0.5N	B	220	2/1234
20081225	43712	43720	02:42	20	0.5S	B	215	2/1234
20081225	43713	43720	03:03	20	0.5E	B	214	2/1234
20081225	43714	43720	03:23	20	0.5W	B	210	2/1234
20081228	43725	43731	02:09	20	0.5N	A	223	2/1234
20081228	43726	43731	02:30	20	0.5S	A	217	2/1234
20090113	43974	43976	02:15	20	0.5E	A	218	2/1234
20090113	43975	43976	02:35	20	0.5W	A	208	2/1234
20090116	44003	44005	01:52	20	0.5E	A	205	2/1234
20090116	44004	44005	02:13	20	0.5W	A	202	2/1234
20090119	44075	44027	01:59	20	0.5E	C	185	2/1234

Table A.4 W44 runlist

Date	Run	Laser	UTC	Dur. (min.)	Offset	Sky	L3 Rate (Hz)	Tel.
20080507	40792	0	10:11	20	0.5N	A	186	2/1234
20080507	40793	0	10:32	20	0.5S	A	188	2/1234
20080507	40794	0	10:53	20	0.5E	A	192	2/1234
20080508	40812	0	10:22	20	0.5W	B	208	2/1234
20080508	40813	0	10:42	20	0.5N	B	209	2/1234
20080508	40814	0	11:03	20	0.5S	B	218	2/1234
20080513	40880	0	09:41	20	0.5E	A	187	2/1234
20080513	40881	0	10:06	20	0.5E	A	192	2/1234

Date	Run	Laser	UTC	Dur. (min.)	Offset	Sky	L3 Rate (Hz)	Tel.
20080513	40882	0	10:27	20	0.5W	A	192	2/1234
20080513	40883	0	10:48	20	0.5W	A	190	2/1234
20080602	41073	41072	07:53	20	0.5N	B	179	2/1234
20080602	41074	41072	08:14	20	0.5S	B	182	2/1234
20080602	41075	41072	08:35	20	0.5E	B	187	2/1234
20080602	41076	41072	08:56	20	0.5W	B	189	2/1234
20080602	41077	41072	09:17	20	0.5N	B	196	2/1234
20080602	41078	41072	09:38	20	0.5S	B	221	2/1234
20080602	41079	41072	09:59	20	0.5E	B	199	2/1234
20080603	41106	41098	09:53	20	0.5W	B+	189	2/1234
20080603	41107	41098	10:14	20	0.5N	B+	186	2/1234
20080603	41108	41098	10:35	20	0.5S	B+	182	2/1234
20080605	41154	41142	09:25	20	0.5E	A	210	2/1234
20080605	41156	41142	10:07	20	0.5W	A	197	2/1234
20080605	41157	41142	10:29	20	0.5N	A	190	2/1234
20080606	41173	41163	08:27	20	0.5N	A	212	2/1234
20080606	41174	41163	08:58	20	0.5S	A	216	2/1234v
20080606	41177	41163	10:03	20	0.5E	A	211	2/1234
20080606	41178	41163	10:24	20	0.5W	A	206	2/1234
20080607	41197	41222	08:10	20	0.5S	A	197	2/1234
20080607	41198	41222	08:31	20	0.5E	A	201	2/1234
20080607	41199	41222	09:08	20	0.5W	A	208	2/1234

Table A.5 CTB 109 runlist

Date	Run	Laser	UTC	Dur. (min.)	Offset	Sky	L3 Rate (Hz)	Tel.
20071204	38184	38186	02:06	20	0.5N	A	256	2/1234
20071205	38219	38186	02:09	20	0.5W	A	278	2/1234
20071205	38220	38186	02:31	20	0.5E	A	259	2/1234
20071206	38254	38267	02:09	20	0.5S	B+	140	2/1234
20071206	38256	38267	02:36	20	0.5N	A	258	2/1234
20071229	38496	38495	01:55	20	0.5E	B-	239	2/1234
20071229	38497	38495	02:17	20	0.5W	B-	235	2/1234
20071230	38509	38508	02:00	20	0.5N	B-	237	2/1234
20071230	38510	38508	02:22	20	0.5S	B-	236	2/1234
20071231	38529	38539	01:44	20	0.5E	A	239	2/1234
20071231	38530	38539	02:06	20	0.5W	A	232	2/1234
20071231	38531	38539	02:27	20	0.5N	A	226	2/1234
20080101	38550	38562	01:40	16	0.5S	A	246	2/1234
20080101	38552	38562	02:19	20	0.5E	A	228	2/1234
20080105	38616	38635	01:48	02	0.5N	B-	221	2/1234
20080110	38679	38685	01:52	20	0.5S	A	137	2/1234
20080110	38680	38685	02:14	20	0.5E	A	189	2/1234
20080111	38708	38731	02:04	20	0.5W	A	226	2/1234
20080112	38750	38786	02:01	20	0.5S	A	210	2/1234

A.2 Sky Survey

Table A.7 A full listing of all of the Sky Survey pointings completed as of December 2008.

Pointing #	RA (hrs)	Dec (deg)	Analyses
1	19.73	31.95	
2	19.80	31.47	CTB 80, G67.7+1.8
3	19.87	30.95	CTB 80, G67.7+1.8
4	19.93	30.43	G67.7+1.8
5	20.00	29.92	G67.7+1.8, G68.6-1.2
6	20.07	29.38	G68.6-1.2
7	19.77	32.65	CTB 80
8	19.83	32.15	CTB 80, G67.7+1.8
9	19.90	31.63	CTB 80, G67.7+1.8
10	19.97	31.12	G67.7+1.8 G69.7+1.0
11	20.03	30.60	G67.7+1.8, G68.6-1.2
12	20.10	30.07	G68.6-1.2
13	19.80	33.35	CTB 80
14	19.87	32.83	CTB 80, G67.7+1.8
15	19.93	32.32	CTB 80, G67.7+1.8, G69.7+1.0
16	20.00	31.80	CTB 80, G67.7+1.8, G69.7+1.0
17	20.07	31.27	G68.6-1.2, G69.7+1.0
18	20.13	30.73	G68.6-1.2
19	19.82	34.03	CTB 80
20	19.90	33.52	CTB 80, G69.7+1.0
21	19.97	33.00	CTB 80, G67.7+1.8, G69.7+1.0
22	20.03	32.48	CTB 80, G67.7+1.8, G69.7+1.0

Pointing	RA (hrs)	Dec (deg)	Analyses
23	20.10	31.95	G68.6-1.2
24	20.17	31.42	G68.6-1.2
25	19.85	34.72	CTB 80
26	19.93	34.22	CTB 80
27	20.00	33.68	CTB 80, G69.7+1.0
28	20.07	33.17	G69.7+1.0
29	20.13	32.62	G69.7+1.0
30	20.20	32.08	
31	19.88	35.40	
32	19.97	34.90	
33	20.03	34.37	G69.7+1.0
34	20.10	33.83	G69.7+1.0
35	20.17	33.30	G69.7+1.0
36	20.23	32.75	
37	19.92	36.10	
38	20.00	35.58	
39	20.07	35.05	
40	20.13	34.52	
41	20.20	33.97	
42	20.27	33.42	
43	19.95	36.78	
44	20.03	36.25	
45	20.10	35.72	G73.9+0.9
46	20.17	35.18	G73.9+0.9
47	20.23	34.63	G73.9+0.9
48	20.30	34.08	

Pointing	RA (hrs)	Dec (deg)	Analyses
49	20.00	37.47	
50	20.07	36.93	
51	20.13	36.40	CTB 87, G73.9+0.9
52	20.20	35.85	CTB 87, G73.9+0.9
53	20.27	35.80	CTB 87, G73.9+0.9
54	20.33	34.73	G73.9+0.9
55	20.03	38.13	
56	20.10	37.62	
57	20.17	37.07	CTB 87, G73.9+0.9
58	20.23	36.52	CTB 87, G73.9+0.9
59	20.30	35.97	CTB 87, G73.9+0.9
60	20.38	35.40	
61	20.07	38.82	
62	20.13	38.28	CTB 87
63	20.20	37.73	CTB 87, G73.9+0.9
64	20.28	37.18	CTB 87, G73.9+0.9, G76.9+1.0
65	20.35	36.62	CTB 87, G73.9+0.9
66	20.42	36.05	
67	20.10	39.50	
68	20.17	38.95	
69	20.25	38.40	CTB 87, G76.9+1.0
70	20.32	37.85	CTB 87, G73.9+0.9, G76.9+1.0
71	20.38	37.28	CTB 87, G76.9+1.0
72	20.45	36.70	
73	20.13	40.17	
74	20.22	39.63	γ-Cygni

Pointing	RA (hrs)	Dec (deg)	Analyses
75	20.28	39.07	γ-Cygni, CTB 87, G76.9+1.0
76	20.35	38.50	γ-Cygni, CTB 87, G76.9+1.0
77	20.42	37.93	CTB 87, G76.9+1.0
78	20.48	37.35	G76.9+1.0
79			
80	20.25	40.30	γ-Cygni,
81	20.32	39.73	γ-Cygni, G76.9+1.0
82	20.38	39.17	γ-Cygni, G76.9+1.0
83	20.47	38.58	G76.9+1.0
84	20.52	38.00	G76.9+1.0
85			
86	20.28	40.95	γ-Cygni
87	20.37	40.38	γ-Cygni, G76.9+1.0
88	20.43	39.82	γ-Cygni, G76.9+1.0
89	20.50	39.23	G76.9+1.0
90	20.57	38.65	
91			
92	20.33	41.62	γ-Cygni
93	20.40	41.05	γ-Cygni
94			
95	20.55	39.88	
96	20.62	39.28	
97			
98	20.37	42.28	γ-Cygni
99	20.43	41.70	γ-Cygni
100	20.52	41.12	

Pointing	RA (hrs)	Dec (deg)	Analyses
101	20.58	40.52	
102	20.65	39.92	
103			
104	20.42	42.93	
105	20.48	42.35	
106	20.55	41.77	
107	20.63	41.17	
108	20.70	40.55	
109			
110	20.45	43.58	
111	20.53	43.00	
112	20.60	42.40	
113	20.67	41.80	
114	20.73	41.18	
115			
116	20.50	44.23	
117	20.57	43.65	
118	20.65	43.05	
119	20.72	42.43	
120	20.78	41.82	

Appendix B

BIAS ALIGNMENT

This appendix will describe the procedure for bias aligning the individual VERITAS telescopes using the laser calibration technique[Toner et al. 2008]. The intention of bias alignment is to overcome the telescope mirror's natural tendency to deform at different elevations. This deformation is largely the result of gravitational slumping. Thus, a telescope aligned perfectly at 0deg elevation (where the mirrors are most readily accessible) will be misaligned and have a measurably worse PSF at higher elevation. Since most VERITAS observations occur above 50° elevation, and telescope alignment occurs at 0°, bias alignment is crucial for this instrument. Typically, alignment is only necessary about once per year.

B.1 Equipment

The key instrument in bias alignment is a custom laser alignment system developed by the VERITAS group at NUI, Galway. The system (Figure B.1) consists of a laser and beam-splitter assembly mounted to a pan-tilt unit (PTU). The PTU is controlled by custom software on an attached laptop. Mounted behind the laser/splitter assembly is a translucent screen and a CCD camera. When trained on a mirror normal to the beam path, the laser light will return along its outgoing path, projecting a laser point at the same position as a backscattered portion of the original beam (the "reference beam").

B.2 Bias Measurement

The biases of each mirror are measured directly by temporarily mounting a laser onto each mirror. These lasers are pointed onto a screen placed over the plane of the camera. Measurements are made for a group of mirrors (typically six) by imaging the pattern of laser points on the screen with the Optical Monitoring CCD Camera. The telescope is moved from 0° up to 70° elevation, and then back down to 0°, with stills taken at each of the three stopping points. The biases of the

Figure B.1 The VERITAS alignment tool front (left) and rear (right) view.

mirrors are determined based on the movement of the laser points between 0° and 70°.

B.3 Bias Alignment

Once biases are calculated for each mirror, bias alignment can occur. The alignment system is mounted on an alignment tower located at twice the focal length (the "2f point) (Figure B.2) from the center of the reflector. The telescope is the slewed into the alignment position, such that the optical axis is aligned with the instrument. While this position is well-known for each telescope, difficulty in fine-positioning the telescopes at low elevation make this a non-trivial task.

Once the telescope is in position, the alignment laser is trained on the mirror to be aligned. The CCD camera takes an image of the screen, and the program finds the separation between the centroids of the reflected and reference beams. For gross alignment, a simple minimization of this separation is desired. For bias alignment, the measured biases are used by the program to determine the desired offset, and the mirror is moved to the appropriate misalignment.

Mirror adjustment is carried out by an individual or individuals at the reflector, usually in a bucketed manlift or cherry-picker. Using pole-mounted ratchet heads, the operators adjust the facet mounting bracket via the three adjustable

mounting screws as instructed by the alignment system operator. Once satisfactory bias alignment is achieved, the process is repeated for each mirror.

Figure B.2 Telescope 2 and its Alignment Tower, located at the "$2f$" point. Image taken from [Toner et al. 2008].

B.4 Improvements and Recent Innovations

Recently, a new technique for bias alignment for VERITAS has been developed by Andrew McCann at McGill University (McCann et al. 2009). Rather than relying on a reflected laser beam, this technique uses a bright star for calibration. A mirror is mounted at 45deg to the light path in front of the PMT camera and a CCD camera is mounted at the new focal point. A Raster-scan is then taken of a bright star at whatever elevation the telescope is to be aligned to (typically 60-70deg). A mirror in perfect alignment will reflect the star's light when the telescope is pointed directly at it, thus appearing bright in the CCD image. A misaligned mirror will appear dark at a 0deg offset, but will become bright as the telescope moves through

the offset matching the mirror's misalignment. By measuring the extent and direction of the offset, the misalignment can be determined, and corrected manually as in the laser technique. Early indications are that this method is at least as successful as the earlier technique and will be implemented in its stead.

BIBLIOGRAPHY

Abdo, A. A. 2007. Discovery of localized TeV gamma-ray sources and diffuse TeV gamma-ray emission from the galactic plane with Milagro using a new background rejection technique. Ph.D. thesis, Michigan State University.

Abdo, A. A., Allen, B. T., Aune, T., Berley, D., Chen, C., Christopher, G. E., DeYoung, T., Dingus, B. L., Ellsworth, R. W., Gonzalez, M. M., Goodman, J. A., Hays, E., Hoffman, C. M., Huentemeyer, P. H., Kolterman, B. E., Linnemann, J. T., McEnery, J. E., Morgan, T., Mincer, A. I., Nemethy, P., Pretz, J., Ryan, J. M., Saz Parkinson, P. M., Shoup, A., Sinnis, G., Smith, A. J., Vasileiou, V., Walker, G. P., Williams, D. A., and Yodh, G. B. 2009. Milagro Observations of Multi-TeV Emission from Galactic Sources in the Fermi Bright Source List. *ArXiv e-prints*.

Acciari, V. A., Aliu, E., Arlen, T., Beilicke, M., Benbow, W., Böttcher, M., Bradbury, S. M., Buckley, J. H., Bugaev, V., Butt, Y., Byrum, K., Cannon, A., Celik, O., Cesarini, A., Chow, Y. C., Ciupik, L., Cogan, P., Cui, W., Daniel, M. K., Dickherber, R., Ergin, T., Falcone, A., Fegan, S. J., Finley, J. P., Fortin, P., Fortson, L., Furniss, A., Gall, D., Gibbs, K., Gillanders, G. H., Godambe, S., Grube, J., Guenette, R., Gyuk, G., Hanna, D., Hays, E., Holder, J., Horan, D., Hui, C. M., Humensky, T. B., Imran, A., Kaaret, P., Karlsson, N., Kertzman, M., Kieda, D., Kildea, J., Konopelko, A., Krawczynski, H., Krennrich, F., Lang, M. J., LeBohec, S., Maier, G., McCann, A., McCutcheon, M., Millis, J., Moriarty, P., Mukherjee, R., Nagai, T., Ong, R. A., Otte, A. N., Pandel, D., Perkins, J. S., Petry, D., Pizlo, F., Pohl, M., Quinn, J., Ragan, K., Reyes, L. C., Reynolds, P. T., Roache, E., Rose, H. J., Schroedter, M., Sembroski, G. H., Smith, A. W., Steele, D., Swordy, S. P., Theiling, M., Toner, J. A., Varlotta, A., Vassiliev, V. V., Wagner, R. G., Wakely, S. P., Ward, J. E., Weekes, T. C., Weinstein, A., Williams, D. A., Wissel, S., Wood, M., and Zitzer, B. 2009. Observations of Shell-type SNR Cassiopeia A at TeV Energies with VERITAS. IN REVIEW.

Aharonian, F., Akhperjanian, A., Barrio, J., Bernlöhr, K., Börst, H., Bojahr, H., Bolz, O., Contreras, J., Cortina, J., Denninghoff, S., Fonseca, V., Gonzalez, J., Götting, N., Heinzelmann, G., Hermann, G., Heusler, A., Hofmann, W., Horns, D., Ibarra, A., Iserlohe, C., Jung, I., Kankanyan, R., Kestel, M., Kettler, J., Kohnle, A., Konopelko, A., Kornmeyer, H., Kranich, D., Krawczynski, H., Lampeitl, H., Lopez, M., Lorenz, E., Lucarelli, F., Magnussen, N., Mang, O., Meyer, H., Mirzoyan, R., Moralejo, A., Ona, E., Padilla, L., Panter, M., Plaga, R., Plyasheshnikov,

A., Prahl, J., Pühlhofer, G., Rauterberg, G., Röhring, A., Rhode, W., Rowell, G. P., Sahakian, V., Samorski, M., Schilling, M., Schröder, F., Siems, M., Stamm, W., Tluczykont, M., Völk, H. J., Wiedner, C. A., and Wittek, W. 2001a. Evidence for TeV gamma ray emission from Cassiopeia A. *A&A 370*, 112–120.

Aharonian, F., Akhperjanian, A., Beilicke, M., Bernlöhr, K., Börst, H.-G., Bojahr, H., Bolz, O., Coarasa, T., Contreras, J., Cortina, J., Denninghoff, S., Fonseca, V., Girma, M., Götting, N., Heinzelmann, G., Hermann, G., Heusler, A., Hofmann, W., Horns, D., Jung, I., Kankanyan, R., Kestel, M., Kohnle, A., Konopelko, A., Kranich, D., Lampeitl, H., Lopez, M., Lorenz, E., Lucarelli, F., Mang, O., Mazin, D., Meyer, H., Mirzoyan, R., Moralejo, A., Oña-Wilhelmi, E., Panter, M., Plyasheshnikov, A., Pühlhofer, G., de los Reyes, R., Rhode, W., Ripken, J., Rowell, G. P., Sahakian, V., Samorski, M., Schilling, M., Siems, M., Sobzynska, D., Stamm, W., Tluczykont, M., Vitale, V., Völk, H. J., Wiedner, C. A., and Wittek, W. 2005. The unidentified TeV source (TeV J2032+4130) and surrounding field: Final HEGRA IACT-System results. *A&A 431*, 197–202.

Aharonian, F., Akhperjanian, A. G., Bazer-Bachi, A. R., Beilicke, M., Benbow, W., Berge, D., Bernlöhr, K., Boisson, C., Bolz, O., Borrel, V., Braun, I., Breitling, F., Brown, A. M., Bühler, R., Büsching, I., Carrigan, S., Chadwick, P. M., Chounet, L.-M., Cornils, R., Costamante, L., Degrange, B., Dickinson, H. J., Djannati-Ataï, A., O'C. Drury, L., Dubus, G., Egberts, K., Emmanoulopoulos, D., Espigat, P., Feinstein, F., Ferrero, E., Fiasson, A., Fontaine, G., Funk, S., Funk, S., Gallant, Y. A., Giebels, B., Glicenstein, J. F., Goret, P., Hadjichristidis, C., Hauser, D., Hauser, M., Heinzelmann, G., Henri, G., Hermann, G., Hinton, J. A., Hofmann, W., Holleran, M., Horns, D., Jacholkowska, A., de Jager, O. C., Khélifi, B., Komin, N., Konopelko, A., Kosack, K., Latham, I. J., Le Gallou, R., Lemière, A., Lemoine-Goumard, M., Lohse, T., Martin, J. M., Martineau-Huynh, O., Marcowith, A., Masterson, C., McComb, T. J. L., de Naurois, M., Nedbal, D., Nolan, S. J., Noutsos, A., Orford, K. J., Osborne, J. L., Ouchrif, M., Panter, M., Pelletier, G., Pita, S., Pühlhofer, G., Punch, M., Raubenheimer, B. C., Raue, M., Rayner, S. M., Reimer, A., Reimer, O., Ripken, J., Rob, L., Rolland, L., Rowell, G., Sahakian, V., Saugé, L., Schlenker, S., Schlickeiser, R., Schwanke, U., Sol, H., Spangler, D., Spanier, F., Steenkamp, R., Stegmann, C., Superina, G., Tavernet, J.-P., Terrier, R., Théoret, C. G., Tluczykont, M., van Eldik, C., Vasileiadis, G., Venter, C., Vincent, P., Völk, H. J., Wagner, S. J., and Ward, M. 2006. Observations of the Crab Nebula with HESS. *A&A 457*, 899–915.

Aharonian, F., Akhperjanian, A. G., and et al. 1993. Status and Upgrade of the HEGRA Air Shower Experiment at La Palma. In *International Cosmic Ray Conference*. International Cosmic Ray Conference, vol. 4. 291–+.

Aharonian, F. A., Akhperjanian, A. G., Barrio, J. A., Bernlöhr, K., Börst, H., Bojahr, H., Bolz, O., Contreras, J. L., Cortina, J., Denninghoff, S., Fonseca, V., Gonzalez, J. C., Götting, N., Heinzelmann, G., Hermann, G., Heusler, A., Hofmann, W., Horns, D., Ibarra, A., Jung, I., Kankanyan, R., Kestel, M., Kettler, J., Kohnle, A., Konopelko, A., Kornmeyer, H., Kranich, D., Krawczynski, H., Lampeitl, H., Lorenz, E., Lucarelli, F., Magnussen, N., Mang, O., Meyer, H., Mirzoyan, R., Moralejo, A., Padilla, L., Panter, M., Plaga, R., Plyasheshnikov, A., Prahl, J., Pühlhofer, G., Rauterberg, G., Röhring, A., Rhode, W., Rowell, G. P., Sahakian, V., Samorski, M., Schilling, M., Schröder, F., Stamm, W., Tluczykont, M., Völk, H. J., Wiedner, C., and Wittek, W. 2001b. A Study of Tycho's SNR at TeV Energies with the HEGRA CT-System. *A&A 373*, 292–300.

Aharonian, F. A., Akhperjanian, A. G., Beilicke, M., Bernloehr, K., Bojahr, H., Bolz, O., Boerst, H., Coarasa, T., Contreras, J. L., Cortina, J., Denninghoff, S., Fonseca, V., Girma, M., Goetting, N., Heinzelmann, G., Hermann, G., Heusler, A., Hofmann, W., Horns, D., Jung, I., Kankanyan, R., Kestel, M., Kettler, J., Kohnle, A., Konopelko, A., Kornmeyer, H., Kranich, D., Krawczynski, H., Lampeitl, H., Lopez, M., Lorenz, E., Lucarelli, F., Mang, O., Meyer, H., Mirzoyan, R., Moralejo, A., Ona, E., Panter, M., Plyasheshnikov, A., Puehlhofer, G., Rauterberg, G., Reyes, R., Rhode, W., Ripken, J., Roehring, A., Rowell, G. P., Sahakian, V., Samorski, M., Schilling, M., Siems, M., Sobzynska, D., Stamm, W., Tluczykont, M., Voelk, H. J., Wiedner, C. A., and Wittek, W. 2002. A Search for TeV gamma-ray Emission from SNRs, Pulsars and Unidentified GeV Sources in the Galactic Plane in the Longitude Range between -2 deg and 85 deg. *A&A 395*, 803–811.

Aharonian, F. A., Drury, L. O., and Voelk, H. J. 1994. GeV/TeV gamma-ray emission from dense molecular clouds overtaken by supernova shells. *A&A 285*, 645–647.

Albert, J., Aliu, E., Anderhub, H., Antoranz, P., Armada, A., Baixeras, C., Barrio, J. A., Bartko, H., Bastieri, D., Becker, J. K., Bednarek, W., Berger, K., Bigongiari, C., Biland, A., Bock, R. K., Bordas, P., Bosch-Ramon, V., Bretz, T., Britvitch, I., Camara, M., Carmona, E., Chilingarian, A., Coarasa, J. A., Commichau, S., Contreras, J. L., Cortina, J., Costado, M. T., Curtef, V., Danielyan, V., Dazzi, F., de Angelis, A., Delgado, C., de Los Reyes, R., de Lotto, B., Domingo-Santamaría, E., Dorner, D., Doro, M., Errando, M., Fagiolini, M., Ferenc, D., Fernández, E., Firpo, R., Flix, J., Fonseca, M. V., Font, L.,

Fuchs, M., Galante, N., García-López, R., Garczarczyk, M., Gaug, M., Giller, M., Goebel, F., Hakobyan, D., Hayashida, M., Hengstebeck, T., Herrero, A., Höhne, D., Hose, J., Hsu, C. C., Jacon, P., Jogler, T., Kosyra, R., Kranich, D., Kritzer, R., Laille, A., Lindfors, E., Lombardi, S., Longo, F., López, J., López, M., Lorenz, E., Majumdar, P., Maneva, G., Mannheim, K., Mansutti, O., Mariotti, M., Martínez, M., Mazin, D., Merck, C., Meucci, M., Meyer, M., Miranda, J. M., Mirzoyan, R., Mizobuchi, S., Moralejo, A., Nilsson, K., Ninkovic, J., Oña-Wilhelmi, E., Otte, N., Oya, I., Paneque, D., Panniello, M., Paoletti, R., Paredes, J. M., Pasanen, M., Pascoli, D., Pauss, F., Pegna, R., Persic, M., Peruzzo, L., Piccioli, A., Poller, M., Puchades, N., Prandini, E., Raymers, A., Rhode, W., Ribó, M., Rico, J., Rissi, M., Robert, A., Rügamer, S., Saggion, A., Sánchez, A., Sartori, P., Scalzotto, V., Scapin, V., Schmitt, R., Schweizer, T., Shayduk, M., Shinozaki, K., Shore, S. N., Sidro, N., Sillanpää, A., Sobczynska, D., Stamerra, A., Stark, L. S., Takalo, L., Temnikov, P., Tescaro, D., Teshima, M., Tonello, N., Torres, D. F., Turini, N., Vankov, H., Vitale, V., Wagner, R. M., Wibig, T., Wittek, W., Zandanel, F., Zanin, R., and Zapatero, J. 2007a. Observation of VHE γ-rays from Cassiopeia A with the MAGIC telescope. *A&A 474*, 937–940.

Albert, J., Aliu, E., Anderhub, H., Antoranz, P., Armada, A., Baixeras, C., Barrio, J. A., Bartko, H., Bastieri, D., Becker, J. K., Bednarek, W., Berger, K., Bigongiari, C., Biland, A., Bock, R. K., Bordas, P., Bosch-Ramon, V., Bretz, T., Britvitch, I., Camara, M., Carmona, E., Chilingarian, A., Coarasa, J. A., Commichau, S., Contreras, J. L., Cortina, J., Costado, M. T., Curtef, V., Danielyan, V., Dazzi, F., De Angelis, A., Delgado, C., de los Reyes, R., De Lotto, B., Domingo-Santamaría, E., Dorner, D., Doro, M., Errando, M., Fagiolini, M., Ferenc, D., Fernández, E., Firpo, R., Flix, J., Fonseca, M. V., Font, L., Fuchs, M., Galante, N., García-López, R., Garczarczyk, M., Gaug, M., Giller, M., Goebel, F., Hakobyan, D., Hayashida, M., Hengstebeck, T., Herrero, A., Hirotani, K., Höhne, D., Hose, J., Hsu, C.-C., Jacon, P., Jogler, T., Kosyra, R., Kranich, D., Kritzer, R., Laille, A., Lindfors, E., Lombardi, S., Longo, F., López, J., López, M., Lorenz, E., Majumdar, P., Maneva, G., Mannheim, K., Mansutti, O., Mariotti, M., Martínez, M., Mazin, D., Merck, C., Meucci, M., Meyer, M., Miranda, J. M., Mirzoyan, R., Mizobuchi, S., Moralejo, A., Nieto, D., Nilsson, K., Ninković, J., Oña-Wilhelmi, E., Otte, N., Oya, I., Paneque, D., Panniello, M., Paoletti, R., Paredes, J. M., Pasanen, M., Pascoli, D., Pauss, F., Pegna, R., Persic, M., Peruzzo, L., Piccioli, A., Poller, M., Prandini, E., Puchades, N., Raymers, A., Rhode, W., Ribó, M., Rico, J., Rissi, M., Robert, A., Rügamer, S., Saggion, A., Sánchez, A., Sartori, P., Scalzotto, V., Scapin, V., Schmitt, R.,

Schweizer, T., Shayduk, M., Shinozaki, K., Shore, S. N., Sidro, N., Sillanpää, A., Sobczyńska, D., Stamerra, A., Stark, L. S., Takalo, L., Temnikov, P., Tescaro, D., Teshima, M., Tonello, N., Torres, D. F., Turini, N., Vankov, H., Vitale, V., Wagner, R. M., Wibig, T., Wittek, W., Zandanel, F., Zanin, R., and Zapatero, J. 2007b. Constraints on the Steady and Pulsed Very High Energy Gamma-Ray Emission from Observations of PSR B1951+32/CTB 80 with the MAGIC Telescope. *Astrophys. J. 669*, 1143–1149.

Amenomori, M., Cao, Z., Ding, L. K., Feng, Z. Y., Hibino, K., Hotta, N., Huang, Q., Huo, A. X., Jia, H. Y., and Jiang, G. Z. 1992. Search for steady emission of 10-TeV gamma rays from the Crab Nebula, Cygnus X-3, and Hercules X-1 using the Tibet Air Shower Array. *Physical Review Letters 69*, 2468–2471.

Angerhofer, P. E., Strom, R. G., Velusamy, T., and Kundu, M. R. 1981. A Multifrequency Study of CTB:80 with the Westerbork Synthesis Radio Telescope. *A&A 94*, 313.

Arons, J. and Tavani, M. 1994. Relativistic particle acceleration in plerions. *Astrophys. J. Suppl. 90*, 797–806.

Asaoka, I. and Koyama, K. 1990. Do all the Crab-like supernova remnants have an X-ray photon index near a value of 2? *PASJ 42*, 625–632.

Bartko, H., Bednarek, W., Delgado, C., and et al. 2008. Search for gamma-ray emission from the Supernova Remnants W66, W44 and IC443 with the MAGIC Telescope. In *International Cosmic Ray Conference*. International Cosmic Ray Conference, vol. 2. 655–658.

Bednarek, W. and Bartosik, M. 2003. Gamma-rays from the pulsar wind nebulae. *A&A 405*, 689–702.

Bell, A. R. 1978a. The acceleration of cosmic rays in shock fronts. I. *MNRAS 182*, 147–156.

Bell, A. R. 1978b. The acceleration of cosmic rays in shock fronts. II. *MNRAS 182*, 443–455.

Berezhko, E. G. and Völk, H. J. 2004. Direct evidence of efficient cosmic ray acceleration and magnetic field amplification in Cassiopeia A. *A&A 419*, L27–L30.

Bernlöhr, K., Carrol, O., Cornils, R., Elfahem, S., Espigat, P., Gillessen, S., Heinzelmann, G., Hermann, G., Hofmann, W., Horns, D., Jung, I., Kankanyan, R., Katona, A., Khelifi, B., Krawczynski, H., Panter, M., Punch, M., Rayner, S., Rowell, G., Tluczykont, M., and van Staa, R. 2003. The optical system of the H.E.S.S. imaging atmospheric Cherenkov telescopes. Part I: layout and components of the system. *Astroparticle Physics 20*, 111–128.

Bhattacharya, D., Chantell, M. C., Coppi, P., Covault, C. E., Dragovan, M., Gregorich, D. T., Hanna, D. S., Mukherjee, R., Ong, R. A., Oser, S., Ragan, K., Tümer, O. T., and Williams, D. A. 1997. Solar tower atmospheric Cherenkov effect experiment (STACEE) for ground based gamma ray astronomy. In *Proceedings of the Fourth Compton Symposium*, C. D. Dermer, M. S. Strickman, & J. D. Kurfess, Ed. American Institute of Physics Conference Series, vol. 410. 1626–1630.

Bi, X.-J., Chen, T.-L., Wang, Y., and Yuan, Q. 2009. The Diffuse GeV-TeV γ-Ray Emission of the Cygnus Region. *Astrophys. J. 695*, 883–887.

Bietenholz, M. F., Hester, J. J., Frail, D. A., and Bartel, N. 2004. The Crab Nebula's Wisps in Radio and Optical. *Astrophys. J. 615*, 794–804.

Blandford, R. D. and Ostriker, J. P. 1978. Particle acceleration by astrophysical shocks. *Astrophys. J. Lett. 221*, L29–L32.

Borione, A., Cronin, J. W., Covault, C. E., Fick, B. E., Gibbs, K. G., Krimm, H. A., McKay, T. A., Müller, D., Newport, B. J., Ong, R. A., Rosenberg, L. J., Catanese, M., Green, K. D., Matthews, J., Nitz, D. F., Sinclair, D., van der Velde, J. C., and Kieda, D. 1993. CASA-MIA: A "precision" EAS detector. In *Very High Energy Cosmic-Ray Interactions*, L. Jones, Ed. American Institute of Physics Conference Series, vol. 276. 207–211.

Borkowski, K. J., Rho, J., Reynolds, S. P., and Dyer, K. K. 2001. Thermal and Nonthermal X-Ray Emission in Supernova Remnant RCW 86. *Astrophys. J. 550*, 334–345.

Bradbury, S. 1999. The Very Energetic Radiation Imaging Telescope Array System (VERITAS). In *International Cosmic Ray Conference*. International Cosmic Ray Conference, vol. 5. 280–+.

Branch, D. and Miller, D. L. 1993. Type IA supernovae as standard candles. *Astrophys. J. Lett. 405*, L5–L8.

Buckley, J. H., Akerlof, C. W., Carter-Lewis, D. A., Catanese, M., Cawley, M. F., Connaughton, V., Fegan, D. J., Finley, J. P., Gaidos, J. A., Hillas, A. M., Krennrich, F., Lamb, R. C., Lessard, R. W., McEnery, J. E., Mohanty, G., Quinn, J., Rodgers, A. J., Rose, H. J., Rovero, A. C., Schubnell, M. S., Sembroski, G., Srinivasan, R., Weekes, T. C., and Zweerink, J. 1998. Constraints on cosmic-ray origin from TeV gamma-ray observations of supernova remnants. *A&A 329*, 639–658.

Casandjian, J.-M. and Grenier, I. A. 2008. A revised catalogue of EGRET γ-ray sources. *A&A 489*, 849–883.

Castelletti, G., Dubner, G., Brogan, C., and Kassim, N. E. 2007. The low-frequency radio emission and spectrum of the extended SNR W44: new VLA observations at 74 and 324 MHz. *A&A 471*, 537–549.

Celik, O. 2008. Observations of crab nebula and pulsar with veritas. Ph.D. thesis, University of California Los Angeles.

Chandrasekhar, S. 1931. The Maximum Mass of Ideal White Dwarfs. *Astrophys. J. 74*, 81.

Charles, P. A. and Seward, F. D. 1995. *Exploring the X-ray Universe.* Cambridge University Press.

Čherenkov, P. A. 1937. Visible light from clear liquids under teh action of gamma radiation. *C.R. (Doklady) Acad. Sci. URSS 2*, 451–4.

Chevalier, R. A. 1977. The interaction of supernovae with the interstellar medium. *ARA&A 15*, 175–196.

Cho, S.-H., Kim, K. T., and Fukui, Y. 1994. CO study of the giant molecular cloud towards supernova remnant. *Astron. J. 108*, 634–638.

Cocconi, G. 1960. An air shower telescope and the detection of 10^{12} eV photon sources. In *International Cosmic Ray Conference*. International Cosmic Ray Conference, vol. 2. 309–+.

Cogan, P. 2006. Nanosecond Sampling of Atmospheric Čerenkov Radiation Applied to TeV Gamma-Ray Observations of Blazars with VERITAS. Ph.D. thesis, University College Dublin.

Cogan, P. 2008. VEGAS, the VERITAS Gamma-ray Analysis Suite. In *International Cosmic Ray Conference*. International Cosmic Ray Conference, vol. 3. 1385–1388.

Cornils, R., Gillessen, S., Jung, I., Hofmann, W., Beilicke, M., Bernlöhr, K., Carrol, O., Elfahem, S., Heinzelmann, G., Hermann, G., Horns, D., Kankanyan, R., Katona, A., Krawczynski, H., Panter, M., Rayner, S., Rowell, G., Tluczykont, M., and van Staa, R. 2003. The optical system of the H.E.S.S. imaging atmospheric Cherenkov telescopes. Part II: mirror alignment and point spread function. *Astroparticle Physics 20*, 129–143.

Cortina, J., Armada, A., Biland, A., Blanch, O., Garczarczyk, M., Goebel, F., Majumdar, P., Mariotti, M., Moralejo, A., Paneque, D., Paoletti, R., and Turini, N. 2005. Technical Performance of the MAGIC Telescope. In *International Cosmic Ray Conference*. International Cosmic Ray Conference, vol. 5. 359–+.

Cronin, J. W., Gaisser, T. K., and Swordy, S. P. 1997. Cosmic rays at the energy frontier. *Scientific American 276*, 32–37.

da Silva, L. A. L. 1993. The classification of supernovae. *Ap&SS 202*, 215–236.

Davies, J. M. and Cotton, E. S. 1957. Design of the quartermaster solar furnace. *Solar Energy 1,* 2-3 (April-July), 16–22.

de Jager, O. C. and Harding, A. K. 1992. The expected high-energy to ultra-high-energy gamma-ray spectrum of the Crab Nebula. *Astrophys. J. 396*, 161–172.

de Jager, O. C. and Mastichiadis, A. 1997. A Relativistic Bremsstrahlung/Inverse Compton Origin for 2EG J1857+0118 Associated with Supernova Remnant W44. *Astrophys. J. 482*, 874–+.

Dickel, J. R., van Breugel, W. J. M., and Strom, R. G. 1991. Radio structure of the remnant of Tycho's supernova (SN 1572). *Astron. J. 101*, 2151–2159.

Dobashi, K., Bernard, J.-P., and Fukui, Y. 1996. Molecular Clouds in Cygnus. II. Statistical Studies of Star-forming Regions. *Astrophys. J. 466*, 282–+.

Drury, L. O., Aharonian, F. A., and Voelk, H. J. 1994. The gamma-ray visibility of supernova remnants. A test of cosmic ray origin. *A&A 287*, 959–971.

Ergin, T. and VERITAS Collaboration. 2008. VERITAS Observations of the Supernova Remnant Cas A. In *AAS/High Energy Astrophysics Division*. Vol. 10. 31.08.

Esposito, J. A., Hunter, S. D., Kanbach, G., and Sreekumar, P. 1996. EGRET Observations of Radio-bright Supernova Remnants. *Astrophys. J. 461*, 820.

Fermi, E. 1949. On the Origin of the Cosmic Radiation. *Physical Review 75*, 1169–1174.

Galbraith, W. and Jelley, J. V. 1953. Light Pulses from the Night Sky associated with Cosmic Rays. *Nature 171*, 349–350.

Giacani, E. B., Dubner, G. M., Kassim, N. E., Frail, D. A., Goss, W. M., Winkler, P. F., and Williams, B. F. 1997. New Radio and Optical Study of the Supernova Remnant W44. *Astron. J. 113*, 1379.

Ginzburg, V. and Syrovatski, S. 1964. *The Origin of Cosmic Rays*. Pergamon Press Ltd., Oxford, New York.

Gök, F., Sezer, A., Aslan, Z., and Aktekin, E. 2008. Optical observations of the galactic supernova remnants G59.5+0.1, G84.9+0.5 and G67.7+1.8. *Ap&SS 318*, 207–214.

Green, D. A. 2006. A Catalogue of Galactic Supernova Remnants.

Green, D. A., Reynolds, S. P., Borkowski, K. J., Hwang, U., Harrus, I., and Petre, R. 2008. The Radio Expansion and Brightening of the Very Young Supernova Remnant G1.9+0.3. *MNRAS 387*, L54–L58.

Hartman, R. C., Bertsch, D. L., Bloom, S. D., Chen, A. W., Deines-Jones, P., Esposito, J. A., Fichtel, C. E., Friedlander, D. P., Hunter, S. D., McDonald, L. M., Sreekumar, P., Thompson, D. J., Jones, B. B., Lin, Y. C., Michelson, P. F., Nolan, P. L., Tompkins, W. F., Kanbach, G., Mayer-Hasselwander, H. A., Mucke, A., Pohl, M., Reimer, O., Kniffen, D. A., Schneid, E. J., von Montigny, C., Mukherjee, R., and Dingus, B. L. 1999. Third EGRET catalog. *VizieR Online Data Catalog 212*, 30079.

Helene, O. 1983. Upper Limit of Peak Area. *Nuclear Instruments and Methods 212*, 319–322.

Hester, J. J. 2008. The Crab Nebula: An Astrophysical Chimera. *ARA&A 46*, 127–155.

Hillas, A. M. 1985. Cerenkov light images of EAS produced by primary gamma. In *International Cosmic Ray Conference*, F. C. Jones, Ed. International Cosmic Ray Conference, vol. 3. 445–448.

Hillas, M. A. 1995. The MOCCA Program: Monte-Carlo Cascades. In *International Cosmic Ray Conference*. International Cosmic Ray Conference, vol. 1. 270–+.

Holder, J., Acciari, V. A., Aliu, E., Arlen, T., Beilicke, M., Benbow, W., Bradbury, S. M., Buckley, J. H., Bugaev, V., Butt, Y., Byrum, K. L., Cannon, A., Celik, O., Cesarini, A., Ciupik, L., Chow, Y. C. K., Cogan, P., Colin, P., Cui, W., Daniel, M. K., Ergin, T., Falcone, A. D., Fegan, S. J., Finley, J. P., Finnegan, G., Fortin, P., Fortson, L. F., Furniss, A., Gillanders, G. H., Grube, J., Guenette, R., Gyuk, G., Hanna, D., Hays, E., Horan, D., Hui, C. M., Humensky, T. B., Imran, A., Kaaret, P., Karlsson, N., Kertzman, M., Kieda, D. B., Kildea, J., Konopelko, A., Krawczynski, H., Krennrich, F., Lang, M. J., Lebohec, S., Maier, G., McCann, A., McCutcheon, M., Moriarty, P., Mukherjee, R., Nagai, T., Niemiec, J., Ong, R. A., Pandel, D., Perkins, J. S., Pohl, M., Quinn, J., Ragan, K., Reyes, L. C., Reynolds, P. T., Rose, H. J., Schroedter, M., Sembroski, G. H., Smith, A. W., Steele, D., Swordy, S. P., Toner, J. A., Valcarcel, L., Vassiliev, V. V., Wagner, R., Wakely, S. P., Ward, J. E., Weekes, T. C., Weinstein, A., White, R. J., Williams, D. A., Wissel, S. A., Wood, M., and Zitzer, B. 2008. Status of the VERITAS Observatory. In *American Institute of Physics Conference Series*, F. A. Aharonian, W. Hofmann, & F. Rieger, Ed. American Institute of Physics Conference Series, vol. 1085. 657–660.

Holder, J., Atkins, R. W., Badran, H. M., Blaylock, G., Bradbury, S. M., Buckley, J. H., Byrum, K. L., Carter-Lewis, D. A., Celik, O., Chow, Y. C. K., Cogan, P., Cui, W., Daniel, M. K., de La Calle Perez, I., Dowdall, C., Dowkontt, P., Duke, C., Falcone, A. D., Fegan, S. J., Finley, J. P., Fortin, P., Fortson, L. F., Gibbs,

K., Gillanders, G., Glidewell, O. J., Grube, J., Gutierrez, K. J., Gyuk, G., Hall, J., Hanna, D., Hays, E., Horan, D., Hughes, S. B., Humensky, T. B., Imran, A., Jung, I., Kaaret, P., Kenny, G. E., Kieda, D., Kildea, J., Knapp, J., Krawczynski, H., Krennrich, F., Lang, M. J., Lebohec, S., Linton, E., Little, E. K., Maier, G., Manseri, H., Milovanovic, A., Moriarty, P., Mukherjee, R., Ogden, P. A., Ong, R. A., Petry, D., Perkins, J. S., Pizlo, F., Pohl, M., Quinn, J., Ragan, K., Reynolds, P. T., Roache, E. T., Rose, H. J., Schroedter, M., Sembroski, G. H., Sleege, G., Steele, D., Swordy, S. P., Syson, A., Toner, J. A., Valcarcel, L., Vassiliev, V. V., Wakely, S. P., Weekes, T. C., White, R. J., Williams, D. A., and Wagner, R. 2006. The first VERITAS telescope. *Astroparticle Physics 25*, 391–401.

Hui, C. Y. and Becker, W. 2008. Exploring the X-ray emission properties of the supernova remnant G67.7+1.8 and its central X-ray sources. *ArXiv e-prints*.

Hulsizer, R. I. and Rossi, B. 1948. Search for Electrons in the Primary Cosmic Radiation. *Physical Review 73,* 11 (June), 1402–1403.

Kamper, K. and van den Bergh, S. 1976. Optical studies of Cassiopeia A. V - A definitive study of proper motions. *Astrophys. J. Suppl. 32*, 351–366.

Kang, H. and Drury, L. O. 1992. A comparison of models for supernova remnants including cosmic rays. *Astrophys. J. 399*, 182–184.

Kawachi, A., Hayami, Y., Jimbo, J., Kamei, S., Kifune, T., Kubo, H., Kushida, J., LeBohec, S., Miyawaki, K., Mori, M., Nishijima, K., Patterson, J. R., Suzuki, R., Tanimori, T., Yanagita, S., Yoshikoshi, T., and Yuki, A. 2001. The optical reflector system for the CANGAROO-II imaging atmospheric Cherenkov telescope. *Astroparticle Physics 14*, 261–269.

Kieda, D. B., Allen, D., Hall, J., Nagai, T., Snure, M., Vassiliev, V. V., and Walker, G. 2003. Calibration Systems for the VERITAS Observatory. In *International Cosmic Ray Conference*. International Cosmic Ray Conference, vol. 5. 2831–+.

Koo, B.-C., Reach, W. T., Heiles, C., Fesen, R. A., and Shull, J. M. 1990. Detection of an expanding H I shell in the old supernova remnant CTB 80. *Astrophys. J. 364*, 178–186.

Kothes, R., Fedotov, K., Foster, T. J., and Uyaniker, B. 2006. A catalogue of Galactic supernova remnants from the Canadian Galactic plane survey. I. Flux densities, spectra, and polarization characteristics. *A&A 457*, 1081–1093.

Krause, O., Birkmann, S. M., Usuda, T., Hattori, T., Goto, M., Rieke, G. H., and Misselt, K. A. 2008a. The Cassiopeia A Supernova Was of Type IIb. *Science 320*, 1195–.

Krause, O., Tanaka, M., Usuda, T., Hattori, T., Goto, M., Birkmann, S., and Nomoto, K. 2008b. Tycho Brahe's 1572 supernova as a standard typeIa as revealed by its light-echo spectrum. *Nature 456*, 617–619.

Landecker, T. L., Higgs, L. A., and Wendker, H. J. 1993. G 76.9+1.0 - a Supernova Remnant and Unusual Properties. *A&A 276*, 522.

Li, T.-P. and Ma, Y.-Q. 1983. Analysis methods for results in gamma-ray astronomy. *Astrophys. J. 272*, 317–324.

Li, X. H., Lu, F. J., and Li, T. P. 2005. X-Ray Spectroscopy of PSR B1951+32 and Its Pulsar Wind Nebula. *Astrophys. J. 628*, 931–937.

Loiseau, N., Reich, W., Wielebinski, R., Reich, P., and Muench, W. 1988. A survey of an area around the north ecliptic pole at 11 CM wavelength. *A&AS 75*, 67–78.

Lorimer, D. R., Lyne, A. G., and Camilo, F. 1998. A search for pulsars in supernova remnants. *A&A 331*, 1002–1010.

Markiewicz, W. J., Drury, L. O., and Voelk, H. J. 1990. Diffusive particle acceleration in spherically symmetric shock waves - Supernova remnant origin of cosmic rays. *A&A 236*, 487–502.

Mavromatakis, F. 2003. Optical line emission from the supernova remnant G 73.9+0.9. *A&A 398*, 153–158.

Mavromatakis, F., Papamastorakis, J., Ventura, J., Becker, W., Paleologou, E. V., and Schaudel, D. 2001. The supernova remnants G 67.7+1.8, G 31.5-0.6 and G 49.2-0.7. *A&A 370*, 265–272.

McCann, A., Hanna, D., Kildea, J., and McCutcheon, M. 2009. A New Mirror Alignment System for the VERITAS Telescopes. *ArXiv e-prints*.

Merck, M., Bertsch, D. L., Dingus, B. L., Esposito, J. A., Fichtel, C. E., Fierro, J. M., Hartman, R. C., Hunter, S. D., Kanbach, G., Kniffen, D. A., Lin, Y. C., Mayer-Hasselwander, H. A., Michelson, P. F., von Montigny, C., Muecke, A., Mukherjee, R., Nolan, P. L., Pohl, M., Schneid, E., Sreekumar, P., Thompson, D. J., and Willis, T. D. 1996. Study of the spectral characteristics of unidentified galactic EGRET sources. Are they pulsar-like? *A&AS 120*, C465+.

Otte, A. N., Aliu, E., Contreras, J. L., and et al. 2008. Observation of the Crab Nebula with the MAGIC telescope. In *International Cosmic Ray Conference*. International Cosmic Ray Conference, vol. 2. 827–830.

Particle Data Group, Amsler, C., Doser, M., Antonelli, M., Asner, D. M., Babu, K. S., Baer, H., Band, H. R., Barnett, R. M., Bergren, E., Beringer, J., Bernardi, G., Bertl, W., Bichsel, H., Biebel, O., Bloch, P., Blucher, E., Blusk, S., Cahn, R. N., Carena, M., Caso, C., Ceccucci, A., Chakraborty, D., Chen,

M.-C., Chivukula, R. S., Cowan, G., Dahl, O., D'Ambrosio, G., Damour, T., de Gouvêa, A., Degrand, T., Dobrescu, B., Drees, M., Edwards, D. A., Eidelman, S., Elvira, V. D., Erler, J., Ezhela, V. V., Feng, J. L., Fetscher, W., Fields, B. D., Foster, B., Gaisser, T. K., Garren, L., Gerber, H.-J., Gerbier, G., Gherghetta, T., Giudice, G. F., Goodman, M., Grab, C., Gritsan, A. V., Grivaz, J.-F., Groom, D. E., Grünewald, M., Gurtu, A., Gutsche, T., Haber, H. E., Hagiwara, K., Hagmann, C., Hayes, K. G., Hernández-Rey, J. J., Hikasa, K., Hinchliffe, I., Höcker, A., Huston, J., Igo-Kemenes, P., Jackson, J. D., Johnson, K. F., Junk, T., Karlen, D., Kayser, B., Kirkby, D., Klein, S. R., Knowles, I. G., Kolda, C., Kowalewski, R. V., Kreitz, P., Krusche, B., Kuyanov, Y. V., Kwon, Y., Lahav, O., Langacker, P., Liddle, A., Ligeti, Z., Lin, C.-J., Liss, T. M., Littenberg, L., Liu, J. C., Lugovsky, K. S., Lugovsky, S. B., Mahlke, H., Mangano, M. L., Mannel, T., Manohar, A. V., Marciano, W. J., Martin, A. D., Masoni, A., Milstead, D., Miquel, R., Mönig, K., Murayama, H., Nakamura, K., Narain, M., Nason, P., Navas, S., Nevski, P., Nir, Y., Olive, K. A., Pape, L., Patrignani, C., Peacock, J. A., Piepke, A., Punzi, G., Quadt, A., Raby, S., Raffelt, G., Ratcliff, B. N., Renk, B., Richardson, P., Roesler, S., Rolli, S., Romaniouk, A., Rosenberg, L. J., Rosner, J. L., Sachrajda, C. T., Sakai, Y., Sarkar, S., Sauli, F., Schneider, O., Scott, D., Seligman, W. G., Shaevitz, M. H., Sjöstrand, T., Smith, J. G., Smoot, G. F., Spanier, S., Spieler, H., Stahl, A., Stanev, T., Stone, S. L., Sumiyoshi, T., Tanabashi, M., Terning, J., Titov, M., Tkachenko, N. P., Törnqvist, N. A., Tovey, D., Trilling, G. H., Trippe, T. G., Valencia, G., van Bibber, K., Vincter, M. G., Vogel, P., Ward, D. R., Watari, T., Webber, B. R., Weiglein, G., Wells, J. D., Whalley, M., Wheeler, A., Wohl, C. G., Wolfenstein, L., Womersley, J., Woody, C. L., Workman, R. L., Yamamoto, A., Yao, W.-M., Zenin, O. V., Zhang, J., Zhu, R.-Y., Zyla, P. A., Harper, G., Lugovsky, V. S., and Schaffner, P. 2008. Review of Particle Physics. *Physics Letters B 667*, 1–5.

Petruk, O. 2009. Approximation of the radiation power of electrons due to the inverse-Compton process in the black-body photon field. *A&A 499*, 643–648.

Reich, W., Fürst, E., Reich, P., and Junkes, N. 1988. New Supernova Remnants from Deep Radio Continuum Surveys. In *IAU Colloq. 101: Supernova Remnants and the Interstellar Medium*, R. S. Roger and T. L. Landecker, Eds. 293–+.

Roache, E., Irvin, R., Perkins, J. S., and et al. 2008. Mirror Facets for the VERITAS Telescopes. In *International Cosmic Ray Conference*. International Cosmic Ray Conference, vol. 3. 1397–1400.

Sasaki, M., Kothes, R., Plucinsky, P. P., Gaetz, T. J., and Brunt, C. M. 2006. Evidence for Shocked Molecular Gas in the Galactic Supernova Remnant CTB 109 (G109.1-1.0). *Astrophys. J. Lett. 642*, L149–L152.

Sasaki, M., Plucinsky, P. P., Gaetz, T. J., Smith, R. K., Edgar, R. J., and Slane, P. O. 2004. XMM-Newton Observations of the Galactic Supernova Remnant CTB 109 (G109.1-1.0). *Astrophys. J. 617*, 322–338.

Schein, M., Jesse, W. P., and Wollan, E. O. 1941. The Nature of the Primary Cosmic Radiation and the Origin of the Mesotron. *Physical Review 59,* 7 (April), 615.

Schlickeiser, R. 2002. *Cosmic Ray Astrophysics*.

Sinnis, G. 2005. HAWC: A Next Generation VHE All-Sky Telescope. In *High Energy Gamma-Ray Astronomy*, F. A. Aharonian, H. J. Völk, & D. Horns, Ed. American Institute of Physics Conference Series, vol. 745. 234–245.

Slane, P. 2002. Particle Acceleration in Supernova Remnants and Pulsar Wind Nebulae. *ArXiv Astrophysics e-prints*.

Smith, A. J. 2005. The MILAGRO Gamma Ray Observatory. In *International Cosmic Ray Conference*. International Cosmic Ray Conference, vol. 10. 227–+.

Smith, D. A., Bergeret, H., Cordier, A., Dumora, D., Eschstruth, P., Espigat, P., Fabre, B., Fleury, P., Giebels, B., Merkel, B., Meynadier, C., Paré, E., Procureur, J., Québert, J., Rob, L., Roy, P., Salamon, M. H., Schovanek, P., and Vrana, J. 1997. CELESTE: A Large Heliostat Array for Gamma Ray Astronomy. *Nuclear Physics B Proceedings Supplements 54*, 362–366.

Tatematsu, K., Fukui, Y., Nakano, M., Kogure, T., Ogawa, H., and Kawabata, K. 1987. Molecular clouds in the vicinity of the semicircular supernova remnant G109.1-1.0. *A&A 184*, 279–283.

The, L.-S., Leising, M. D., Kurfess, J. D., Johnson, W. N., Hartmann, D. H., Gehrels, N., Grove, J. E., and Purcell, W. R. 1996. CGRO/OSSE observations of the Cassiopeia A SNR. *A&AS 120*, C357.

Thorstensen, J. R., Fesen, R. A., and van den Bergh, S. 2001. The Expansion Center and Dynamical Age of the Galactic Supernova Remnant Cassiopeia A. *Astron. J. 122*, 297–307.

Toner, J. A., Acciari, V. A., Cesarini, A., and et al. 2008. Bias Alignment of the VERITAS Telescopes. In *International Cosmic Ray Conference*. International Cosmic Ray Conference, vol. 3. 1401–1404.

Turver, K. E. and Weekes, T. C. 1978. Gamma-ray astronomy from 10 to 100 GeV. *Nuovo Cimento B Serie 45*, 99–108.

Vink, J. 2004. Supernova Remnants: An Introductory Review. In *Young Neutron Stars and Their Environments*, F. Camilo and B. M. Gaensler, Eds. IAU Symposium, vol. 218. 57.

Vink, J. and Laming, J. M. 2003. On the Magnetic Fields and Particle Acceleration in Cassiopeia A. *Astrophys. J. 584*, 758–769.

Warren, J. S., Hughes, J. P., Badenes, C., Ghavamian, P., McKee, C. F., Moffett, D., Plucinsky, P. P., Rakowski, C., Reynoso, E., and Slane, P. 2005. Cosmic-Ray Acceleration at the Forward Shock in Tycho's Supernova Remnant: Evidence from Chandra X-Ray Observations. *Astrophys. J. 634*, 376–389.

Weekes, T. 2003. *Very High Energy Gamma-Ray Astronomy*, 1^{st} ed. Series in Astronomy and Astrophysics. Institute of Physics Publishing Ltd., Philadelphia.

Weekes, T. C., Cawley, M. F., Fegan, D. J., Gibbs, K. G., Hillas, A. M., Kowk, P. W., Lamb, R. C., Lewis, D. A., Macomb, D., Porter, N. A., Reynolds, P. T., and Vacanti, G. 1989. Observation of TeV gamma rays from the Crab nebula using the atmospheric Cerenkov imaging technique. *Astrophys. J. 342*, 379–395.

Weisskopf, M. C., Hester, J. J., Tennant, A. F., Elsner, R. F., Schulz, N. S., Marshall, H. L., Karovska, M., Nichols, J. S., Swartz, D. A., Kolodziejczak, J. J., and O'Dell, S. L. 2000. Discovery of Spatial and Spectral Structure in the X-Ray Emission from the Crab Nebula. *Astrophys. J. Lett. 536*, L81–L84.

Yoshita, K., Miyata, E., and Tsunemi, H. 2000. Discovery of a New Supernova Remnant in the Direction of G69.7+1.0. *PASJ 52*, 867–873.

Yukawa, Y. 2008. Search for TeV Gamma-ray Emission from the Supernova Remnant W44 with the CANGAROO-III telescope. Ph.D. thesis, The University of Tokyo.

Zweerink, J. 1999. THE SOLAR TWO GAMMA-RAY OBSERVATORY: Astronomy between 20-300 GeV. In *International Cosmic Ray Conference*. International Cosmic Ray Conference, vol. 5. 223–+.